UNIVERSITY OF OKLAHOMA

GRADUATE COLLEGE

FABRICATION AND CHARACTERIZATION OF POROUS CNF/PDMS NANOCOMPOSITE FOR SENSING APPLICATION

A THESIS

SUBMITTED TO THE GRADUATE FACULTY

in partial fulfillment of the requirements for the

Degree of

MASTER OF SCIENCE

By

WENYUAN LUO
Norman, Oklahoma
2018

Downloaded from SHAREOK. Persistent Handle URL: https://hdl.handle.net/11244/301321

FABRICATION AND CHARACTERIZATION OF POROUS CNF/PDMS NANOCOMPOSITE FOR SENSING APPLICATION

A THESIS APPROVED FOR THE
SCHOOL OF AEROSPACE AND MECHANICAL ENGINEERING

BY

_____
Dr. Mrinal C. Saha, Chair

_____
Dr. Yingtao Liu, Co-Chair

_____
Dr. Chung-Hao Lee

© Copyright by WENYUAN LUO 2018
All Rights Reserved.

It is my pleasure to dedicate this thesis to my parents, who always encourage me go on every adventure and help me grow as a person. Also, I want to dedicate it to my girlfriend, the person I truly fell in love with, who gave all infinity love.

Acknowledgements

My deep gratitude goes first to my advisor Dr. Mrinal. C. Saha, who adroitly invested enormous time in my research and graduate student life. His genuine enthusiasm guided me as a professional researcher from the first day when I worked with him. Without his selfless helps and guides, I have no possible to accomplish this research work. I would also extend my appreciations to my co-advisor Dr. Yingtao Liu, his tremendous knowledge inspired me become an assiduous person. His creative ideas always lead me in a correct path. In addition, I would also thanks to my committee member, Dr. Chung-Hao Lee, his tireless spirit instructed me be a promising researcher. In addition, I am truly appreciated all the staffs from Aerospace & Mechanical department at the University of Oklahoma (Norman), and my lab mates such as Mark Olima, Chowdhury Shoieb, Jingyu Wang, Mohammad Abshirini, and Mohammad Charara. They have provided endless supports and kept me in motivated. There is no possible for me to have precious opportunities to tour ocean of knowledge without help from everyone.

Above all, I am fully indebted to my respectable parents for their unrequited love from the first day of school in USA. Special thanks to my beloved girlfriend, you are the person who made me believe that I was worth it and made me smile every single day.

Table of Contents

Acknowledgements iv

List of Tables viii

List of Figures x

Abstract xvi

Chapter 1. Introduction 1

1.1 Backgrounds of Conductive Porous PDMS based Nanocomposites 2

1.2 Literature Reviews of Porous PDMS based Sensors 3

1.3 Discussions of the Fabrication Strategies of Porous PDMS Foam 6

1.3.1 Straightforward Templating Technique 6

1.3.2 Gas Foaming Technique 7

1.3.3 Emulsion Polymerization Technique 8

1.3.4 Phase Separation Technique 9

1.3.5 Freeze-Drying Backfilling Technique 9

1.3.6 3D Print Technique 10

1.4 Scope of the Research 11

1.5 Research Objectives 12

Chapter 2. Materials and Fabrication Methodology 13

2.1 Materials 14

2.1.1 Carbon Nanofiber (CNF) and Tetrahydrofuran (THF) 14

2.1.2 Polydimethylsiloxane (PDMS) 15

2.1.3 Pure and Demerara Cane Sugar 16

2.2 Fabrication Procedures 18

2.2.1 Pure Solid PDMS Cube 18
2.2.2 Pristine PDMS Foam with Different Porosities 19
2.2.3 Porous CNF/PDMS Nanocomposites Created by the Direct Method 21
2.2.4 Porous CNF/PDMS Nanocomposites Crated by the Indirect Method 22
Chapter 3. Characterizations of Morphology and CNF Adhesive Capacity 25
3.1 Pristine Porous PDMS Foams 25
3.2 Porous CNF/PDMS Nanocomposites 27
3.2.1 SEM of Porous CNF/PDMS Nanocomposites Created by the Direct Method 27
3.2.2 SEM of Porous CNF/PDMS Nanocomposites Created by the Indirect Method 33
3.3 Interfacial Adhesion Study 41
Chapter 4. Material and Mechanical Properties: Porosity, Young's Modulus, and Electrical Properties 43
4.1 Density and Porosity of Pristine Porous PDMS Foams 44
4.2 Quasi-static Compressive Test 48
4.3 Mechanical Property (Young's Modulus) of Pristine Porous PDMS Foams 50
4.3.1 The Young's Modulus of Pristine Solid PDMS and Porous PMDS Foams 50
4.3.2 Robustness of Mechanical Performance 52
4.3.3 Prediction of the Young's Modulus 54
4.4 Mechanical behavior of Porous CNF/PDMS Nanocomposites 56
4.4.1 Porous Nanocomposites Created by the Direct Method 56

4.4.2 Porous Nanocomposites Created by the Indirect Method 59
4.5 Electrical Properties of Porous CNF/PDMS Nanocomposites Created by the Direct and Indirect Methods 63
Chapter 5. Sensing Concept Validation 68
5.1 Sensing Functions of Porous CNF/PDMS Nanocomposites Created by the Direct Method 70
5.2 Sensing Functions of Porous CNF/PDMS Nanocomposites Created by the Indirect Method 77
5.3 Robustness and Durability of Sensing Responses 82
5.3.1 Robustness Validation 83
5.3.2 Durability Validation 84
Chapter 6. Summary and Scope for Future Works 88
References 91

List of Tables

Table 1. Summary of the pros and cons of the common techniques to fabricate porous PDMS foam 11

Table 2. Volume ratio of different sugar templates 19

Table 3. CNF loading in the porous CNF/PDMS nanocomposites created by the indirect method 24

Table 4. The CNF distribution of nanocomposites created by the direct method 40

Table 5. The CNF distribution of nanocomposites created by the indirect method 41

Table 6. Density of solid PDMS cubes measured by pycnometer 44

Table 7. Density and Porosity of 4S pristine porous foams 45

Table 8. Density and Porosity of 1B3S pristine porous foams 46

Table 9. Density and Porosity of 1S3B pristine porous foams 46

Table 10. Density and Porosity of 4B pristine porous foams 47

Table 11. Average density and porosity of pristine porous foams 47

Table 12. The Young's modulus of solid PDMS cubes 51

Table 13. Young's modulus and density of pristine porous PDMS foams 52

Table 14. Young's modulus under different strain rates of 4S pristine PDMS foam 54

Table 15. Experimental Vs. Predicted Young's Modulus 56

Table 16. Young's modulus of porous nanocomposites created by the direct method with various amount of CNF loading 58

Table 17. Young's modulus under different strain rates of porous nanocomposites created by the direct method (1 wt.% CNF) 59

Table 18. Young's modulus of porous nanocomposites created by the indirect method with various amount of CNF loading 61
Table 19. Young's modulus under different strain rates of porous nanocomposites created by the indirect method (0.92 wt.% CNF)..... 62
Table 20. Electrical resistivity and conductivity of porous nanocomposites created by the direct method with various CNF loading 66
Table 21. Electrical resistivity and conductivity of porous nanocomposites created by the indirect method with various CNF loading 66
Table 22. Gauge factors of porous nanocomposites created by the direct method (3 wt.% CNF) under different maximum compressive strain..... 74
Table 23. Gauge factors of porous nanocomposites created by the direct method (6 wt.% CNF) under different maximum compressive strain..... 75
Table 24. Gauge factors of porous nanocomposites created by the direct method (9 wt.% CNF) under different maximum compressive strain..... 75
Table 25. Gauge factors of porous nanocomposites created by the indirect method (0.47 wt.% CNF) under different maximum compressive strain..... 78
Table 26. Gauge factors of porous nanocomposites created by the indirect method (0.78 wt.% CNF) under different maximum compressive strain..... 79
Table 27. Gauge factors of porous nanocomposites created by the indirect method (0.92 wt.% CNF) under different maximum compressive strain..... 80
Table 28. Selections of optimized porous nanocomposites created by the direct and indirect methods 83

List of Figures

Figure 1. Schematic procedures of porous CNF/PDMS nanocomposites created by the direct and indirect methods 14

Figure 2. The molecular structure of PDMS 15

Figure 3. Dow Corning® Sylgard 184 Silicone Elastomer Kit [41] 16

Figure 4. Florida Crystals® pure and demerara cane sugars 16

Figure 5. Pure and demerara cane sugar crystals at low (left) and high (right) magnifications 17

Figure 6. The length and width distribution of filtered pure (a & b) and demerara (c & d) cane sugars 18

Figure 7. Stainless steel mold for solid PDMS cube 19

Figure 8. Solid PDMS cube 19

Figure 9. Silicon rubber (female) and 3D printed PLA (male)molds 20

Figure 10. Sugar cubes with different volume ratios between pure and demerara cane sugars (top) and pristine PDMS foams with various porosities (bottom) 20

Figure 11. The process of CNF coated pure cane sugar (a) 100 ml CNF/THF suspension (b) Pure cane sugar (c) 20 ml CNF/THF suspension (d) Sugar/CNF/THF mixture (e) CNF coated sugar 22

Figure 12. Porous nanocomposites created by the direct method fabrication process (From left to right: CNF coated sugar cube, PDMS infiltration, Porous CNF/PDMS nanocomposites) 22

Figure 13. Swelling of PDMS foam in THF/CNF suspension (a) before sonication (b) immediately after sonication (c) THF completely evaporate 23

Figure 14. Porous nanocomposites created by the indirect method fabrication process (From left to right: Sugar cube, PDMS illustration, Sugar crystals dissolved, Porous CNF/PDMS nanocomposites) 23
Figure 15. Pristine porous PDMS foams with various porosities (a) 4S; (b) 3S1B; (c) 1S3B; (d) 4B 26
Figure 16. CNF coated sugar cube in different magnifications 28
Figure 17. Nanocomposites created by the direct method (1 wt.% CNF) in different magnifications 31
Figure 18. Nanocomposites created by the direct method (9 wt.% CNF) in different magnifications 33
Figure 19. Nanocomposites created by the indirect method (0.24 wt.% CNF) in different magnifications (a-d: top; e-h: middle) 37
Figure 20. Nanocomposites created by the indirect method (0.78 wt.% CNF) in different magnifications (a-d: top; e-j: middle) 40
Figure 21. Double-sided tape experiment (a) Before; (b) After 42
Figure 22. Morphology of solid PDMS cube 44
Figure 23. Relationship between density of pristine porous PDMS foam and small sugar volume percentage 48
Figure 24. Relationship between porosity of pristine porous PDMS foam and small sugar volume percentage 48
Figure 25. Stress-strain curve of solid PDMS cube 49
Figure 26. Stress-strain curve of pristine porous PDMS foam 50
Figure 27. Stress-strain curve of solid PDMS cube within linear elasticity region 51

Figure 28. Stress-strain curve of pristine porous PDMS foam within linear elasticity region 52
Figure 29. Stress-strain curve of 4S pristine porous PDMS foam with various strain rates 53
Figure 30. Stress-strain curve of 4S pristine porous PDMS foam within linear elasticity region with various strain rates 54
Figure 31. Prediction of the Young's modulus 56
Figure 32. Stress-strain curve of porous nanocomposites created by the direct method with various amount of CNF loading 57
Figure 33: Stress-strain curve of porous nanocomposites created by the direct method with various amount of CNF loading within linear elasticity region 57
Figure 34. Stress-strain curve of porous nanocomposites created by the direct method (1 wt.% CNF) with various strain rates 58
Figure 35. Stress-strain curve of porous nanocomposites created by the direct method (1 wt.% CNF) with various strain rates within linear elasticity region 59
Figure 36. Stress-strain curve of porous nanocomposites created by the indirect method with various amount of CNF loading 60
Figure 37. Stress-strain curve of porous nanocomposites created by the indirect method with various amount of CNF loading within linear elasticity region 60
Figure 38. Stress-strain curve of porous nanocomposites created by the indirect method (0.92 wt.% CNF) with various strain rates 61
Figure 39. Stress-strain curve of porous nanocomposites created by the indirect method (0.92 wt.% CNF) with various strain rates within linear elasticity region 62

Figure 40. Electrical resistance measurement set up of porous nanocomposites created by the direct method 63
Figure 41. Electrical resistance measurement set up of porous nanocomposites created by the indirect method 64
Figure 42. Electrical resistance of porous nanocomposites created by the direct method with various amount of CNF loading 64
Figure 43. Electrical resistance of porous nanocomposites created by the indirect method with various amount of CNF loading 65
Figure 44. Electrical resistivity of porous nanocomposites created by the direct and indirect methods 67
Figure 45. Electrical conductivity of porous nanocomposites created by the direct and indirect methods 67
Figure 46. Schematic setup for sensing functions validation in compressive loading and unloading test..... 70
Figure 47. Effect of compressive deformation on the electrical networks of the porous CNF/PDMS nanocomposites..... 71
Figure 48. Sensing functions of porous nanocomposites created by the direct method (3 wt.% CNF) under different maximum compressive strain..... 74
Figure 49. Sensing functions of porous nanocomposites created by the direct method (6 wt.% CNF) under different maximum compressive strain..... 74
Figure 50. Sensing functions of porous nanocomposites created by the direct method (9 wt.% CNF) under different maximum compressive strain..... 75

Figure 51. Validation of relative resistance change and stress as a function of strain porous nanocomposites (3 wt.% CNF) created by the direct method 76
Figure 52. Validation of relative resistance change and stress as a function of strain porous nanocomposites (6 wt.% CNF) created by the direct method 76
Figure 53. Validation of relative resistance change and stress as a function of strain porous nanocomposites (9 wt.% CNF) created by the direct method 77
Figure 54. Sensing functions of porous nanocomposites created by the indirect method (0.47 wt.% CNF) under different maximum compressive strain 78
Figure 55. Sensing functions of porous nanocomposites created by the indirect method (0.78 wt.% CNF) under different maximum compressive strain 79
Figure 56. Sensing functions of porous nanocomposites created by the indirect method (0.92 wt.% CNF) under different maximum compressive strain 79
Figure 57. Validation of relative resistance change and stress as a function of strain porous nanocomposites (0.47 wt.% CNF) created by the indirect method 81
Figure 58. Validation of relative resistance change and stress as a function of strain of porous nanocomposites (0.78 wt.% CNF) created by the indirect method 81
Figure 59. Validation of relative resistance change and stress as a function of strain of porous nanocomposites (0.92 wt.% CNF) created by the indirect method 82
Figure 60. Robustness validation of porous nanocomposites (9 wt.% CNF) created by the direct method 84
Figure 61. Robustness validation of porous nanocomposites (0.78 wt.% CNF) created by the indirect method 84

Figure 62. Relative resistance change throughout durability test of porous nanocomposites (9 wt.% CNF) created by the direct method 85
Figure 63. Durability validation of porous nanocomposites (9 wt.% CNF) created by the direct method 85
Figure 64. Relative resistance change throughout durability test of porous nanocomposites (0.78 wt.% CNF) created by the indirect method 86
Figure 65. Durability validation of porous nanocomposites (0.78 wt.% CNF) created by the indirect method 86
Figure 66. Hysteresis of porous nanocomposites (0.78 wt.% CNF) created by the indirect method 87

Abstract

Electrically conductive polydimethylsiloxane (PDMS) elastomer-based materials are growing as one of the critical needs for the emerging field of wearable electronics due to its high elastic limits and good biocompatibility. Recently, researches have shown that the porous structure can further improve its deformability and decrease the concentration of conducive nanofiller loading to easily reach percolation threshold at the same time. To address the challenge of fabricating 3D interconnected conductive PDMS based nanocomposites, this thesis focuses on characterizing material and mechanical properties, and sensing functions of nanocomposites for sensing application. In this study, highly flexible and electrically conductive porous carbon nanofiber (CNF)/PDMS nanocomposites are fabricated by sugar templating strategy and CNF is incorporated by direct and indirect techniques.

The pristine porous PDMS foams with various porosities are synthesized by sugar templating method with different volume ratios of fine and coarse sugar. The mechanical performances, and relationship between Young's modulus and porosity are firstly investigated under quasi-static compressive tests to select the feasible substrate for sensor design. The Young's modulus of pristine porous PDMS foam can be properly predicted by a polynomial equation with known density. Then, a series of CNF loadings are deposited in the porous PDMS cube by direct and indirect techniques. Scanning electron microscopy (SEM) is used to examine the morphologies of samples, and the distributions and dispersion quality of CNF. The electrical conductivity of nanocomposites created by the direct and indirect methods are measured. The porous CNF/PDMS nanocomposites created by the indirect method exhibits a lower

percolation threshold. The porous CNF/PDMS nanocomposites created by the direct method endow a stronger interfacial adhesion between the CNF and the PDMS polymer. The experimental results under quasi-static compressive test show the concentration of CNF loading can impact the mechanical property (Young's modulus) of porous CNF/PDMS nanocomposites.

The piezoresistive sensing functions of nanocomposites created by both methods are characterized by correlating the relative electrical resistance change and the compressive strain under cyclic compressive loading and unloading tests at the strain range from 1.25% to 40%. The mechanisms of piezoresistive sensor are responsible for the variation of electric resistance. The tunable sensing performance and gauge factor are depending on the concentration of CNF loading and the fabrication technique. The optimum formulas of porous CNF/PDMS nanocomposites created by both methods are ascertained based on the sensing performances. Finally, the durability and robustness of identified samples are demonstrated.

Chapter 1. Introduction

Highly flexible and electrically conductive materials have become of great interest in recent years, attracting a growing number of researchers. These researchers have combined efforts in order to adapt these materials for a variety of promising applications such as health monitor [1], wearable electronics [2], flexible pressure sensors [3], and robotic manipulation [4]. In particular, PDMS, as a hyper-elastic material, has drawn tremendous attentions in conducing material fabrication because its Si-O backbone endows it with properties such as chemically inertness, non-toxicity, biocompatibility, environment friendliness, high flexibility, excellent thermal and electric resistance, hydrophobic surface, and low surface energy [5]. Additionally, varying curing conditions [6] or silica content [7] can affect its mechanical properties. It is important to note that solid PDMS (non-porous) requires larger energy input than porous PDMS foam to achieve the same deformation. It is also important to note that the tensile fracture strain of solid PDMS is three times lower than its porous counterparts [8]. Therefore, porous PDMS structure possesses remarkable energy saving potential while achieving severe physical conditions. To take advantage of both the outstanding properties of PDMS and of 3D porous structures, porous conductive PDMS foam has been developed and extended to a large number of applications such as flexible conductors [8], highly sensitive sensors [9], fluidic electronics [10], energy storage devices [11], and electric nanogenerators [12]. The fundamental theories of these applications are converting different types of external stimuli into electricity response via the piezoresistive [8], piezoelectric[11], capacitive[13], triboelectric[14], and electromagnetic [12] effects.

The objectives of this chapter include: (1) Discuss the basic backgrounds and advantages of conductive porous PDMS based nanocomposites. (2) Illustrate how the available testing strategies to validate samples can develop promising sensing applications. (3) Expound various techniques to fabricate porous PDMS foam with conclusion of their advantages and disadvantages. (4) Illustrate the scope of the research and research objectives.

1.1 Backgrounds of Conductive Porous PDMS based Nanocomposites

Development of conductive porous PDMS nanocomposites require that conducting nanofillers are introduced into a porous matrix. Various conductive nanofillers, such as, metal nanoparticle [15], carbon nanotube (CNT) [10], carbon nanofiber (CNF) [8, 16], and graphene [17], have been applied in efforts to create these nanocomposites. Of these, carbon derived-nanofillers are much lighter. Moreover, carbon nanofibers disperse easily than CNT in a polymer matrix or solvent due to CNT having greater Van der Waals force to hold molecules together, which typically needs the aid of chemical dispersants or functionalization techniques [18]. Nonuniform dispersion in a polymer matrix exhibits degradation of tensile strength and impact strength [19]. Sandler et al. [20] reported the tensile stiffness and strength of CNF/poly (ether ether ketone) solid nanocomposites increased with a higher nanofiber loading, however, the tensile fracture strain of nanocomposites with 15 wt.% nanofiller was approximately three times lower than 5 wt.% nanofiller. This is due to a high concentration of nanofillers loading in sample, results in a nonuniform dispersion. Shoieb et al. [21] reported that solid PDMS based sensor by THF solvent assisted ultra-sonication method required 12 wt. % nanofiller loading to achieve excellent sensing

functions. Ease of dispersion is vital because nonuniform dispersion leads to a relative high concentration of carbon nanofiller required to attain sufficient electrical conductivity for satisfying potential applications. Inclusion of the proper amount of nanofiller to achieve satisfactory electrical conductivity is referred to as the percolation threshold. To avoid any dispersion issues that may affect the mechanical and electrical properties of the carbon derived nanocomposites, recent researches have shown that depositing CNF into a 3D interconnected porous structure serves as a potential solution [8, 10]. Wu et al. [8] characterized the sensing performances of porous CNF/PDMS strips with less than 1 wt.% of CNF (compare with 5 wt.% solid CNF/PDMS by Shoieb et al. [21]) under cyclic tensile test. This structure exhibited failure strain as 120% and sensing response with gauge factor as high as 6.5. As a comparison, conventional metallic foil strain gauge exhibits a significantly lower failure strain and gauge factor.

1.2 Literature Reviews of Porous PDMS based Sensors

Porous structure sensors are becoming popular in practical uses due to the benefits of highly flexible and stretchable substrate, hypersensitivity, and convenient fabrication procedures. Prior to develop nanocomposites as sensing applications, several preliminary validations are necessary to execute for proving their sensing. This section introduces several available testing strategies to validate sensing functions of porous PDMS based sensors and their mechanisms.

Wu et al. [8] evaluated the sensing capability of porous CNF/PDMS sensor under quasi-static tensile, and cyclic stretching and releasing tests. The resistance of nanocomposites increased continuously with applying stretch. Electrons moved though polymer if distance between neighbor CNF was less than the tunneling distance (5-

50nm). The sensor appeared a large deformation during stretching and CNF probably slid past or moved over each other in result of leading to enlarged gaps. Therefore, resistance increased in the direction of stretching due to an increasement in the tunneling resistance. Future more stretches, CNF may totally loss contact and caused a future conductivity decrement. Moreover, the sample was subjected to quasi-static tensile test, the relative resistance change initially displayed a nearly linear dependence on the strain up to 30%, while, exhibited a non-linear behavior at larger strain range. Besides, to validate durability of sensor, sample was subjected to cyclic loading up to 30% strain and unloading to original point in 10000 cycles. The resistance of nanocomposites displayed most fully recovered on each consecutive cycle after first few cycles, which indicated the outstanding durability of sensor. The possible reason that the resistance was not able to exactly recover is CNF appeared buckling phenomenal. Due to the Poisson's effect in the transverse stretching direction, CNF buckled out of the stretching plane. But after initial few cycles, the influence of buckling and fracture became weaker in result of displaying recovered piezoresistive sensing response.

Han et al. [10] characterized cubic porous CNT/PDMS nanocomposites on cyclic compressive loading and unloading test. The sample was sandwiched between two conducting metal plates. The results displayed around 10% relative resistance change for 20% compressive strain and 90% relative resistance change for 70% compressive strain. The resistance decreased due to CNT contacted neighbor so that created more electric networks under compressive load. King et al. [22] also explained mechanism in a similar way, the embedded carbon nanofiller tend to contact each other

under deformation. Carbon nanofiller initially sparely attached to the pore walls and there were little percolating carbon-carbon contacts on unloading stage. When compressive force was loaded, the sensor became more conductivity due to the numbers of carbon-carbon connections increased.

Rinaldi et al. [23] fabricated porous graphene/PDMS nanocomposites via the dipping infiltration method. The sample was subjected cyclic compressive loading and unloading test with strain rate varied over orders of magnitude. The results indicated that the sample did not have an excellent robust because the gauge factor was dependence of strain rate. The sensing function exhibited some unexpected phenomenal such as the electrical resistance suddenly fluctuated. Because different piezoresistive mechanisms happened at different strain range. Typically, porous foam experiences three regions under compressive test such as, linear elastic, plateau, and densification regions. The carbon filler created different types conducting paths in different regions. Without applied any loading on sample, carbon fillers adhered on the surface of the pores and created the conducting paths. When load was initially applied, within linear elastic region, adjacent carbon filler tend to contact each other in result of increase conductivity, which is a similar view from Wu et al. [8]. When a future load was applied, within the plateau region, the degradation of sensing function occurred due to nanofillers slid mutually. As the result, the length of pathways could either decrease or increase depend on different situations. For example, reduced overlap and broke path in raised areas may recede electrical conductivity, however, increased overlap in depressed area may enhance electrical conductivity. At the larger strain range, within the densification region, the pores started to collapse so that numerous nanofiller contacted

and overlapped, which is possible to generate multi-branches pathways, and thus enhanced electrical conductivity strongly.

1.3 Discussions of the Fabrication Strategies of Porous PDMS Foam

A wide range of approaches have been employed to fabricate porous PDMS foams, including: straightforward templating, gas foaming, emulsion polymerization, phase separation, freeze-drying backfilling, and 3D print techniques. This section introduce how various techniques fabricate foam and their pros and cons.

1.3.1 Straightforward Templating Technique

A straightforward templating technique is to utilize solid template as a porogen, which is possible to be dissolved or removed by the solving solutions assistances, and eventually leave over an interconnected PDMS skeleton as inverse of the template. Recently, many researchers reported several materials such as sugars, salts, polymer particles, and nickel foam were used to prepare sacrificial templates. Han et al. [10] reported cane sugar cubes were dry-pressed molding and infiltrated by PDMS prepolymer (the weight ratio of silicone elastomer and curing agent is normally 10:1). Followed by placing sugar cubes in vacuum regime to degas and facilitate PDMS prepolymer infiltration and cured at room temperature. Then, thin layer of cured PDMS on the surface of sugar cube was wiped off until surface completely exposed. Finally, porous PDMS foam was obtained after sugar template dissolved in water sonication bath. Zhang et al. [24] reported that porous PDMS foam was synthesized by a modified sugar-template method, which is a facile way to avoid the process of vacuum regime. PDMS prepolymer was firstly diluted with p-xylene before sugar particles introduced. The p-xylene decreased the viscosity of PDMS prepolymer in result of no air bubble

exhibiting. Zhao et al. [25] fabricated porous PDMS foam with smaller size pores by using salt microparticles. The mixture of PDMS prepolymer, salts, and dimethicone were packed tightly by high speed centrifuged in a polypropylene tube. After curing, salt template was submerged in ethanol to remove dimethicone. Most salts were dissolved in warm water easily, and residual salts were continually dissolved in dichloromethane and ethanol by hand squeeze. The matrix structure was controllable by the weight ratio PDMS prepolymer to dimethicone or the size of salt particles. Kang et al. [26] spin-coated PDMS prepolymer on a polystyrene latex microsphere cubic structure with an AZ1512 photoresist layer. After curing, sample was submerged in acetone to remove AZ1512 photoresist layer and cured PDMS thin film was automatically fell off from the substrate due to PDMS swelling issue. Porous PDMS foam was finally obtained after transferred into dimethylformamide to etch polystyrene heads completely. The pores size depended on size of polystyrene latex microspheres. This method ensured a narrow pore size distribution than using sugars or salts. In addition, nickel foam is another sacrificial template used to fabricate well sized porous PDMS foam with narrow pore size distribution. Chen et al. [27] reported that nickel foam was firstly dipped into dilute PDMS/ethyl acetate prepolymer solution and then nickel foam framework was cured by vacuum heating. Finally, porous PDMS foam was obtained after nickel foam completely removed by a ferric nitrate solution at 60°C for 72 hours and dried in high temperature to remove ferric nitrate.

1.3.2 Gas Foaming Technique

Gas foaming technique is a common method to fabricate porous PDMS foam with open or closed pores, but this method is hard to control the size of pore. Typically,

the gas bubbles are forming pore in porous PDMS. Kobayashi et al. [28] fabricated porous PDMS foam by hydrosilylation curing silicon compound, which contains vinyl group and hydrosilane in the presence of additives (water or ethanol). Eventually, the pores were obtained by gas foaming due to chemical reaction between the hydrosilane (SiH) group and OH group that provided by additives.

1.3.3 Emulsion Polymerization Technique

Polymerization of the emulsion phase plays an important role to fabricate porous PDMS foam for emulsion polymerization technique. Droplets of emulsion are utilized as the templates of the pores. Dozen years ago, Grosse et al. [29] synthesized porous PDMS foam by adding polysiloxane monoliths (siloxane-HIPEs). Siloxane-HIPEs was a continuous phase of an inverse emulsion, which was produced by hydrosilylation reaction with polymethylhydrosiloxane and vinylsiloxane monomers. Afterwards, the Karstedt catalyst (Pt metal and vimyl function) was introduced in and cured at 50°C for 72 hours. Finally, porous PDMS foam were fabricated after washing by water/ethanol mixture and acetone follow with drying in one week. Recently, Huang et al. [30] reported porous PDMS foam was facilely fabricated by mixing distilled water into PDMS prepolymer. Distilled water was firstly mechanical stirred at high speed mix (11,000 rpm) for 5 min and ensured water bubbles distributed uniformly in PDMS prepolymer. The pores were generated due to phase transition of water droplet, liquid sublimated to gas, during PDMS curing process in heating. In this method, the porosity was controllable by the weight ratio of PDMS to distilled water.

1.3.4 Phase Separation Technique

Solvent phase separation technique is a promising method to fabricate porous PDMS by inducing phase separation into PDMS. Phase separation is utilized as the template of pores. Lee et al. [31] synthesized porous PDMS foam by inducing the phase separation of polymethylmethacrylate (PMMA) in PDMS. The PDMS (only silicone elastomer), PMMA, and their block polymer (PDMS-b-PMMA) were firstly dissolved in toluene at 75°C and mixed uniformly. Successively, toluene was evaporated slowly in heating with stirring to induce phase separations. Afterwards, the curing agent were introduced and PDMS cured at 140°C for 12 hours. The sample was submerging in acetic acid solution to remove PMMA. Finally, porous PDMS foam was obtained after washing by deionized water, blowing with nitrogen gas, and drying in air. The pore size could be adjusted by drying temperatures and weight ratio of three polymers. The size of pore was smaller when the solution contained a smaller amount of PMMA, higher concentration of block copolymer, or dried at lower temperature.

1.3.5 Freeze-Drying Backfilling Technique

Freeze-drying backfilling technique fabricate porous PDMS foam with an orientational porous structure. Zhai et al. [32] reported that porous PDMS foam was fabricated through PDMS backfilled superhydrophobic poly (vinyl alcohol) (PVA) aerogel. PVA aerogel was firstly unidirectionally suspended and then freeze-dried in a lyophilized at -78°C for four days. It produced an unidirectionally aligned microtubular porous structure as template of pores. To facilitate PDMS infiltration, PVA was converted from hydrophilic to hydrophobic using a thermal chemical vapor deposition (CVD) technique. Then, the PVA aerogel was backfilled with the PDMS prepolymer

using a vacuum-assisted liquid filling method and placed in the centrifuged tube under ice bath to prevent the PDMS prepolymer from cross-linking during the filling stage. The backfilling process took up to four days to fill in the aerogel template. Finally, porous PDMS/aerogel foam was fabricated by curing at 125 °C for 30 minutes.

1.3.6 3D Print Technique

Innovation in industrial manufacturing have drawn tremendous attentions in recent years. 3D print is a novel and facile technique to fabricate porous PDMS foam instead of traditional methods. However, it remains a big challenge to direct print complicated or up-scaled porous structure due to the low viscosity of PDMS prepolymer. Hinton et al. [33] demonstrated 3D printed PDMS within a hydrophilic Carbopol gel by freeform reversible embedding. Because of the immiscibility between PDMS and Carbopol, extruded PDMS prepolymer could maintain a stable shape up to 72 hours in the Carbopol. Finally, Carbopol was removed by using phosphate buffered saline solution and eventually left over PDMS. In this way, porous PDMS foam is possible to fabricate if PDMS model designs with cavities. Duan et al. [34] 3D printed sacrificial scaffolds and embedded into PDMS prepolymer. Polylactic acid (PLA) scaffold was first 3D printed by a 0.2 mm syringe needle. PLA is eco-friendly and can be easily removed by certain solvents. Afterwards, PLA frame was submerged into PDMS prepolymer under vacuum regime and cured at 50°C for 5 hours. The curing temperature was lower than the glass transition temperature of PLA (60-65°C) to avoid frame change shape. The cured PDMS was then washed by dichloromethane to remove PLA. Finally, porous PDMS foam was obtained after drying process. The 3D print technique can skillfully customize the structure of porous PDMS foam.

Table 1. Summary of the pros and cons of the common techniques to fabricate porous PDMS foam

Fabrication techniques	Tunable pore size	Narrow pore size distribution	Well-order/shaped pores	Non-toxic solvents	No sophisticated instrument	Cost-effective
Straightforward templating (sugar/salt)	YES	NO	YES	YES	YES	YES
Straightforward templating (polystyrene)	YES	YES	YES	NO	NO	NO
Straightforward templating (nickel foam)	YES	YES	YES	NO	YES	NO
Gas foaming	NO	NO	NO	NO	YES	YES
Emulsion polymerization	YES	NO	NO	NO	YES	NO
Phase separation	YES	YES	YES	NO	NO	YES
Freeze-drying backfilling	YES	YES	YES	YES	NO	NO
3D print	YES	YES	YES	YES	NO	NO

1.4 Scope of the Research

In summary, the porous structure possesses low weight, low conductive nanofiller loading to reach percolation threshold, high flexibility and compressibility than non-porous counterpart. Also, a porous structure can potentially eliminate the risk of nonuniform nanofiller distribution. Comparing to other electrical conductivity nanofillers, CNF is lighter, low cost, and easy to disperse in a polymer matrix or solvent. Moreover, as shown in Table 1, straightforward templating (sugar) is a low cost, non-toxic solvent, no sophisticated instrument, and cost-effective method to fabricate porous PDMS foam because sugar, as the porogen, could be purchased from grocery store and easily dissolved by water. There are several studies in literatures to measure the mechanical properties of PDMS foam and investigate the sensing function of porous PDMS based sensor, however, there were only limited works focused on how porosity or nanofiller loading affects the Young's modulus of porous PDMS foam. Besides, limited work have dealt with how nanofiller loading effect sensing

performance of porous PDMS based sensor and the piezoresistive mechanism under the compressive test. Therefore, this thesis proposes to investigate the prediction of the Young's modulus of pristine porous PDMS foam through porosity or density. And characterize sensing performance of conductive porous CNF/PDMS nanocomposites with different CNF loading under cyclic compressive loading and unloading test.

1.5 Research Objectives

The research objectives of this study are including:

1) Fabricate pristine porous PDMS foam with different porosities by changing the volume ratio of different size sugar crystals.
2) Measure the Young's modulus of pristine porous PDMS foam under quasi-static compressive test and find out the relationship between the Young's modulus and porosity.
3) Fabricate the conductive porous CNF/PDMS nanocomposites with different CNF loading for sensing application. In addition, characterize their sensing performances under cyclic compressive test and explore the piezoresistive mechanism.
4) Select the optimum formula of sensor and validate its sensing robustness and durability.

Chapter 2. Materials and Fabrication Methodology

Porous conductive PDMS nanocomposites raw material selection and manufacturing procedure are the most significant factors needed to be considered. These factors become particularly important when feasibility, productivity, reliability, and cost efficiency are brought into sensor design. For electrical conductive porous sensor, dispersion quality of nanofiller, and toxicity and environment effect of raw materials are necessary to be addressed at the top of priority list. By considering comprehensively of the above factors, straightforward sugar templating technique was utilized to fabricate the porous PDMS foam. To become an electrically conductive material, CNF is introduced into porous PDMS foam via the direct and indirect methods as depicted in Figure 1. For direct method, the sugar crystals are first coated with CNF and then fill with PDMS prepolymer. For indirect method, porous PDMS foam is first fabricated, followed by forced impregnation of CNF via ultrasonic agitation. This chapter lists all the materials and procedures to fabricate solid PDMS, pristine porous PDMS foam, and porous CNF/PDMS nanocomposites created by the direct and indirect methods.

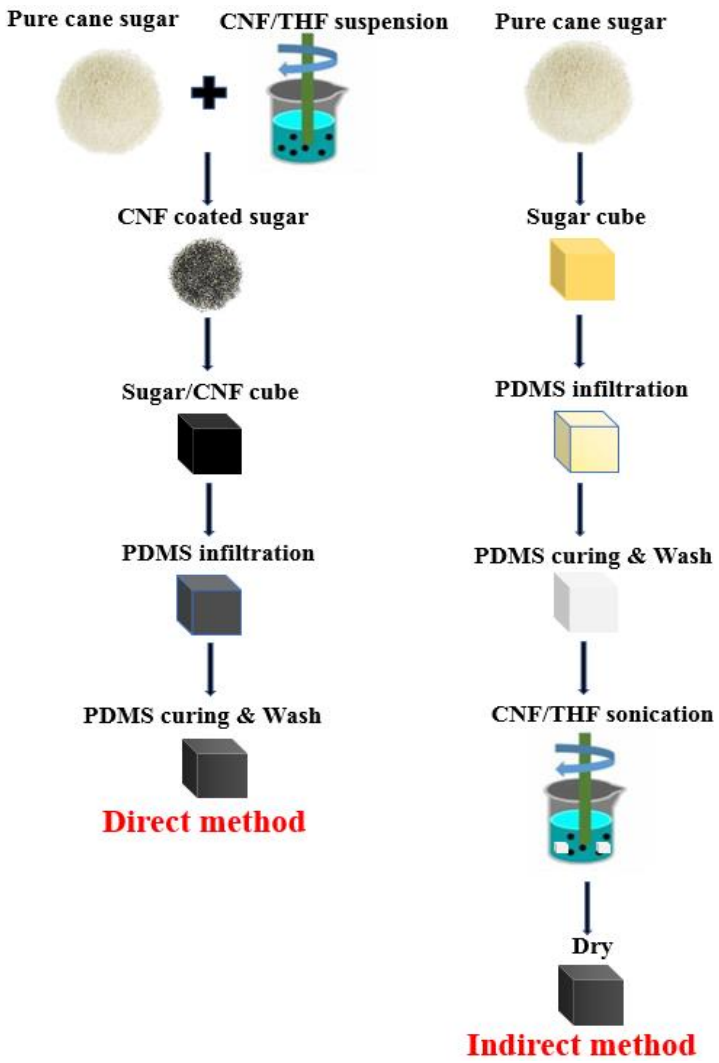


Figure 1. Schematic procedures of porous CNF/PDMS nanocomposites created by the direct and indirect methods

2.1 Materials

2.1.1 Carbon Nanofiber (CNF) and Tetrahydrofuran (THF)

The Pyograf-III PR-24XT-LHT CNF (Applied Science, Inc.), with an average diameter of about 100nm, are carbonized by chemical vapor deposited method. This specific type of CNF was selected as the electrically conductive nanofiller because of its relative low dispersion surface energy (145-165 mJ/m^2) and ability to provide the highest electrical conductivity in nanocomposites as reported in the manufacture's data sheet [35]. Tetrahydrofuran (THF), a low toxic organic solvent, was used to disperse

CNF due to its low surface tension, 26.4 dyn/cm at 25℃. In addition, it causes foam swelling up so that raise efficiency of CNF deposition for the indirect method [36].

2.1.2 Polydimethylsiloxane (PDMS)

The silicone polymer is comprised by silicone backbones (Si-O) with attaching monovalent organic radicals (RSi-O). The silicone backbone plays an important role to build a connection between inorganic and organic polymers. There are a number of substituents that can be attached to silicone backbone. PDMS is the most common type of silicone polymer with monovalent organic radicals as CH_3. This combination endows its outstanding physical and chemical properties such as, chemically inertness, low glass-transaction temperature (-120ºC), biocompatibility, environment friendless, high flexibility, excellent thermal, and low surface tension energy (21-22mN/m) [37]. The empirical formula of PDMS is $(C_2H_6OSi)_n$, and the fragmented formula is $(CH_3)_3SiO[Si(CH_3)_2O]_nSi(CH_3)_3$. The number of monomers repetitions, n, affects the state of non-cross-linked PDMS. Normally, lower n presents a liquid phase, while, higher n presents a semi-solid phase [38, 39]. The molecular structures of PDMS is depicted in Figure 2 [40].

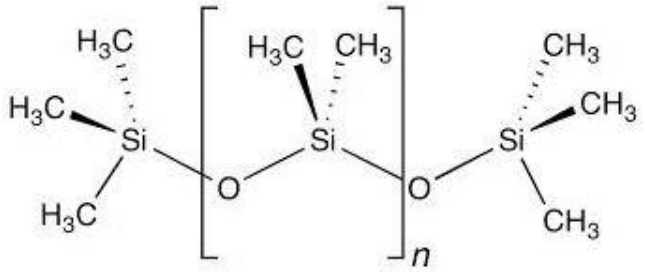


Figure 2. The molecular structure of PDMS

The off-the-shelf PDMS Sylgard 184 (Dow Corning Co. Ltd.) consists of silicon elastomer base and curing agent, as shown in Figure 3, which was used as the base material of porous pristine PDMS and porous CNF/PDMS nanocomposites.



Figure 3. Dow Corning® Sylgard 184 Silicone Elastomer Kit [41]

2.1.3 Pure and Demerara Cane Sugar

Pure and demerara cane sugar (Florida Crystals, Inc.), as shown in Figure 4, were utilized as the sugar crystals porogen due to its relative narrow size distribution compared with other brands available in grocery stores.



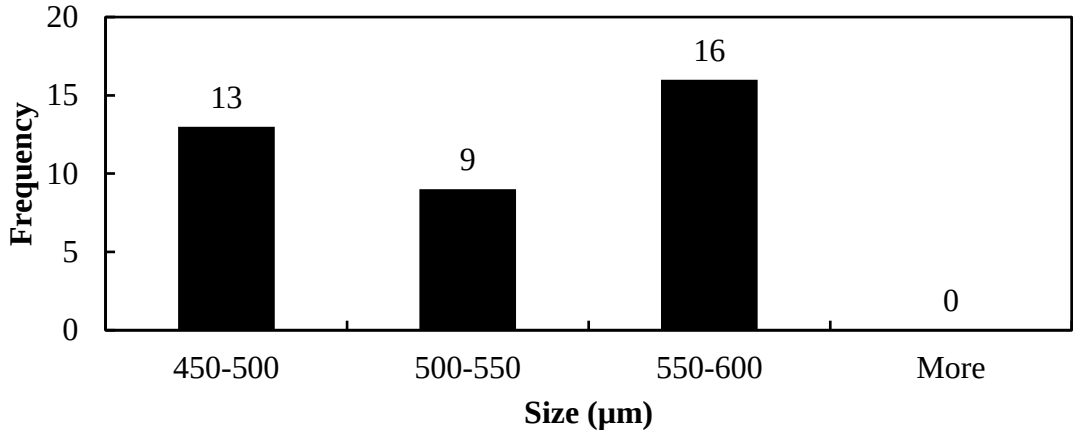
Figure 4. Florida Crystals® pure and demerara cane sugars

Pure and demerara cane sugar crystals were filtered using strainers to eliminate agglomerate and tiny crystals, with the purpose of narrowing size distribution. The average size of the filtered pure and demerara sugars was 500 µm and 2000 µm, with the range of (length x width) 450 µm - 600 µm x 400 µm - 550 µm and 2000 µm - 2600 µm x 1700 µm - 2200 µm, as shown in Figure 5 and Figure 6, respectively.

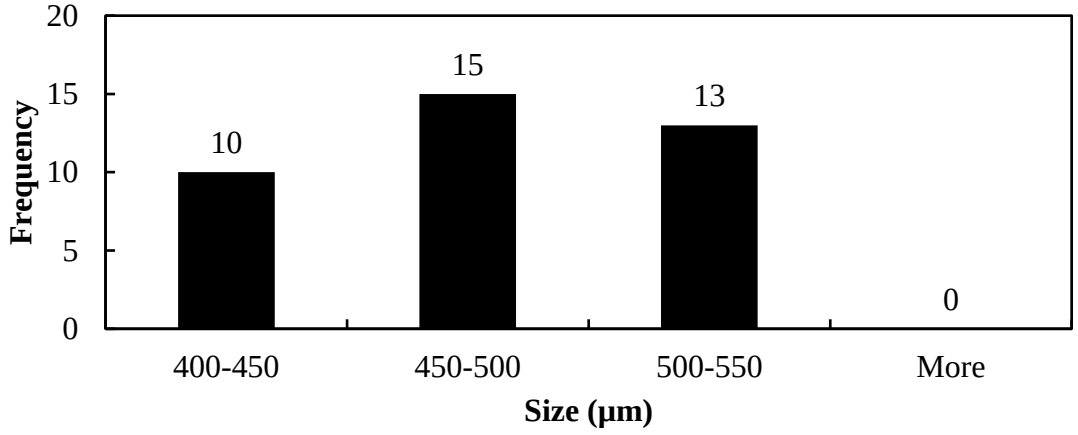


Figure 5. Pure and demerara cane sugar crystals at low (left) and high (right) magnifications

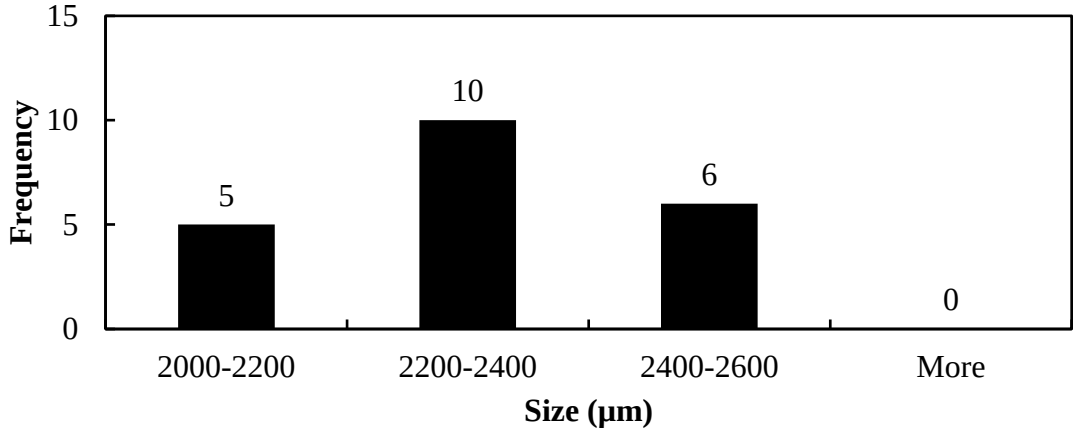
(a). Length distribution of pure cane sugar



(b). Width distribution of pure cane sugar



(c). Length distribution of demerara cane sugar



(d). Width distribution of demerara cane sugar

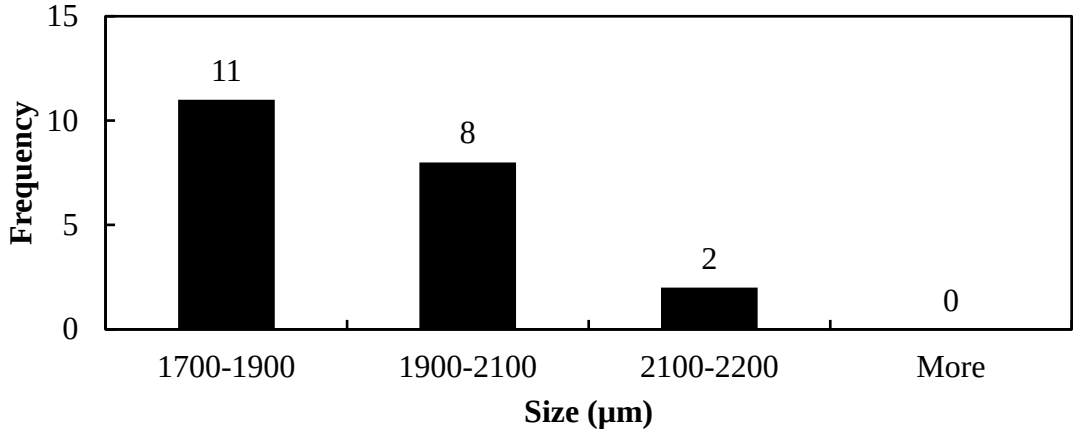


Figure 6. The length and width distribution of filtered pure (a & b) and demerara (c & d) cane sugars

2.2 Fabrication Procedures

2.2.1 Pure Solid PDMS Cube

The PDMS prepolymer was prepared by mixing the base and curing agent at a 10:1 weight ratio (as recommended by the manufacturer). The mixture was hand stirred for 5 minutes until enormous air bubbles appeared and then degassed for 15 minutes at a low vacuum regime (-0.1 MPa) in a desiccator to remove air bubbles. Then, the mixture poured into a stainless-steel 10mm*10mm*10mm cube shaped mold, as shown

in Figure 7. Afterwards, mold was degassed for another 30 minutes. Lastly, solid PDMS cube, as shown in Figure 8, was fabricated after being heated in an oven at 130℃ for 30 minutes.

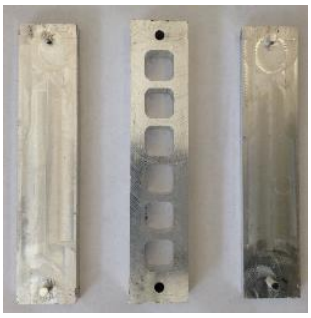


Figure 7. Stainless steel mold for solid PDMS cube



Figure 8. Solid PDMS cube

2.2.2 Pristine PDMS Foam with Different Porosities

Table 2. Volume ratio of different sugar templates

	Pure cane sugar (S)	**Demerara cane sugar (B)**
4S	100%	0%
3S1B	75%	25%
1S3B	25%	75%
4B	0%	100%

Pure cane sugar is small sugar, hence, denoted as S and demerara cane sugar is big sugar, hence, denoted as B. The S and B were mixed in four different volume ratios,4:0(4S), 3:1(3S1B), 1:3(1S3B), and 0:4(4B), as shown in Table 2. The sugar mixture was first blended with spraying water several times and packed tightly into a 10mm*10mm*10mm cube shape silicon rubber female mold (casted from 3D printed male mold), as shown in Figure 9, compressed at a 30kN permanent force for 5 minutes.

Afterwards, the mold was transferred to an oven at 130 ℃ for 1 hour and cooled down to room temperature. Sugar cubes were extracted readily after hardening. Subsequently, sugar cubes were submerged in the liquid PDMS prepolymer, and placed in a desiccator at a low vacuum regime under 15℃ to facilitate PDMS infiltrate into the pores of sugar cubes. After 12 hours infiltration, excess PDMS stuck on the surfaces of sugar cubes was removed. The cubes were transferred to oven cured at 130℃ in 30 minutes. After curing, excess cured PDMS along the edges was trimmed away using a razor. The cubes were submerged into 50℃ ultrasonic water bath in 3 hours followed with drying at 130℃ in 1 hour. Finally, sacrificial sugar crystals removed completely, resulting in porous pristine PDMS foams with various porosities, as shown in Figure 10.

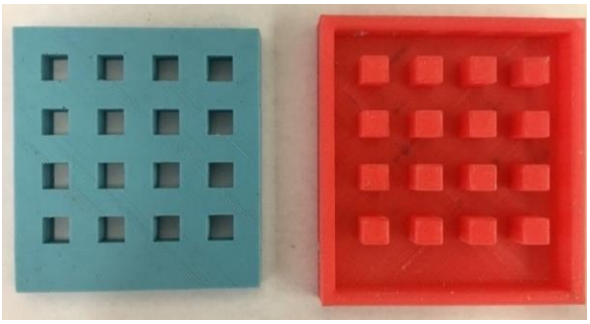


Figure 9. Silicon rubber (female) and 3D printed PLA (male)molds



Figure 10. Sugar cubes with different volume ratios between pure and demerara cane sugars (top) and pristine PDMS foams with various porosities (bottom)

2.2.3 Porous CNF/PDMS Nanocomposites Created by the Direct Method

Pre-calculated amount of CNF was introduced into 100 ml THF solvent and dispersed using a high intensity 750W ultrasonic probe at 35% amplitude in pulse mode (55 seconds on and 5 seconds off) for 6 hours in an iced bath to neutralize heat generated by probe, creating CNF/PDMS nanocomposites with 1 wt.%, 3 wt.%, 6 wt.%, and 9 wt.% CNF loading. At the end of the sonication period, there were no visible aggregates, even after suspensions were left standing overnight, as shown in Figure 11(a). To promote the process of solvent removal and avoid aggregation, the suspension was continuously stirred at 200 rpm under a fume hood to partially remove the solvent, until the suspension evaporated to around 25 ml, Figure 11(c). Pre-calculated filtered pure cane sugar crystals (11.5 g is suited for 8 cubes) poured into CNF/THF suspension, Figure 11 (d), and hand mixed once per 20 minutes. The remaining solvent was evaporated under a fume hood. Once all THF was completely removed, sugar particles appeared to be dyed black by CNF, Figure 11(e). Finally, porous CNF/PDMS nanocomposites were fabricated using a similar process as the pristine PDMS foam, replacing the sugar crystals with CNF coated sugar crystals. But, CNF coated sugar templates took longer time to completely dissolve. It is due to sugar crystals were wrapped by CNF, which reduced the contact surface area with water. Figure 12 illustrates the process in a flow chart from a CNF coated sugar cube to porous CNF/PDMS nanocomposites created by the direct method. It should be noted that a negligible amount of CNF was removed from the nanocomposites during the sugar dissolving process.

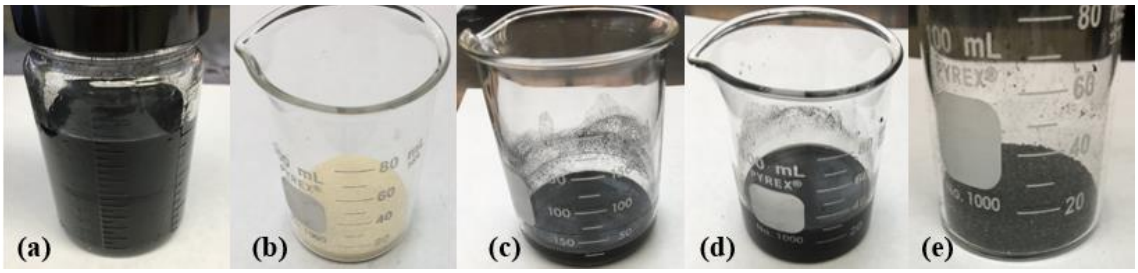


Figure 11. The process of CNF coated pure cane sugar (a) 100 ml CNF/THF suspension (b) Pure cane sugar (c) 20 ml CNF/THF suspension (d) Sugar/CNF/THF mixture (e) CNF coated sugar

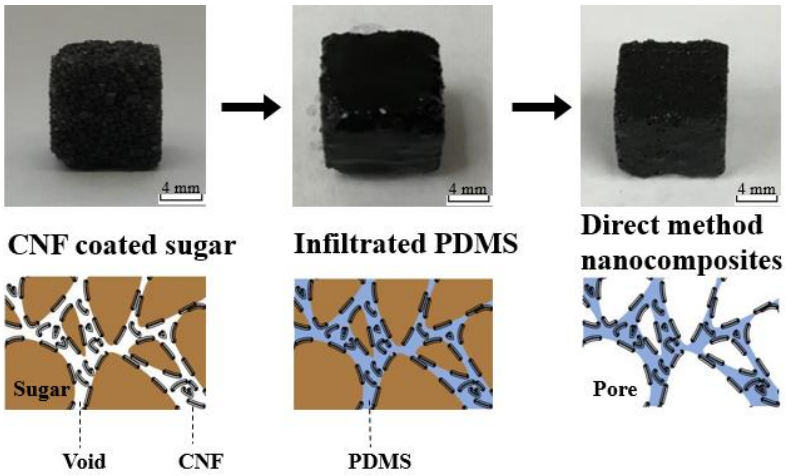


Figure 12. Porous nanocomposites created by the direct method fabrication process (From left to right: CNF coated sugar cube, PDMS infiltration, Porous CNF/PDMS nanocomposites)

2.2.4 Porous CNF/PDMS Nanocomposites Crated by the Indirect Method

Pre-calculated amount of CNF (0.21 g, 0.17g, 0.07g, and 0.035g) was introduced into container with 70 ml THF solvent and dispersed using the same technique as previous mentioned to prepare CNF/THF suspensions at different concentrations (3 g/L, 2.5 g/L, 1 g/L, and 0.5 g/L). 4S porous pristine PDMS foams were then introduced into well-dispersed CNF/THF suspensions and sonicated using a 750 W probe sonicator at 35% amplitude in pulse mode (55 seconds on and 5 seconds off) for 30 minutes. Because THF is an organic solvent with high PDMS compatibility, the swelling ratio is 1.38 [36], the porous PDMS foam quickly swelled up. The length of each side of the porous CNF/PDMS nanocomposites cube expanded from 10 mm to

13mm, as depicted in Figure 13. This swelling likely increased the efficiency of CNF penetration during sonication because pore surface area increased. Finally, porous CNF/PDMS nanocomposites were obtained after THF completely evaporated. The dimensions of the porous cube shrunk to their original size. Figure 14 shows the process from a sugar cube to porous CNF/PDMS nanocomposites created by the indirect method.

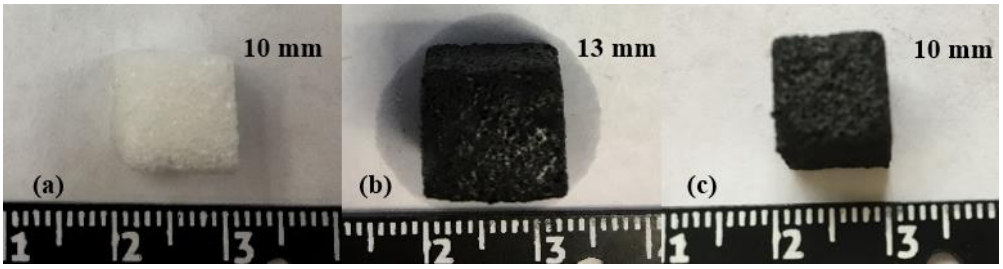


Figure 13. Swelling of PDMS foam in THF/CNF suspension (a) before sonication (b) immediately after sonication (c) THF completely evaporate

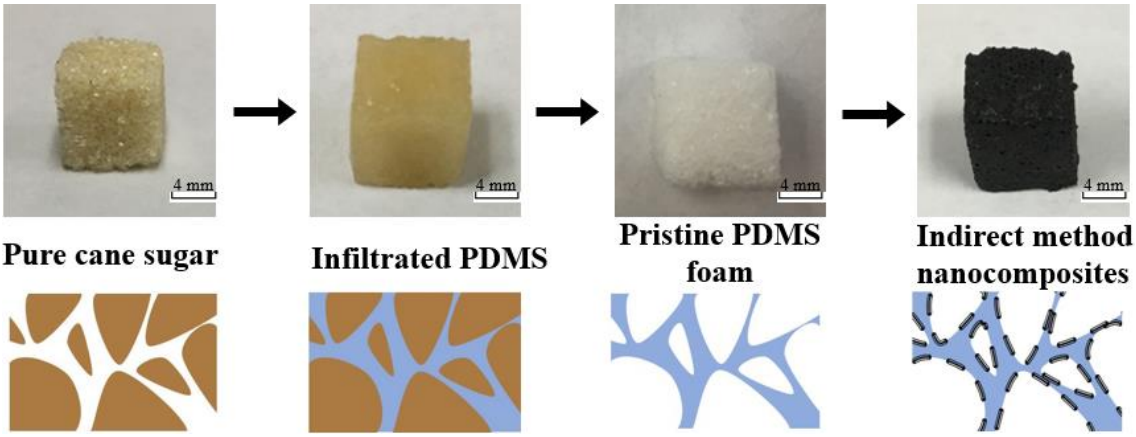


Figure 14. Porous nanocomposites created by the indirect method fabrication process (From left to right: Sugar cube, PDMS illustration, Sugar crystals dissolved, Porous CNF/PDMS nanocomposites)

Manufactured samples underwent several characterization tests to ensure their use in potential sensing applications. First, it is important to establish a CNF weight concentration for each sample. This is easy to characterize porous CNF/PDMS nanocomposites created by the direct method because the CNF loading coincides with the CNF concentration of the sugar cubes. However, it is not visualized for porous

CNF/PDMS nanocomposites created by the indirect method because CNF was penetrated through CNF/THF suspension under ultrasonic. Thus, the studies of the CNF loading for porous CNF/PDMS nanocomposites created by the indirect method was indeed to investigate.

Table 3 lists the weight of infiltrated CNF into porous PDMS foam, fabricated using the indirect method, for all four different concentrations of CNF/THF suspensions. The weight of the foam cubes was measured before and after ultrasonic agitation, and difference between these weights were considered as the weight of infiltrated CNF. The nanocomposites exhibited a larger CNF infiltration as it was agitated in suspension with a higher CNF concentration.

Table 3. CNF loading in the porous CNF/PDMS nanocomposites created by the indirect method

CNF/THF concentration (g/L)	Before sonication (g)	After sonication (g)	Infiltrated CNF (wt.%)	Average infiltrated CNF (wt.%)
3	0.2997	0.3025	0.93%	0.92%
	0.2942	0.2972	1.01%	
	0.3102	0.3128	0.83%	
2.5	0.2833	0.2854	0.74%	0.78%
	0.3010	0.3035	0.82%	
	0.2906	0.2929	0.79%	
1	0.2800	0.2812	0.43%	0.47%
	0.2847	0.2860	0.45%	
	0.3061	0.3077	0.52%	
0.5	0.2981	0.2990	0.30%	0.24%
	0.2936	0.2942	0.20%	
	0.2962	0.2968	0.20%	

Chapter 3. Characterizations of Morphology and CNF Adhesive Capacity

The morphologies of pristine porous PDMS foams, and the porous CNF/PDMS nanocomposites created by the direct and indirect methods were examined by a high magnification field emission scanning electron microscope (SEM) (ZEISS, NEON) at 20 kV. The cross section of all samples was sputter coated with a thin layer of gold and palladium alloy for providing a clear observation. This chapter illustrates the pores' size and microstructure of pristine porous PDMS foams with four different porosities. The dispersion quality and distribution of CNF in porous CNF/PDMS nanocomposites created by both methods with low and high CNF loadings were investigated and compared. SEM figures show that CNF is strongly embedded into PDMS of porous nanocomposites created by the direct method, whereas, the majority of CNF loosely attaches to the surface and the pores of porous nanocomposites created by the indirect method. In addition, a double-sided tape experiment is performed to investigate adhesive capacity of CNF with PDMS in porous nanocomposites created by both methods.

3.1 Pristine Porous PDMS Foams

Figure 15 shows the microstructures of 4S, 3S1B, 1S3B, and 4B pristine porous PDMS foams. These figures reveal the sugar crystals completely dissolved and left a 3D interconnected structural PDMS matrix. As shown in Figure 15(a), the dimensions of pores are concentrated at around 500μm, which is close to the size of pure cane sugar crystals. The 3S1B porous PDMS foam, as shown in Figure 15(b), shows most pores have similar size with 4S foam, but several pores have a larger dimension around 1.5 mm. This is due to its template contained 25% demerara sugar crystals by volume. The

pores of 4S and 3S1B foams exhibit a near-rectangular shape. The size of amorphous pores is close to 2mm for 1S3B and 4B foams, as shown in Figure 15(c) and Figure 15(d), respectively. The several pores with a smaller size due to 1S3B template contained 25% pure sugar crystals by volume.

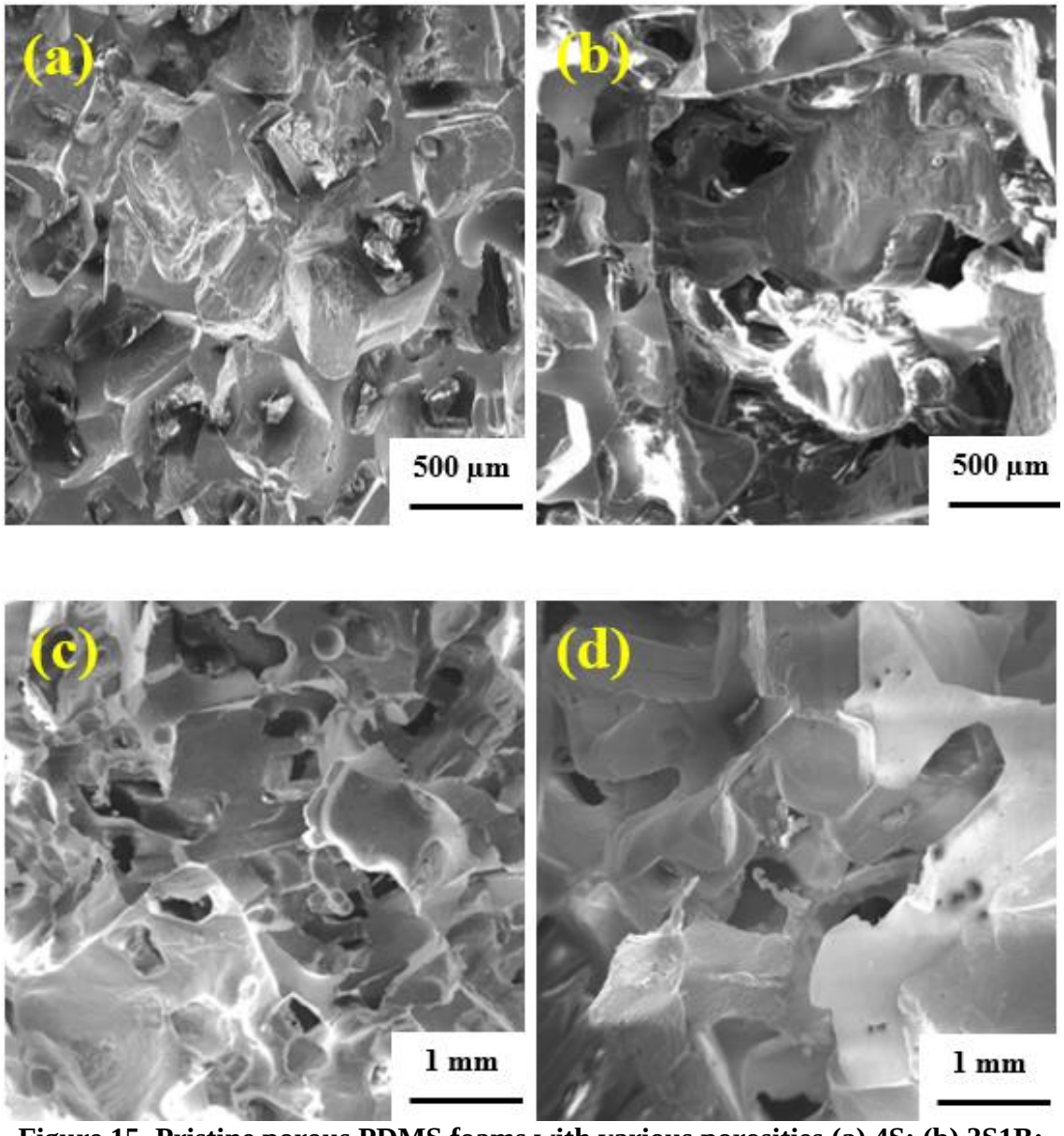
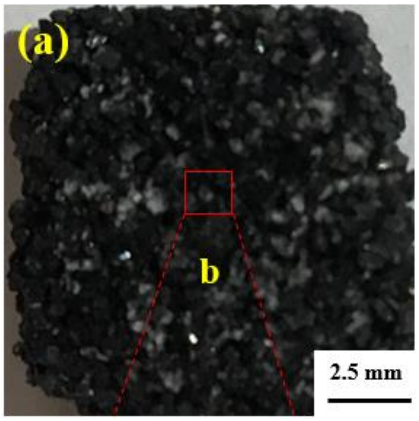


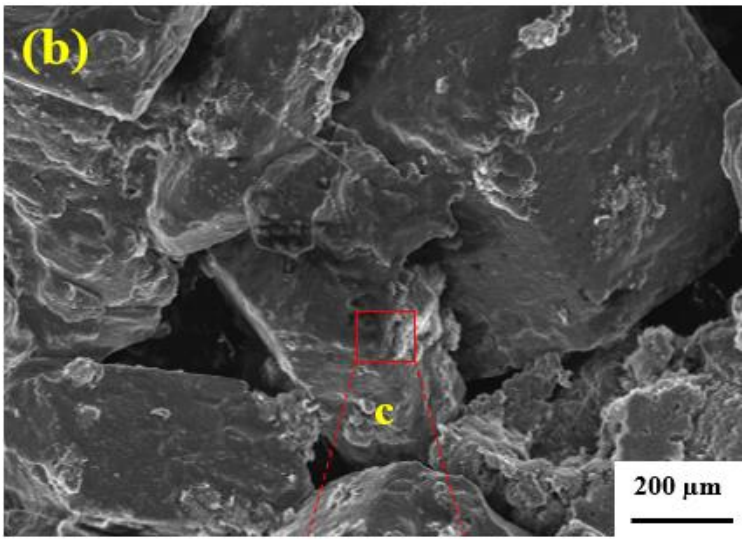
Figure 15. Pristine porous PDMS foams with various porosities (a) 4S; (b) 3S1B; (c) 1S3B; (d) 4B

3.2 Porous CNF/PDMS Nanocomposites

3.2.1 SEM of Porous CNF/PDMS Nanocomposites Created by the Direct Method

Figure 16 shows the morphologies of the CNF coated sugar cube. Figure 16(a) shows the cross section of the CNF coated sugar cube cut from middle center. The several white dots were identified as sugar particles that were dissected by cutting. Figure 16(b) reveals that sugar crystals were packed tightly with small gaps providing space for the liquid PDMS prepolymer to penetrate. The CNF only uniformly coated on the surface of sugar as shown in Figure 16(d). There is no visible CNF in the cross section of sugar particles, Figure 16(e), revealing that no CNF penetrated inside of the sugar crystals during the creation of the CNF coated sugar cube.





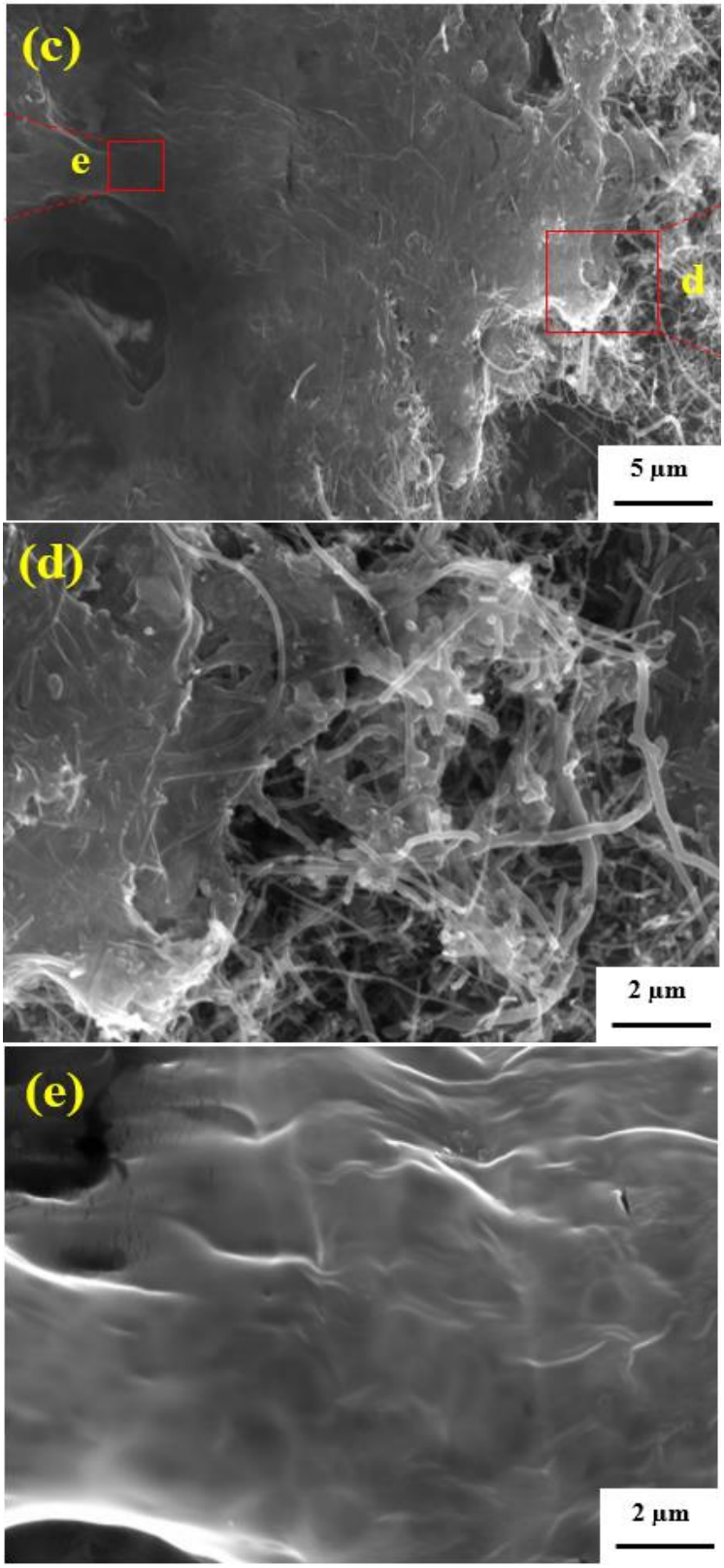
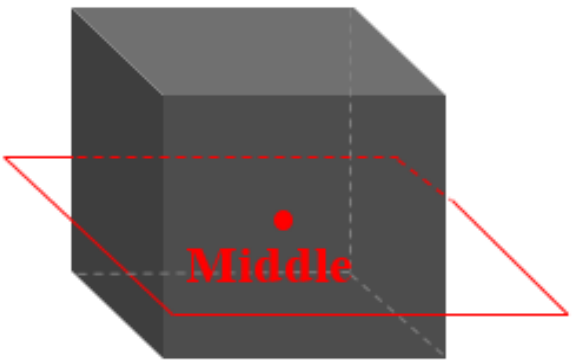
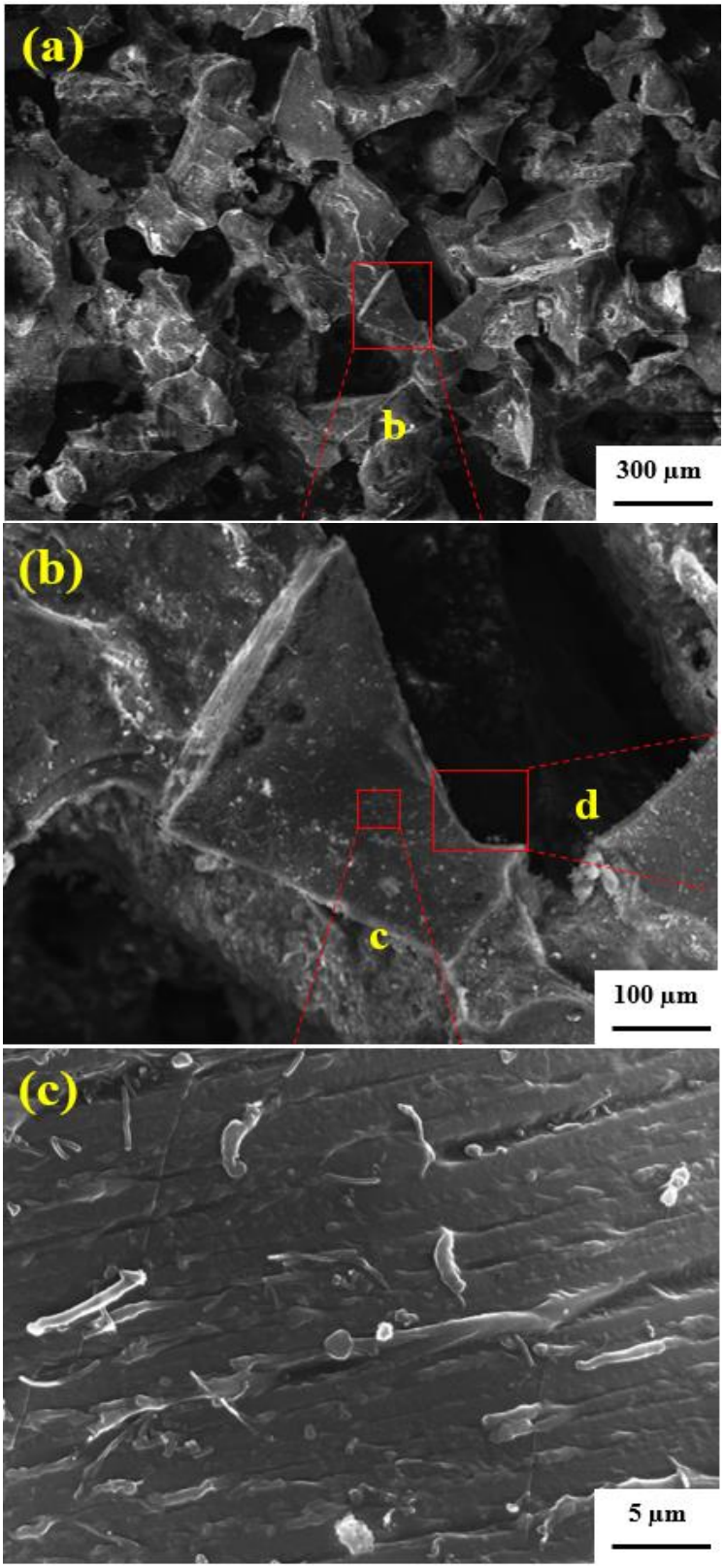


Figure 16. CNF coated sugar cube in different magnifications

Figure 17 and Figure 18 show the morphologies, dispersion quality and distribution of CNF in the porous CNF/PDMS nanocomposites created by the direct method with 1 wt.% and 9 wt.% CNF loading. The samples were cut to reveal their cross section and observed. Figure 17(a) and Figure 18(a) exhibit a similar structure as 4S pristine porous PDMS foam. Figure 17(c) and Figure 18(c) reveal the coated CNF was trapped in the PDMS to generate electric networks. The sample with 9 wt.% CNF loading created more CNF networks than the sample with 1 wt.% CNF loading. The majority of CNF was embedded strongly underneath the PDMS, whereas, only a small quantity of CNF attached to the PDMS. Moreover, there were no entangled nor agglomerated CNF in the PDMS matrix, revealing a uniform CNF dispersion throughout. As stated previously, a poor nanofiller dispersion may lead to unexpected mechanical and electrical properties. This highlights the need to ensure the CNF has a uniform dispersion in the matrix for sensing applications. More CNF distributed on the pore walls (Figure 18(b)) and edges (Figure 18(d & e)) of sample with 9 wt.% CNF loading. The CNF on the sugar crystals left over after the crystals were completely removed and remained penetrated to the cured PDMS matrix. However, only few CNF networks appeared on either edge or the pore walls for the sample with 1 wt.% CNF loading, as depicted in Figure 17(d & e).




(a)
b
300 µm
(b)
d
c
100 µm
(c)
5 µm

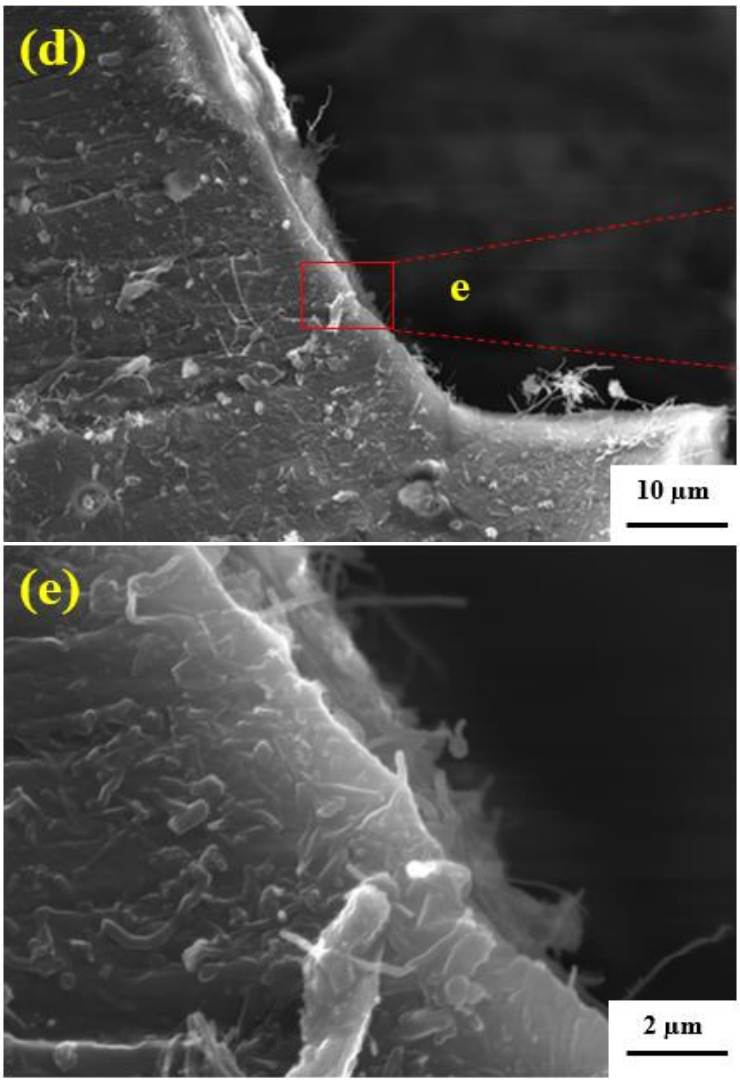
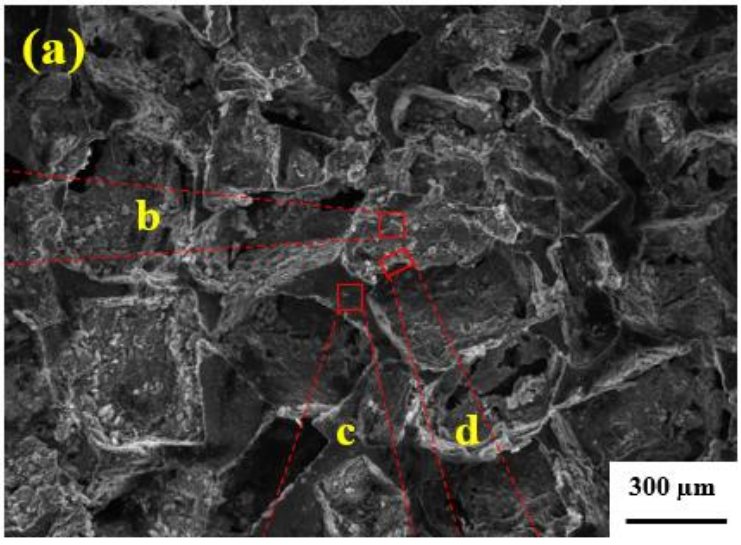
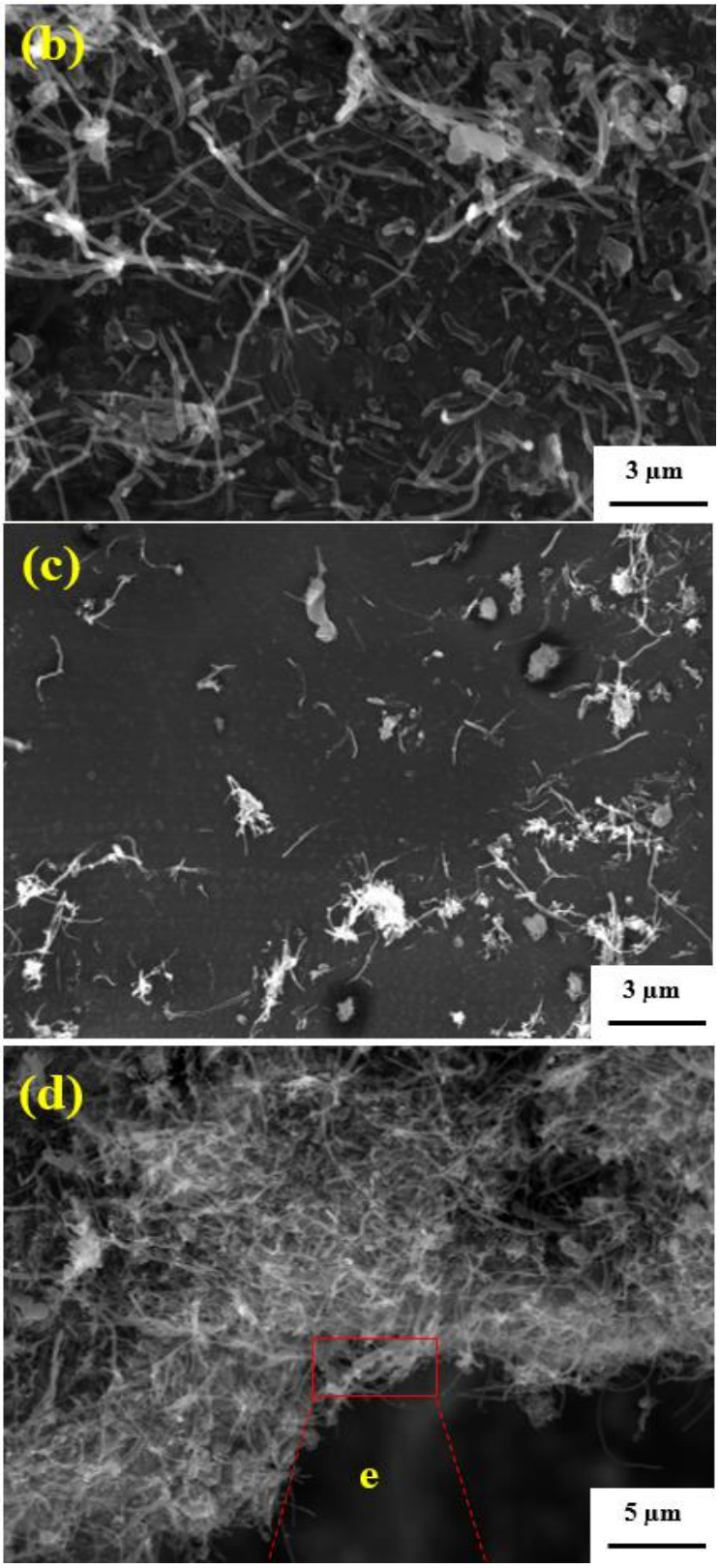


Figure 17. Nanocomposites created by the direct method (1 wt.% CNF) in different magnifications




(b)
3 µm
(c)
3 µm
(d)
e
5 µm

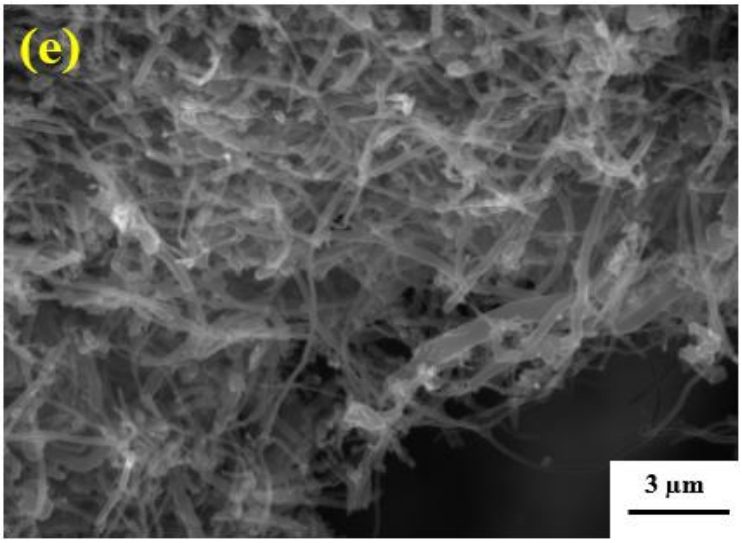
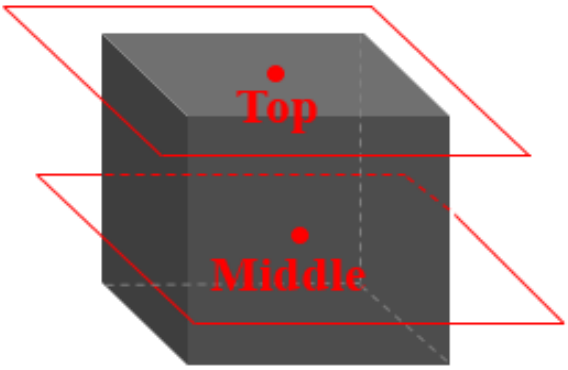


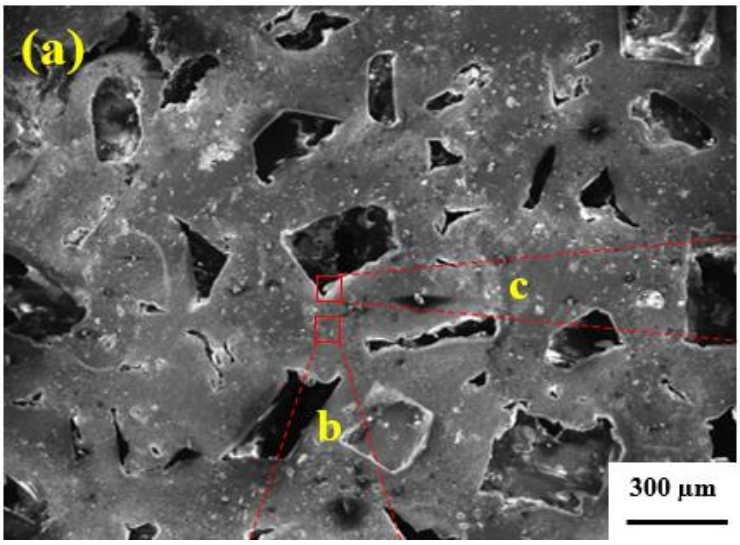
Figure 18. Nanocomposites created by the direct method (9 wt.% CNF) in different magnifications

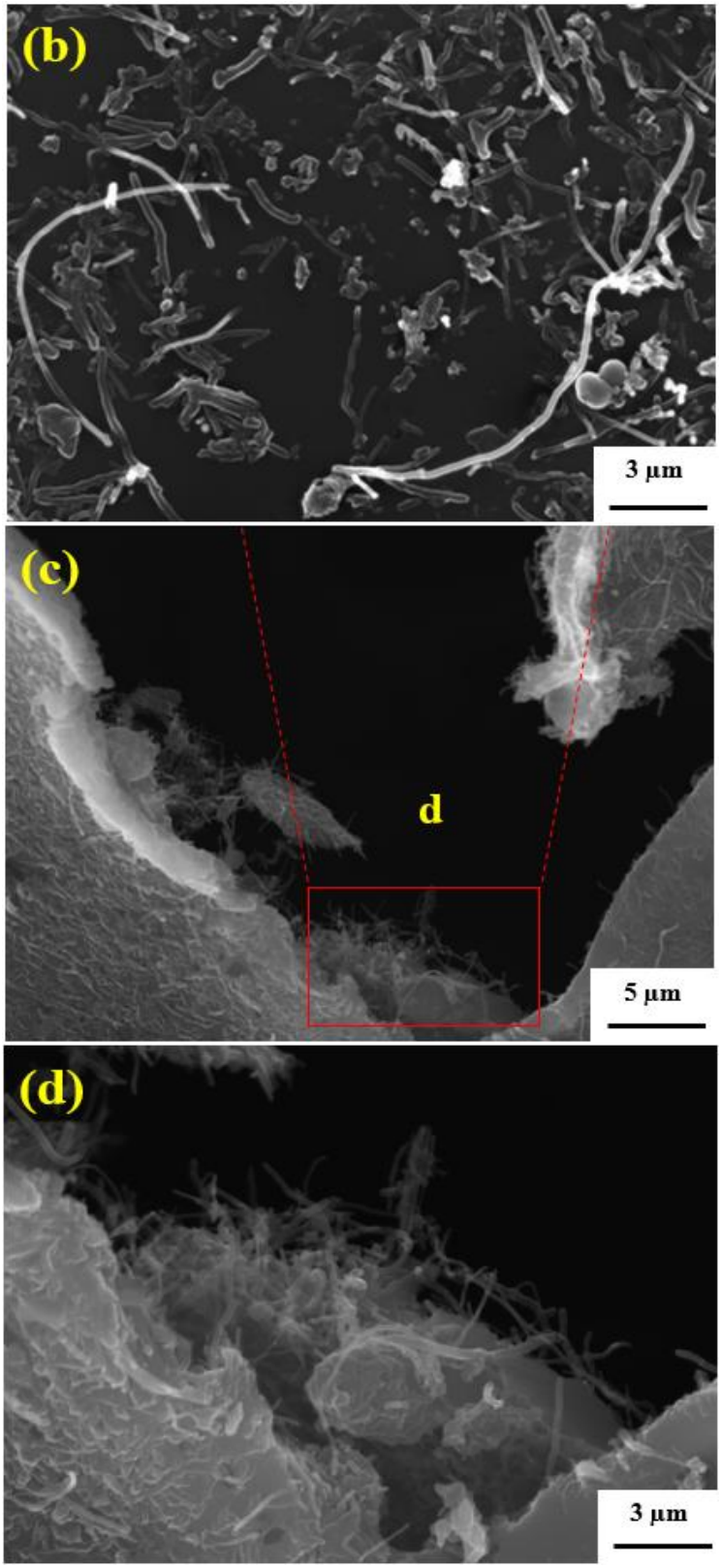
3.2.2 SEM of Porous CNF/PDMS Nanocomposites Created by the Indirect Method

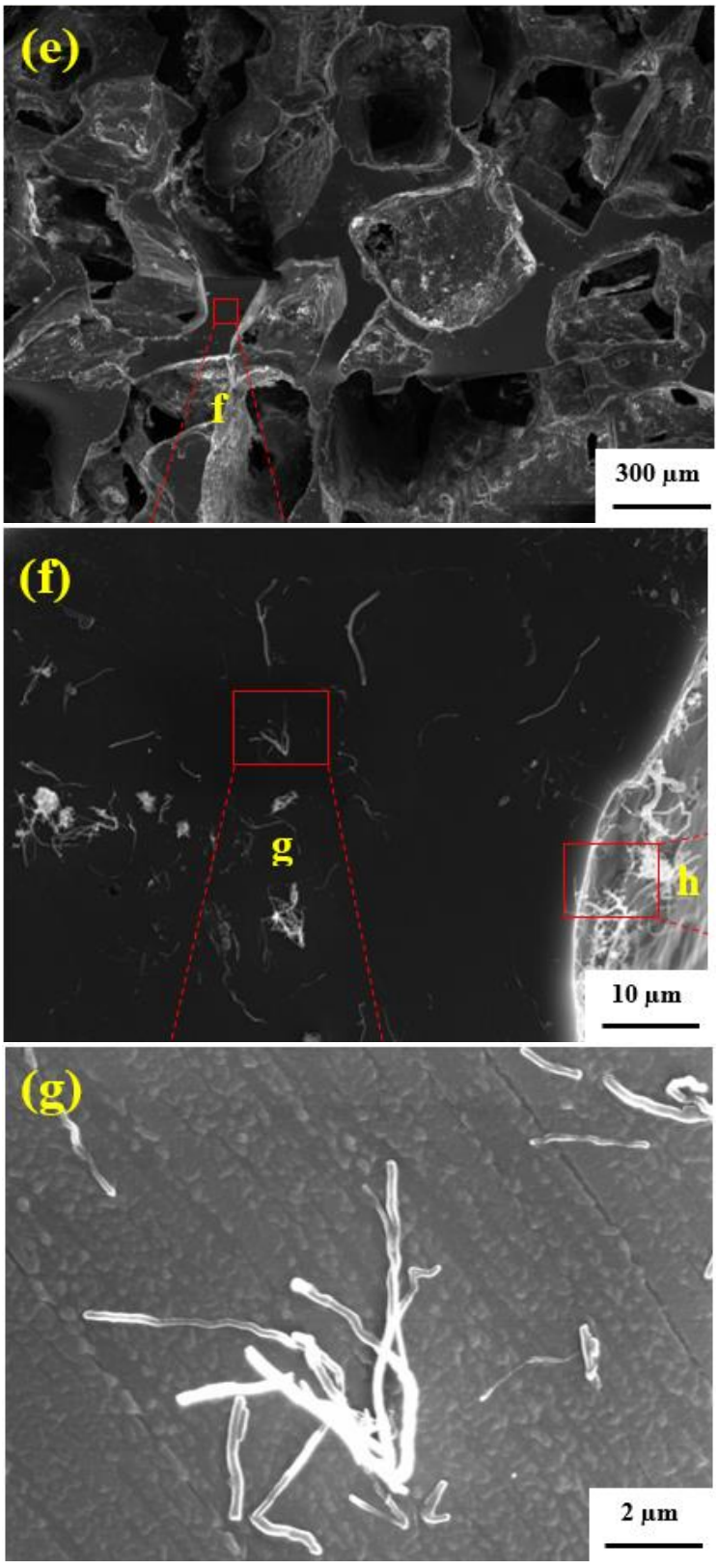
Figure 19(a-d) and (e-h) show the morphologies, dispersion quality and distribution of the CNF on the surface and the middle cross section, respectively, of the porous CNF/PDMS nanocomposites with 0.24 wt.% CNF loading created by the indirect method. Figure 20(a-d) and (e-j) present the surface and the middle cross section, respectively, of the nanocomposites with 0.78 wt.% CNF loading. Figure 19(b & g) and Figure 20(c & g) reveal that the CNF was dispersed uniformly on both the surface and the middle cross section of each sample. The CNF distributed on the surface (Figure 19(b)) and the cross section (Figure 19(f)) of the sample with 0.24 wt.% CNF reveal that majority of CNF was loosely attached to the surface, with very few penetrating into the PDMS matrix. This is due to the concentration of suspension being too low to infiltrate CNF into PDMS. More CNF adhered to the surface (Figure 19 (b)) than penetrated in cross section (Figure 19 (g)). Because the CNF first passed through the surface of the sample, charged on the surface and clogged the pores so that no path was available for CNF to penetrate further. It should be noted that the amount of CNF

deposited on the plane (Figure 19(b) and Figure 20(c)) or edge (Figure 19(d) and Figure 20(d)) of the surface is independent of the concentration of the suspensions. The middle cross section reveal abundant CNF distributed on the edges (Figure 20(h & j)) of sample with 0.78 wt.% CNF loading, compared to the sample with 0.24 wt.% CNF loading (Figure 19(f & h)). Additionally, several CNF chunks appeared inside of the pores of the sample with 0.78 wt.% CNF loading (Figure 20(e & h)). This is due to the CNF violently impinging into the pores under ultrasonic and precipitated as chunks after THF completely evaporated. The sample with 0.24 wt.% CNF loading (Figure 19(e & h)) did not have CNF chunks inside of the pores.






(b)
3 µm
(c)
d
5 µm
(d)
3 µm


(e)
f
300 µm
(f)
g
h
10 µm
(g)
2 µm

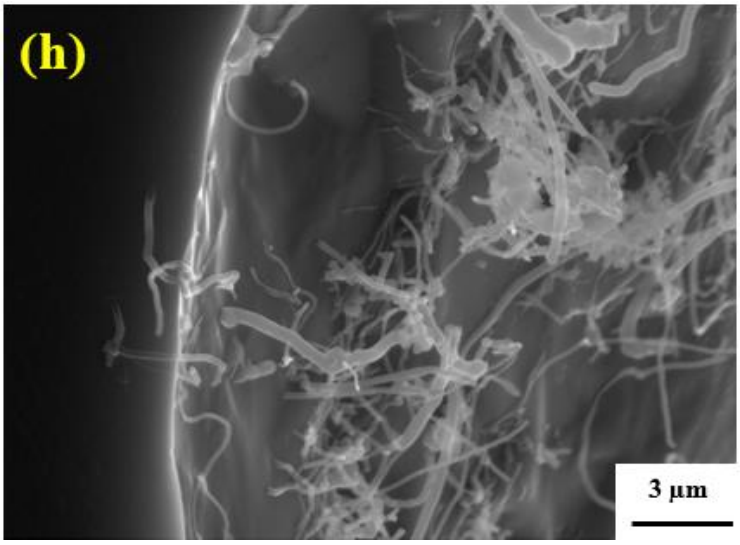
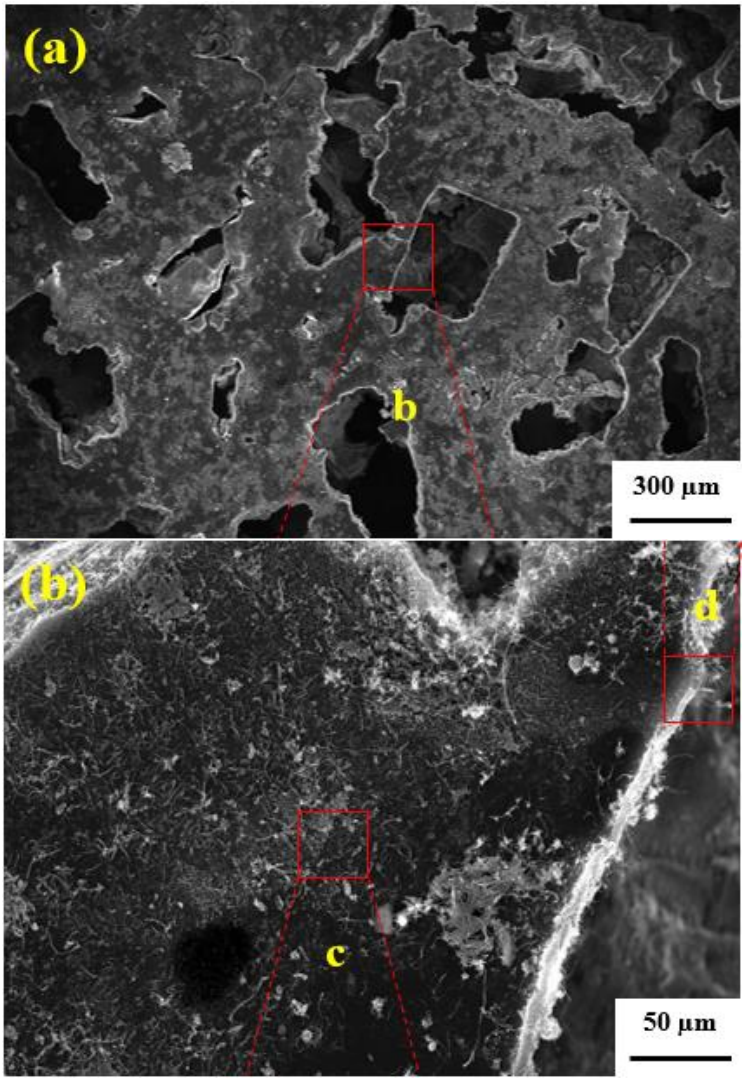
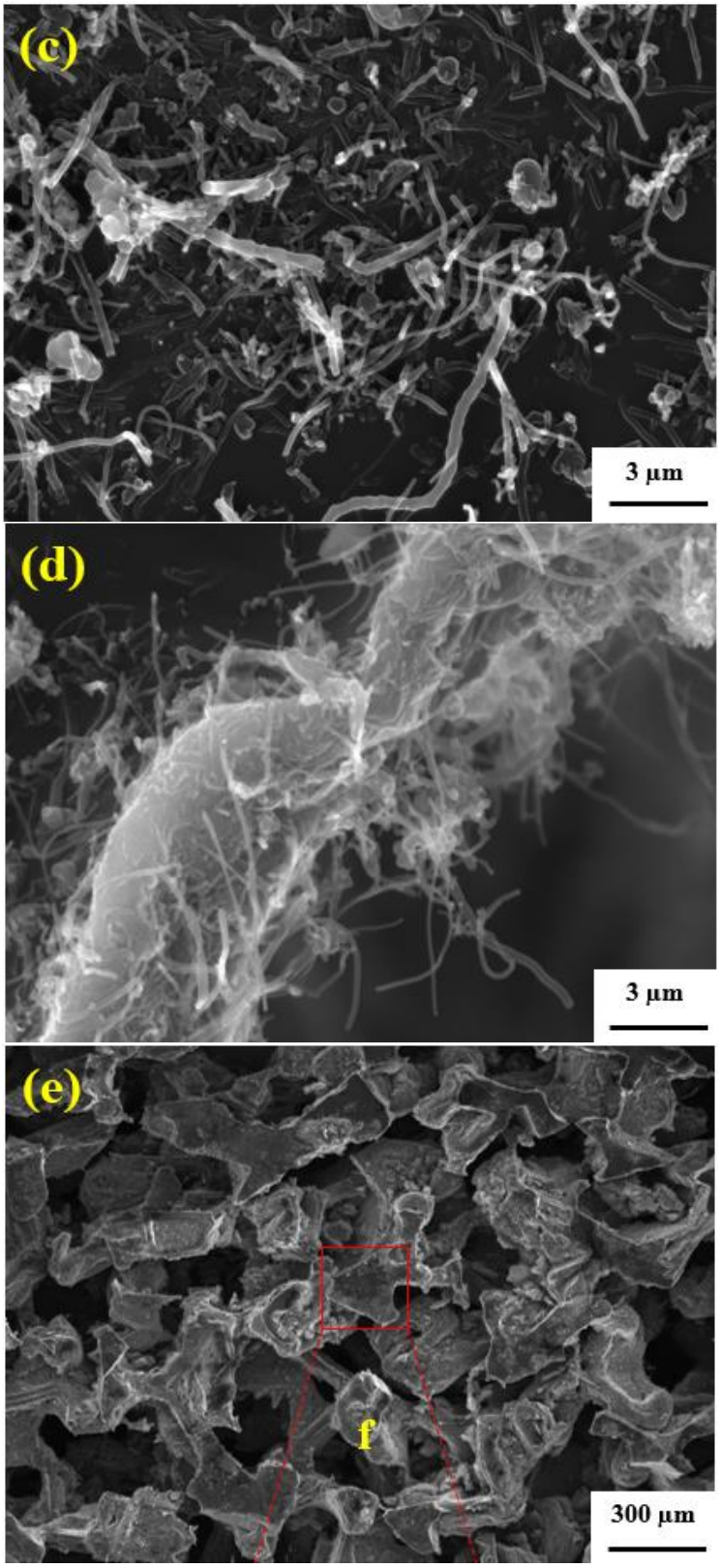
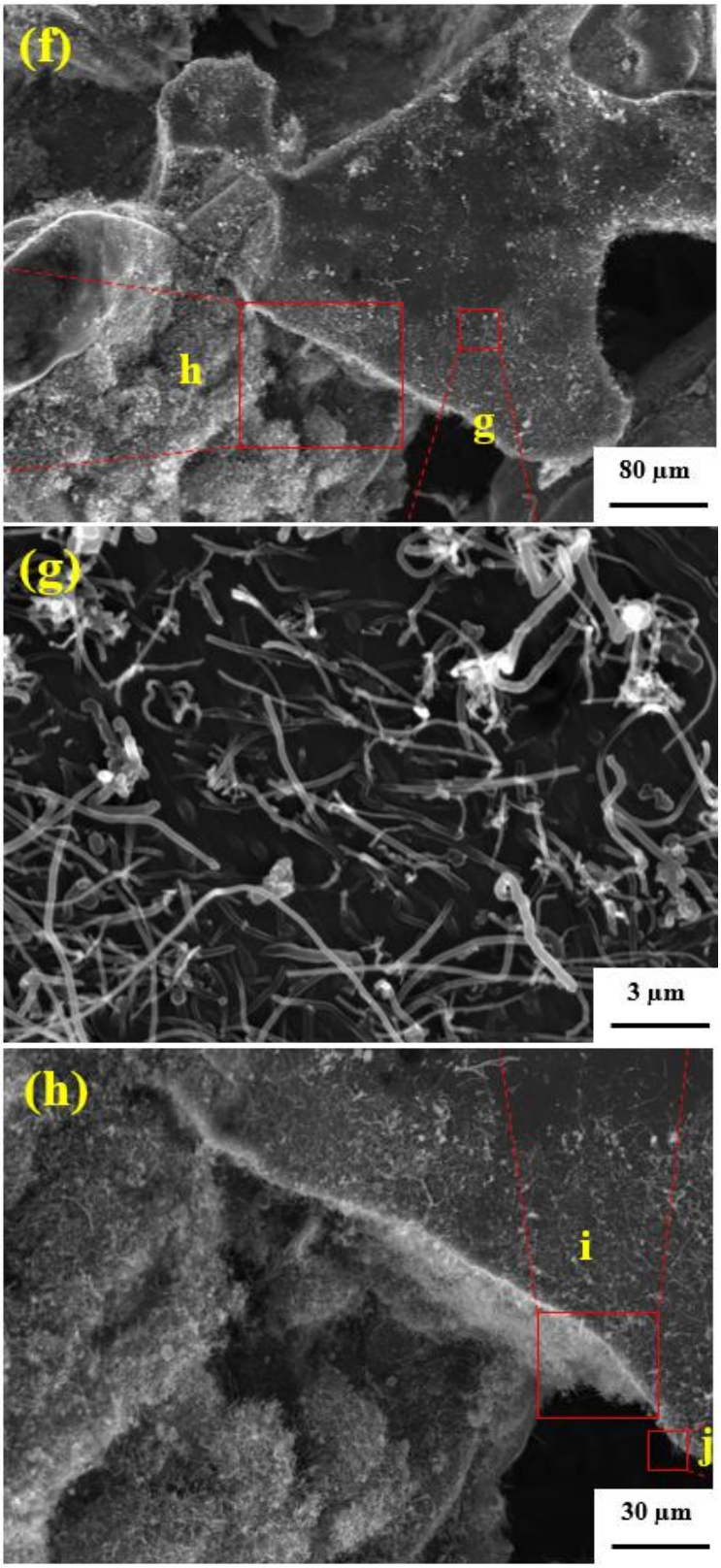


Figure 19. Nanocomposites created by the indirect method (0.24 wt.% CNF) in different magnifications (a-d: top; e-h: middle)




(c)
3 µm
(d)
3 µm
(e)
f
300 µm


(f)
h
g
80 µm
(g)
3 µm
(h)
i
j
30 µm

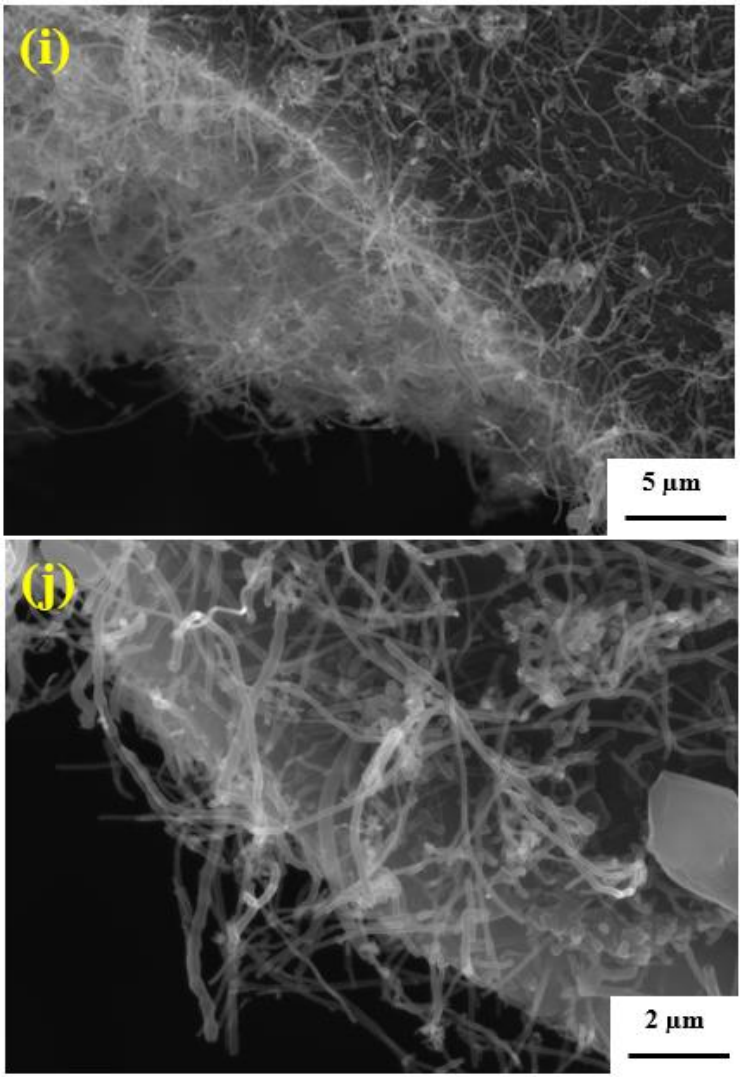


Figure 20. Nanocomposites created by the indirect method (0.78 wt.% CNF) in different magnifications (a-d: top; e-j: middle)

Table 4. The CNF distribution of nanocomposites created by the direct method

Direct method		
	Low concentration (1 wt.% CNF)	**High concentration (9 wt.% CNF)**
CNF at Middle Plane	less	medium
CNF at Middle Edge	less	medium

Table 5. The CNF distribution of nanocomposites created by the indirect method

Indirect method		
	Low concentration (0.24 wt.% CNF)	**High concentration (0.78 wt.% CNF)**
CNF at Top Plane	much	much
CNF at Top Edge	less	less
CNF at Middle Plane	less	much
CNF at Middle Edge	less	chunk

Table 4 and Table 5 include the details of the CNF distribution of porous CNF/PDMS nanocomposites created by both methods with low and high CNF loading based on SEM study. The indirect method can create more CNF electric networks using less amount of CNF. In addition, the CNF chunks only appeared at the middle cross section of porous CNF/PDMS nanocomposites created by the indirect method with a high concentration CNF loading.

3.3 Interfacial Adhesion Study

To investigate the interfacial adhesion property between the porous PDMS matrix and the CNF for nanocomposites created by both methods, a double-sided tape pressing experiment was performed. Samples created by both methods were initially placed on double-sided tape without any pressure, as shown in Figure 21(a). Samples were then subjected to a compressive load to deform equally. This load was applied and released three times, for both samples, simultaneously. Samples were then peeled from the tape. Clearly, more CNF was peeled from the sample created by the indirect method due to weak CNF-PDMS adhesion, as shown in Figure 21(b). In the direct method, the sugar crystals were first coated with CNF; thus, the majority of CNF was fully wrapped by PDMS prepolymer and embedded into cured PDMS. In the indirect method, however, CNF introduced into cured pristine porous PDMS foam. Thus, most CNF was weakly attached to the pore walls, leaving the CNF exposed. This shows that

nanocomposites created by the direct method endow a stronger interfacial adhesion. This is an important consideration for designing wearable sensors because a weak CNF-PDMS adhesion can cause environmental pollution resulting in health issues for anyone nasally ingesting CNF [42].

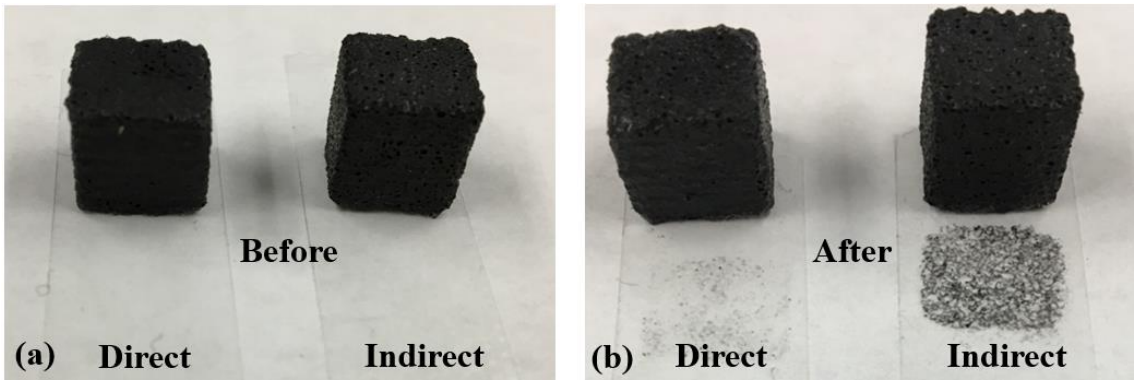


Figure 21. Double-sided tape experiment (a) Before; (b) After

Chapter 4. Material and Mechanical Properties: Porosity, Young's Modulus, and Electrical Properties

In the recent past, Huang et al. [30] reported the tensile elastic modulus (1.45 Mpa-1.96Mpa) and Poisson's ratios (0.32-0.44) of pristine porous PDMS foams with porosity range from 16% to 22%. Rinaldi et al. [23] reported the Young's modulus for pristine porous PDMS foam was 0.11 MPa (10:1 weight ratio of PDMS) and 0.065 MPa (20:1 weight ratio of PDMS). Han et al. [10] reported the Young's modulus increased with the larger compressive strain varies from 0.02 MPa to 0.2 MPa. To better understand the behavior of potential applications of porous PDMS foam, the material and mechanical properties are crucial to determine and predict.

Some researchers also performed numerical computations to find mechanical properties of porous materials. Lantada et al. [43] illustrated the Young's modulus and tensile strength of pristine porous PDMS foam relied on its porosity, density, and structure. Saha et al. [44] reported the structural response of polymer foam also depended on the closed or open cell and the gas flow rate in the cell. Hence, porous PDMS foams with a complicated microstructure indeed left a computation challenge.

This chapter discusses densities and Young's modulus of pristine porous PDMS foams with different porosities. It is noted that the Young's modulus of can be properly predicted by a polynomial equation by a known density. Moreover, the Young's modulus and electrical properties of nanocomposites created by the direct and indirect methods with a series of CNF loadings are measured and compared.

4.1 Density and Porosity of Pristine Porous PDMS Foams

The porosity of the foam is defined as the volume fraction of void over the total volume as a percentage between 0% and 100%. The porosity of foam [45] is calculated by equation:

$$\Phi = (1 - \frac{\rho_{foam}}{\rho_{PDMS}}) * 100\% \quad (1)$$

where Φ is porosity of foam, ρ_{foam} and ρ_{PDMS} are the density of porous PDMS foam and density of the solid PDMS.

The porosity of solid PDMS was considered as 0% because no visible pores appeared in solid PDMS sample, as shown in Figure 22. The average density of five solid PDMS cubes was 1.0021 g/cm³, as shown in Table 6, measured by the AccuPyc II 1240 pycnometer. The experimental results show only 3% difference compare to the theoretical result of 1.03 g/cm³ by the safety data sheet [46]. The gas pycnometer is identified as the most accurate instrument to measure density of solid material.

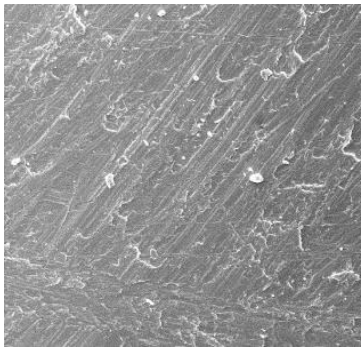


Figure 22. Morphology of solid PDMS cube

Table 6. Density of solid PDMS cubes measured by pycnometer

Sample #	Density (g/cm³)
1	1.018
2	1.0062
3	1.0142
4	0.9895
5	0.9826
Average	1.0021

The weight of each single pristine porous PDMS foam cube was measured by a laboratorial digital scale with four decimal places. The dimensions of pristine porous PMDS foams were measured by a caliper with two decimal places. The volume and density are calculated by equations:

$$V_{PDMS} = \text{Length} * \text{Width} * \text{Height} \quad (2)$$

$$\rho_{foam} = \frac{m_{foam}}{v_{PDMS}} \quad (3)$$

The density of each type of porous PDMS foam was determined by the average of ten samples as shown in Table 11. The 4B porous PDMS foam displayed the largest porosity 77.38% and smallest density 0.2266 $\frac{g}{cm^3}$, while, 4S porous PDMS foam displayed the smallest porosity as 68.48% and largest density 0.3159 $\frac{g}{cm^3}$.

Table 7. Density and Porosity of 4S pristine porous foams

Sample #	4S			
	Weight (g)	**Volume (cm^3)**	**Density (g/cm^3)**	**Porosity**
1	0.3123	0.9992	0.3126	68.8%
2	0.3239	1.0159	0.3188	68.2%
3	0.3313	1.0169	0.3258	67.5%
4	0.3074	0.9897	0.3106	69.0%
5	0.3222	1.0394	0.3100	69.1%
6	0.3209	1.0047	0.3194	68.1%
7	0.3125	0.9953	0.3140	68.7%
8	0.3321	1.0331	0.3215	67.9%
9	0.3210	1.0139	0.3166	68.4%
10	0.3079	0.9944	0.3096	69.1%
Average	0.3192	1.0102	0.3159	68.48%

Table 8. Density and Porosity of 1B3S pristine porous foams

Sample #	1B3S			
	Weight (g)	Volume (cm^3)	Density (g/cm^3)	Porosity
1	0.2859	1.0067	0.2840	71.7%
2	0.2696	0.9964	0.2706	73.0%
3	0.2744	0.9964	0.2754	72.5%
4	0.2936	1.0128	0.2899	71.1%
5	0.2850	1.0223	0.2788	72.2%
6	0.2896	1.0278	0.2818	71.9%
7	0.2882	1.0265	0.2808	72.0%
8	0.2897	1.0162	0.2851	71.6%
9	0.2799	1.0140	0.2760	72.5%
10	0.2869	0.9954	0.2882	71.2%
Average	0.2843	1.0114	0.2811	71.95%

Table 9. Density and Porosity of 1S3B pristine porous foams

Sample #	1S3B			
	Weight (g)	Volume (cm^3)	Density (g/cm^3)	Porosity
1	0.2511	1.0234	0.2453	75.5%
2	0.2685	1.0273	0.2614	73.9%
3	0.2432	1.0081	0.2412	75.9%
4	0.2494	1.0222	0.2440	75.7%
5	0.2552	1.0105	0.2526	74.8%
6	0.2635	1.0004	0.2634	73.7%
7	0.2424	0.9861	0.2458	75.5%
8	0.2446	1.0059	0.2432	75.7%
9	0.2393	0.9634	0.2484	75.2%
10	0.2443	0.9937	0.2458	75.5%
Average	0.2502	1.0041	0.2491	75.14%

Table 10. Density and Porosity of 4B pristine porous foams

Sample #	4B			
	Weight (g)	Volume (cm^3)	Density (g/cm^3)	Porosity
1	0.2145	0.9275	0.2313	76.9%
2	0.2156	0.9897	0.2179	78.3%
3	0.2086	0.8900	0.2344	76.6%
4	0.2354	0.9961	0.2363	76.4%
5	0.2185	0.9538	0.2291	77.1%
6	0.2088	0.8992	0.2322	76.8%
7	0.2108	0.9229	0.2284	77.2%
8	0.2057	0.9419	0.2184	78.2%
9	0.2284	1.0308	0.2216	77.9%
10	0.2057	0.9483	0.2169	78.4%
Average	0.2152	0.9500	0.2266	77.38%

Table 11. Average density and porosity of pristine porous foams

Type	Small sugar volume ratio	Density (g/cm^3)	Porosity
4S	100%	0.3159	68.48%
1B3S	75%	0.2811	71.59%
1S3B	25%	0.2491	75.14%
4B	0%	0.2261	77.38%

The relationships between porosity/density and small sugar volume percentage are shown in Figure 23 and Figure 24. The density or porosity are possible to predict by knowing volume ratio of small and big sugar. In this way, it is possible to fabricate porous PDMS foam with desired porosity by altering the volume ratio of pure and demerara cane sugar referring to the prediction equations.

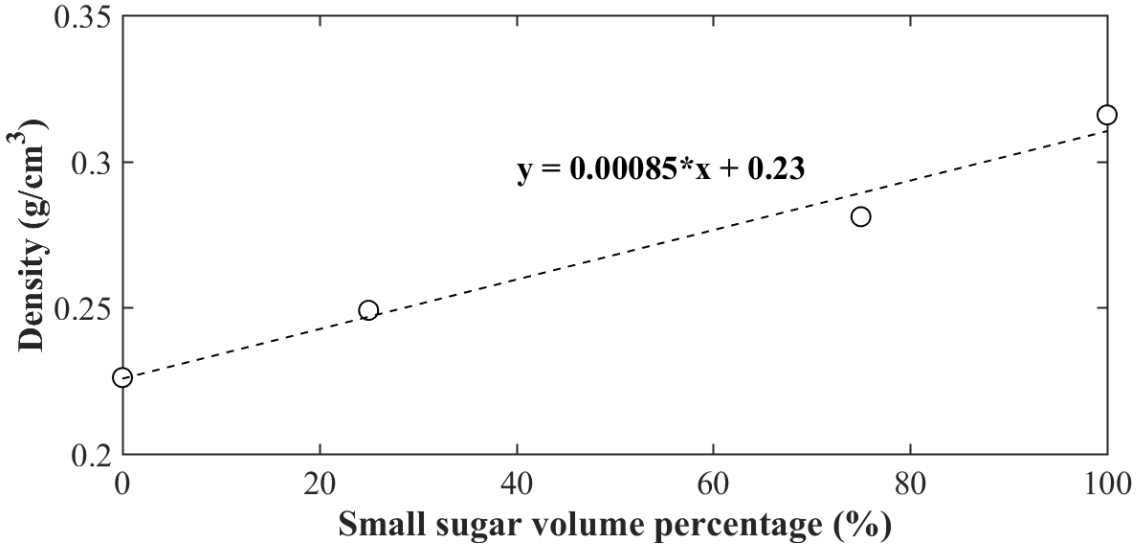


Figure 23. Relationship between density of pristine porous PDMS foam and small sugar volume percentage

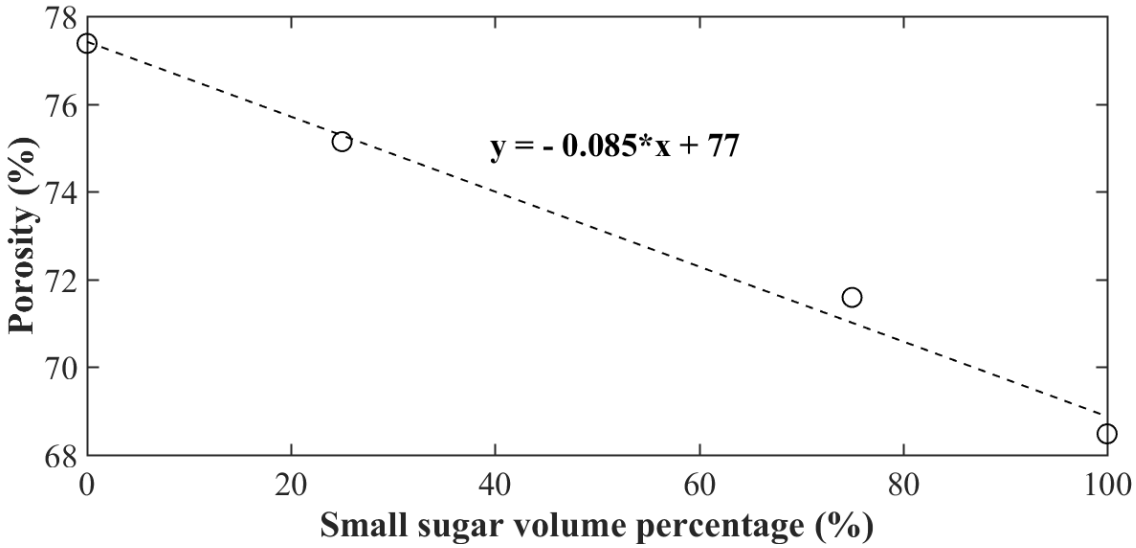


Figure 24. Relationship between porosity of pristine porous PDMS foam and small sugar volume percentage

4.2 Quasi-static Compressive Test

Solid and four types of porous PDMS foams were subjected to uniaxial quasi-static compression test on Instron 5900 linear variable differential transformer (LVDT) universal testing machine with 100 N load cell. A 0.1N initial force was applied to avoid slippage at the beginning of the test. The crosshead velocity was 1mm/min, followed as the ASTM D695 [47].

The compressive stress-strain curve of solid PDMS cube and each type of porous PDMS foams are shown in Figure 25 and Figure 26, respectively. As shown in Figure 26, the 4S sample was induced the most stress than others at high deformation region, which presented the highest stiffness along with other types of foam. At the higher compressive deformation region foam was envisaged as a compact solid sample after the cell walls completely collapsed; thus, stress increase sharply as more compressive strain induced.

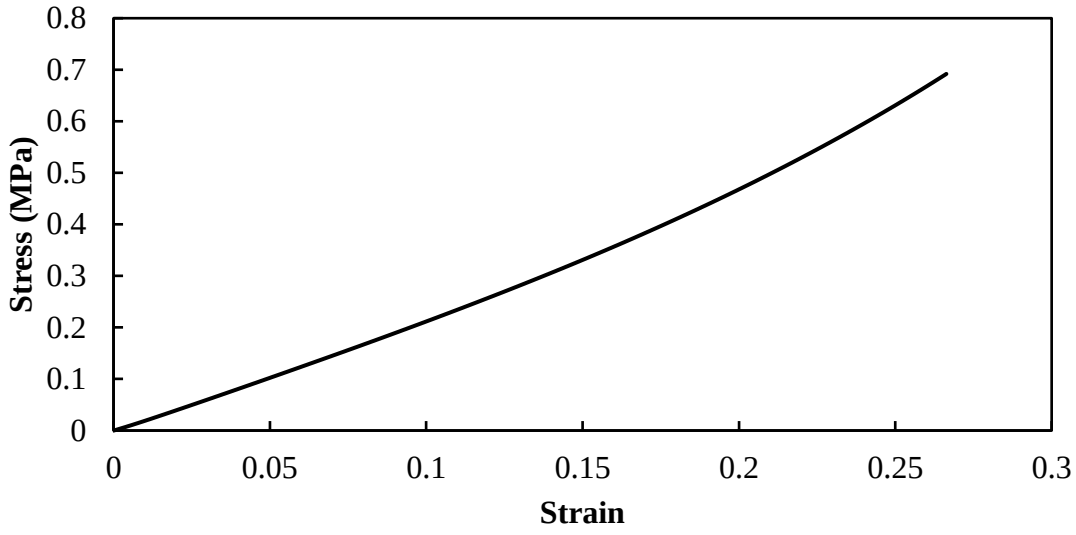


Figure 25. Stress-strain curve of solid PDMS cube

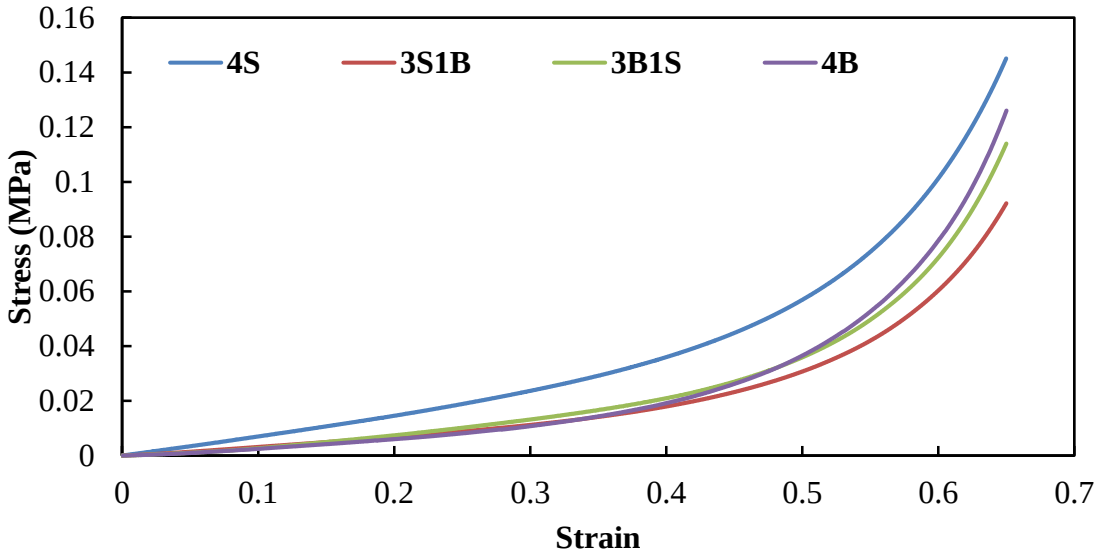


Figure 26. Stress-strain curve of pristine porous PDMS foam

4.3 Mechanical Property (Young's Modulus) of Pristine Porous PDMS Foams

4.3.1 The Young's Modulus of Pristine Solid PDMS and Porous PMDS Foams

The Young's modulus is a measurement of the stiffness of material under linear elasticity region. It describes the relationship between stress and strain. The Young's modulus is determined by the Hooke's Law:

$$\mathrm{E} = \frac{\sigma}{\varepsilon} \tag{4}$$

where E is the compressive Young's modulus, σ and ε is the applied stress and resultant strain within linear stress-strain region.

The Young's modulus of solid PDMS cube was determined by the slope of stress-strain curve within linear elasticity region, up to around 10% maximum compressive strain, as shown in Figure 27. It was measured by the slope of linear trendline with R-squared value around 99.95%. The average Young's modulus of three samples was 2.2943 MPa with a density of 1.0023 g/cm³, as shown in Table 12.

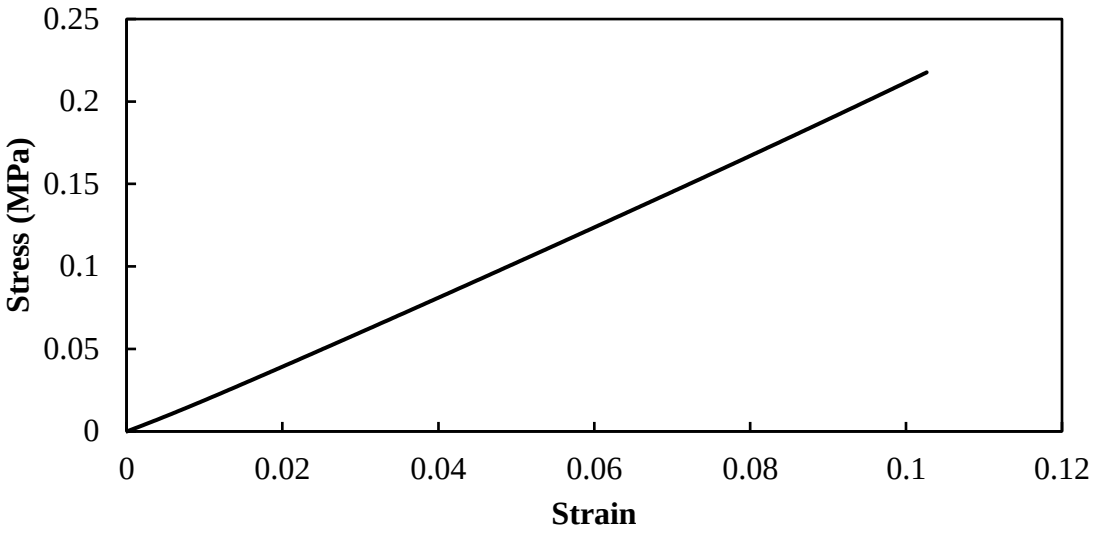


Figure 27. Stress-strain curve of solid PDMS cube within linear elasticity region

Table 12. The Young's modulus of solid PDMS cubes

Sample #	Young's Modulus (MPa)	Density (g/cm^3)
1	2.3226	1.0180
2	2.3118	1.0062
3	2.2484	0.9826
Average	2.2943	1.0023

Figure 28 illustrates the linear elasticity region for 4S and 3S1B samples were up to about 21%, whereas, for the 3B1S and 4B samples were only about 4% compressive strain. Over the linear elasticity region, the stress increased sharply with inducing strain. Table 13 illustrates the Young's modulus and corresponding density of porous pristine PDMS foam with different porosities. Three samples of each type sample were characterized.

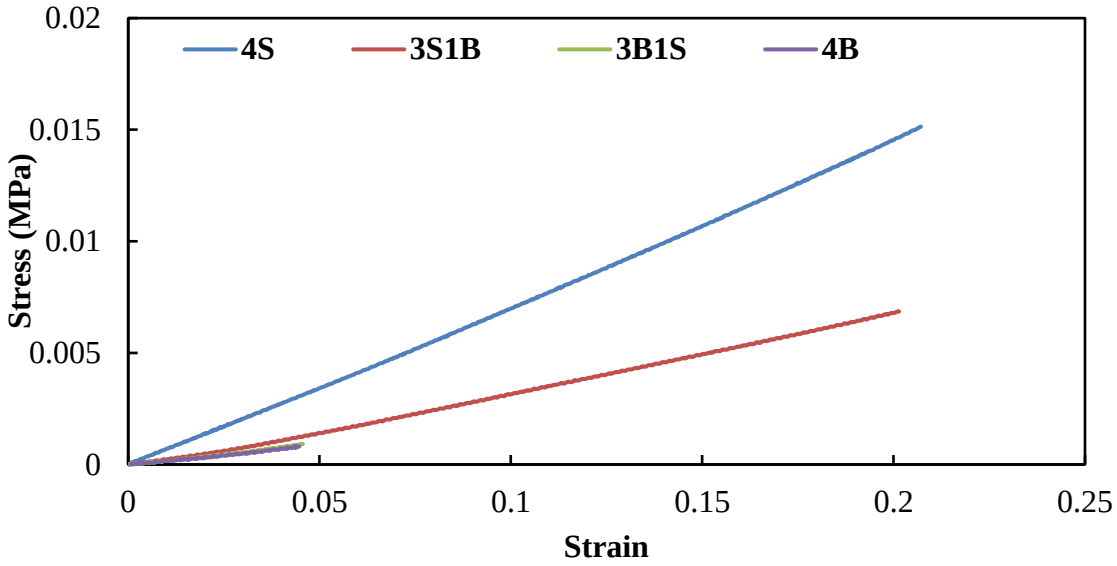


Figure 28. Stress-strain curve of pristine porous PDMS foam within linear elasticity region

Table 13. Young's modulus and density of pristine porous PDMS foams

	Sample #	Young's Modulus (MPa)	Density (g/cm³)
4S	1	0.0635	0.3126
	2	0.0728	0.3188
	3	0.0748	0.3258
3S1B	1	0.0354	0.2840
	2	0.0298	0.2706
	3	0.0324	0.2754
3B1S	1	0.0194	0.2454
	2	0.0278	0.2613
	3	0.0187	0.2412

4.3.2 Robustness of Mechanical Performance

The 4S pristine porous PDMS foam is the best choice for developing sensing applications, because it presented the highest Young's modulus and the widest linear elasticity region. In addition, 4S sugar template was produced easily because the fine sugar crystals were most likely to be packed tightly as template. To validate 4S sample endows an excellent robust mechanical performance, it is essential to investigate the

effect of strain rates on the Young's modulus. Strain rate is defined as the ratio of cross-head speed to original sample height. As shown in Figure 29, the robustness of the 4S sample was demonstrated under quasi-static compressive tests and strain rates varied over orders of magnitude. As shown in Figure 30, there was less than 5% difference in Young's modulus when strain rates were varied from 0.00016s^{-1} to 0.016 s^{-1}. However, the difference increased to about 10% when the strain rate increased to 0.16 s^{-1}. Thus, the Young's modulus of 4S foam had a negligible increasements as the strain rate increased up to 0.016 s^{-1}. It indicated a strong mechanical robustness of 4S pristine porous PDMS foam. Rinaldi et al. [23] reported that porous PDMS foam displayed sensitive mechanical behaviors dependent on strain rates.

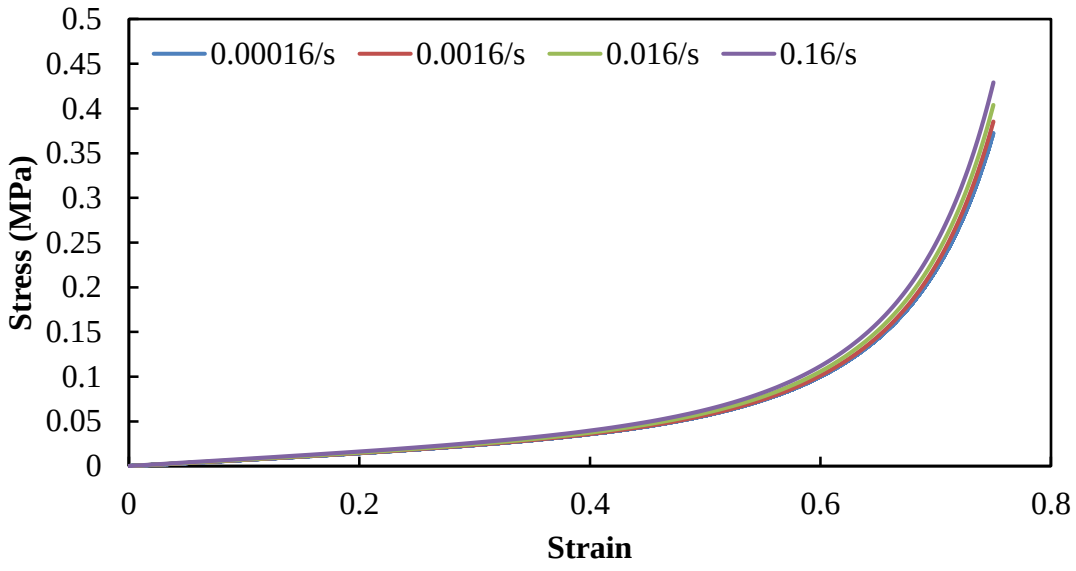


Figure 29. Stress-strain curve of 4S pristine porous PDMS foam with various strain rates

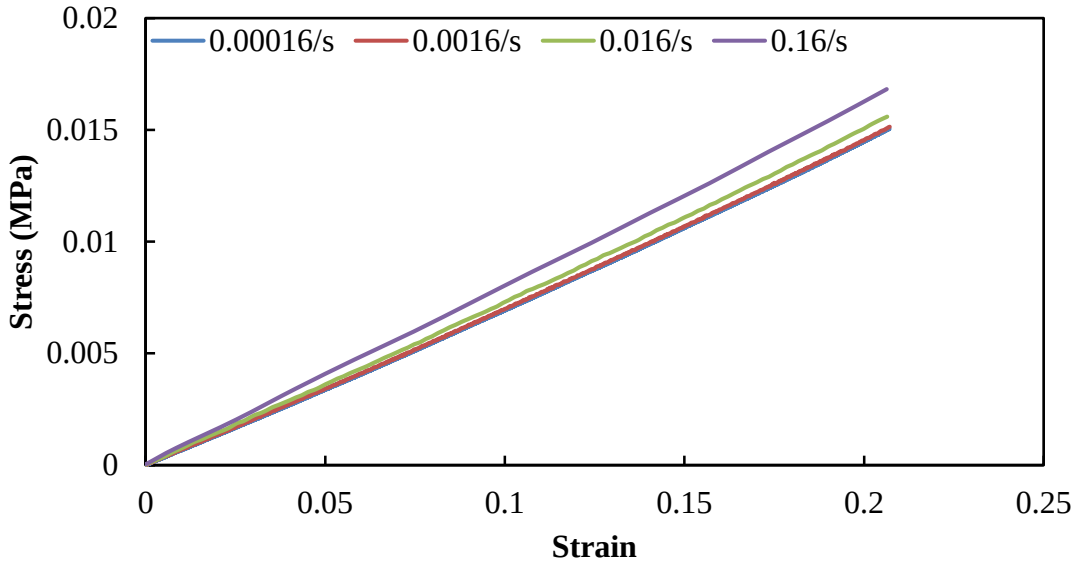


Figure 30. Stress-strain curve of 4S pristine porous PDMS foam within linear elasticity region with various strain rates

Table 14. Young's modulus under different strain rates of 4S pristine PDMS foam

Strain Rate (s^{-1})	Young's Modulus (MPa)
0.00016	0.0710
0.0016	0.0714
0.016	0.0741
0.16	0.0808

4.3.3 Prediction of the Young's Modulus

To better understand the mechanical performance of porous PDMS foam applications, the Young's modulus is crucial to determine first. When porous PDMS foam is compressed, it deforms linearly with respect to stress until the pore walls start to buckle. In this region, the Young's modulus of porous material could be predicted based on its density and strain rate, $E_f, E_s = f(\rho_f, \rho_s, \dot{\varepsilon})$ [10]. However, the Young's modulus and mechanical behavior of pristine PDMS foam displayed a negligible change as the strain rate increased from 0.00016s^{-1} to 0.016 s^{-1}. The strain rate did not affect the mechanical property of porous pristine PDMS foam. Thus, the relationship between

Young's modulus and density can be expressed in a polynomial equation regardless of strain rate:

$$\frac{E_f}{E_s} = C_1(\frac{\rho_f}{\rho_s})^{C_2} \quad (5)$$

where C_1 and C_2 are constants, E_f and E_s are Young's modulus of porous PDMS foam and solid PDMS, ρ_f and ρ_s are the density of porous PDMS foam and solid PDMS, respectively.

To solve the fitted polynomial equation, the density and Young's modulus ratios between each nine pristine porous PDMS foams (refer as Table 13) and the average of solid PDMS (refer as Table 12) were substituted into Equation 5, and generated a prediction equation $E_f/E_s = 7.1977(\rho_f/\rho_s)^{4.7937}$ with R-square around 0.99, as shown in Figure 31. The Young's modulus of 4B porous PDMS foams were calculated based on the prediction equation and only displayed around 6% error between predicted and experimental results, as shown in Table 15. Therefore, this equation is a proper way to predict the Young's modulus of pristine PDMS foams (porosity range is from 67% to 78%) by a known density.

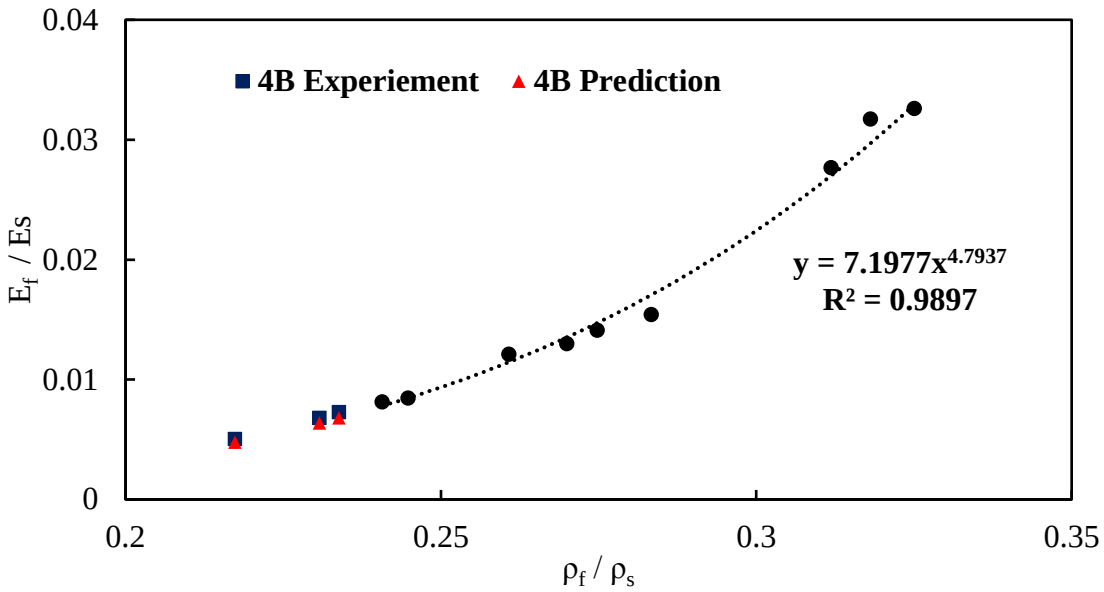


Figure 31. Prediction of the Young's modulus

Table 15. Experimental Vs. Predicted Young's Modulus

4B Porous Pristine PDMS Foam				
Sample #	**Density (g/cm³)**	**Experimental Young's Modulus (MPa)**	**Predicted Young's Modulus (MPa)**	**Error**
1	0.2313	0.0156	0.0146	-6.29%
2	0.2179	0.0116	0.0110	-5.37%
3	0.2344	0.0167	0.0156	-6.69%

4.4 Mechanical behavior of Porous CNF/PDMS Nanocomposites

4.4.1 Porous Nanocomposites Created by the Direct Method

The quasi-static compressive tests were performed to nanocomposites created by the direct method with different CNF loading. As expected, as shown in Figure 32 and Figure 33, nanocomposites loaded with CNF increased the Young's modulus, because CNF is treated as hard skeletons to support load. Moreover, the stiffness and the Young's modulus increased with more CNF loading. The sample with 3 wt.% CNF loading increased Young's modulus from 0.0693 MPa to 0.1046 MPa. When the sample deformed over the linear elasticity region, the stress of nanocomposites with 9 wt.%

CNF loading increased rapidly. It is noticed that the linear elasticity region of all samples was ended at 21% compressive strain regardless of the amount of CNF loading.

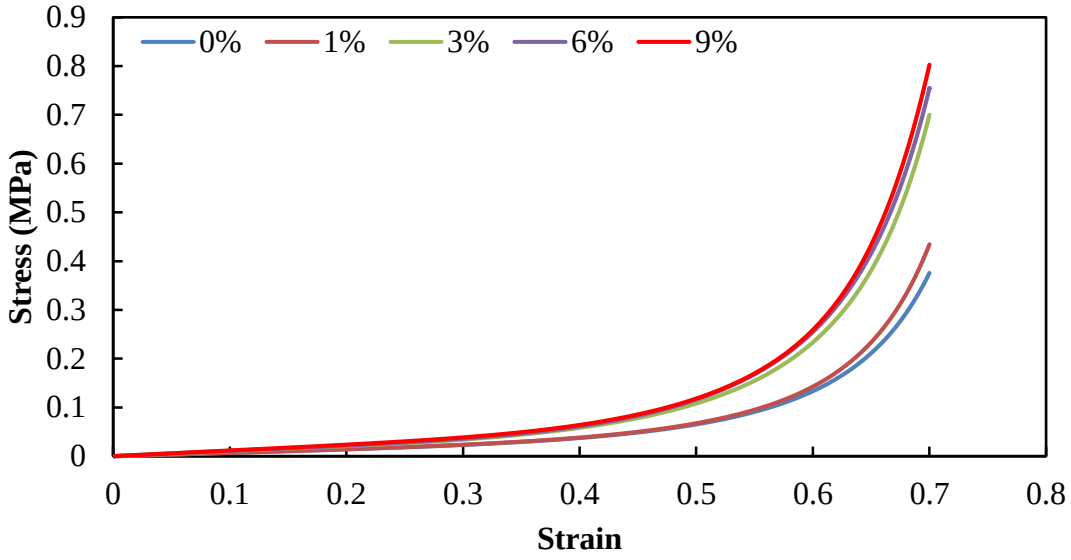


Figure 32. Stress-strain curve of porous nanocomposites created by the direct method with various amount of CNF loading

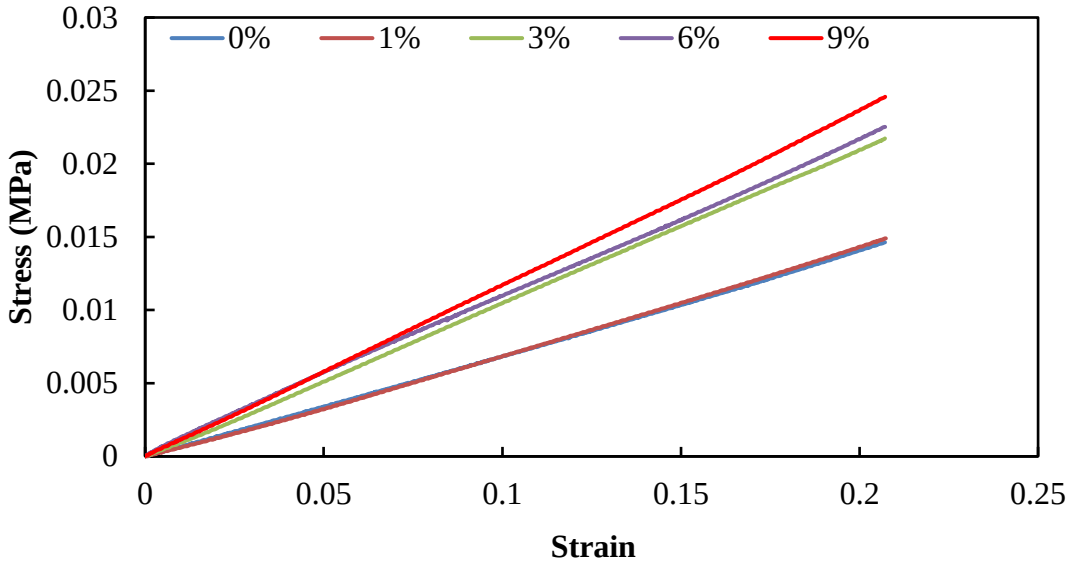


Figure 33: Stress-strain curve of porous nanocomposites created by the direct method with various amount of CNF loading within linear elasticity region

Table 16. Young's modulus of porous nanocomposites created by the direct method with various amount of CNF loading

CNF loading wt.%	Young's Modulus (MPa)
0	0.0693
1	0.0700
3	0.1046
6	0.1086
9	0.1174

The effect of strain rates on Young's modulus of nanocomposites created by the direct method with 1 wt. % CNF loading was investigated with the strain rate varied from 0.00016s^{-1} to 0.16 s^{-1}. As shown in Figure 35, the Young's modulus displayed less than 5% difference. However, a 10% difference appeared when strain rate increased to 0.16 s^{-1}. The Young's modulus of nanocomposites created by the direct method displayed a slight increase as strain rate increased, but it exhibited a strong mechanical robustness when strain rate below 0.016 s^{-1}. The linear elasticity region of the sample was ended at 21% compressive strain regardless of strain rates.

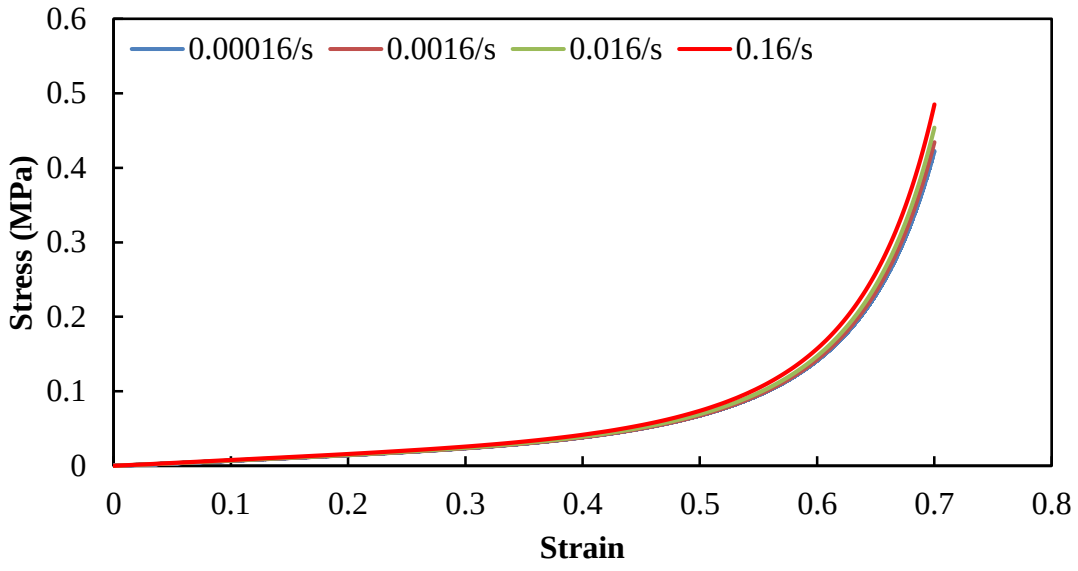


Figure 34. Stress-strain curve of porous nanocomposites created by the direct method (1 wt.% CNF) with various strain rates

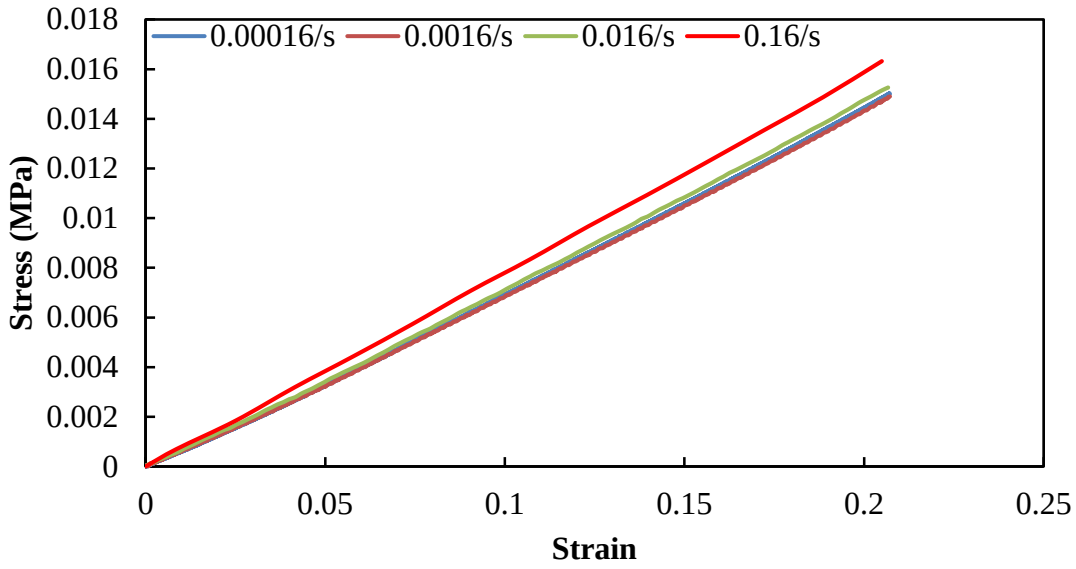


Figure 35. Stress-strain curve of porous nanocomposites created by the direct method (1 wt.% CNF) with various strain rates within linear elasticity region

Table 17. Young's modulus under different strain rates of porous nanocomposites created by the direct method (1 wt.% CNF)

Strain Rate (s^{-1})	Young's Modulus (MPa)
0.00016	0.0706
0.0016	0.0700
0.016	0.0724
0.16	0.0786

4.4.2 Porous Nanocomposites Created by the Indirect Method

Nanocomposites created the by the indirect method with different CNF loading were subjected to the same testing method. As expected, the nanocomposites with the highest CNF loading exhibited the highest stiffness and Young's modulus. As shown in Figure 37, the sample with 0.92 wt. % CNF loading increased Young's modulus from 0.06 MPa to 0.095 MPa. When the sample deformed over the linear elasticity region, the stress of nanocomposites with 0.92 wt.% CNF loading increased rapidly, whereas,

the pristine sample increased slowly. The linear elasticity region of all samples created by the indirect method were ended at 21% compressive strain as well.

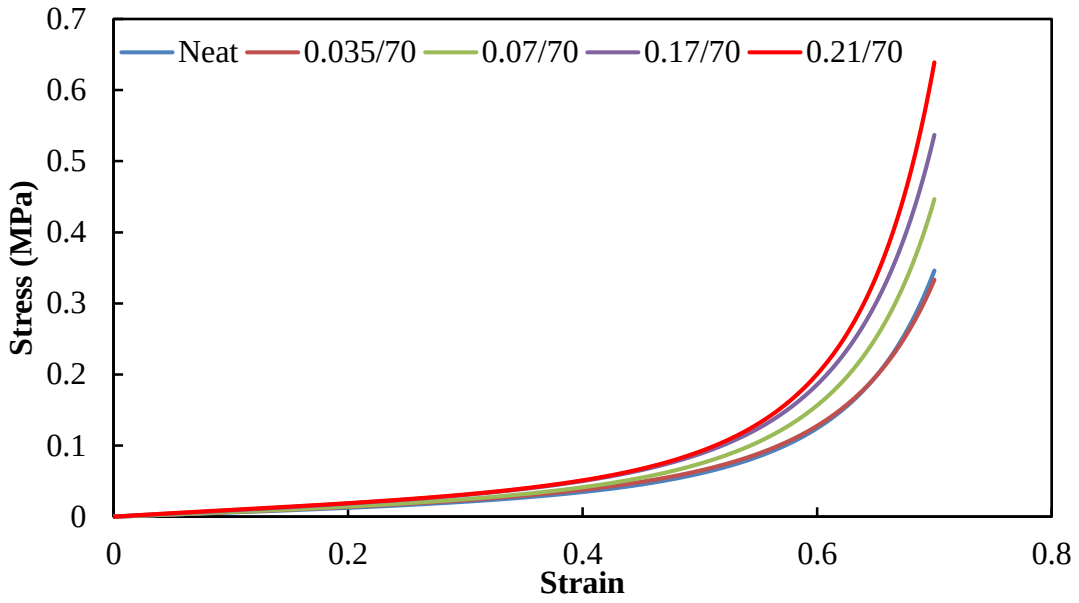


Figure 36. Stress-strain curve of porous nanocomposites created by the indirect method with various amount of CNF loading

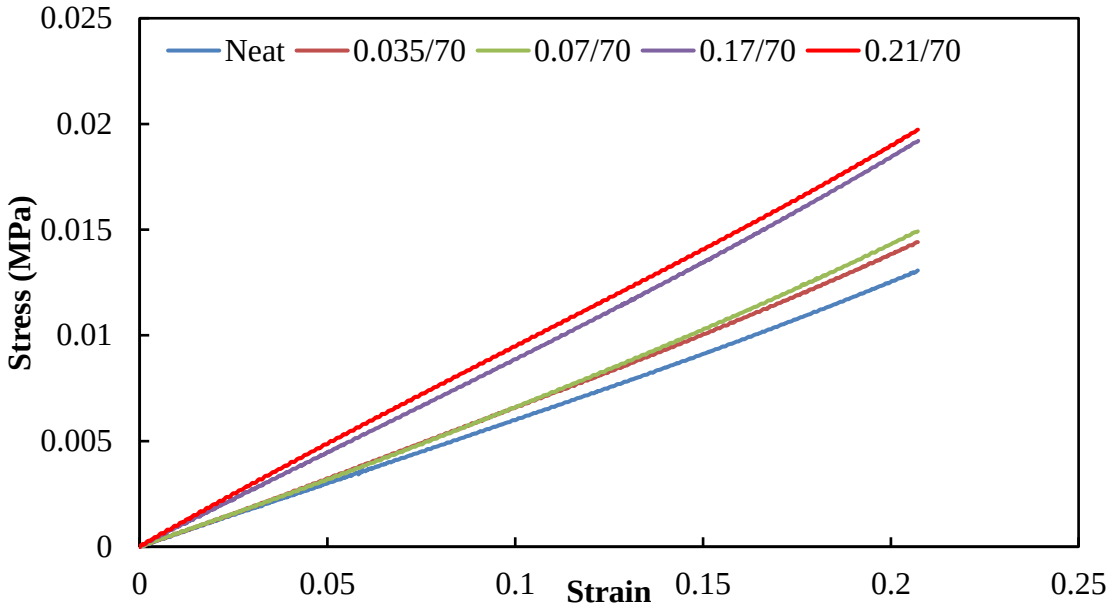


Figure 37. Stress-strain curve of porous nanocomposites created by the indirect method with various amount of CNF loading within linear elasticity region

Table 18. Young's modulus of porous nanocomposites created by the indirect method with various amount of CNF loading

CNF loading wt.%	Young's Modulus (MPa)
0	0.0613
0.24	0.0674
0.47	0.0690
0.78	0.0904
0.92	0.0945

Mechanical robustness of nanocomposites created by the indirect method with 0.92 wt.% CNF loading was validated by the same testing method as direct method. Figure 39 illustrates the Young's modulus and stiffness increased when the strain rate increased from 0.00016s^{-1} to 0.16 s^{-1}. Strong mechanical robustness was validated when the strain rate was below 0.016 s^{-1}.

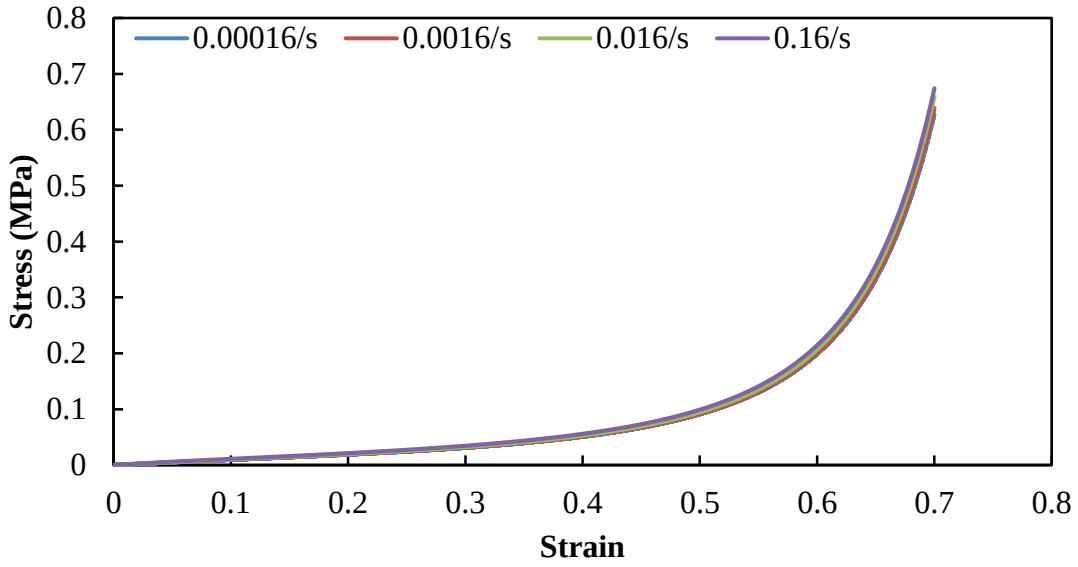


Figure 38. Stress-strain curve of porous nanocomposites created by the indirect method (0.92 wt.% CNF) with various strain rates

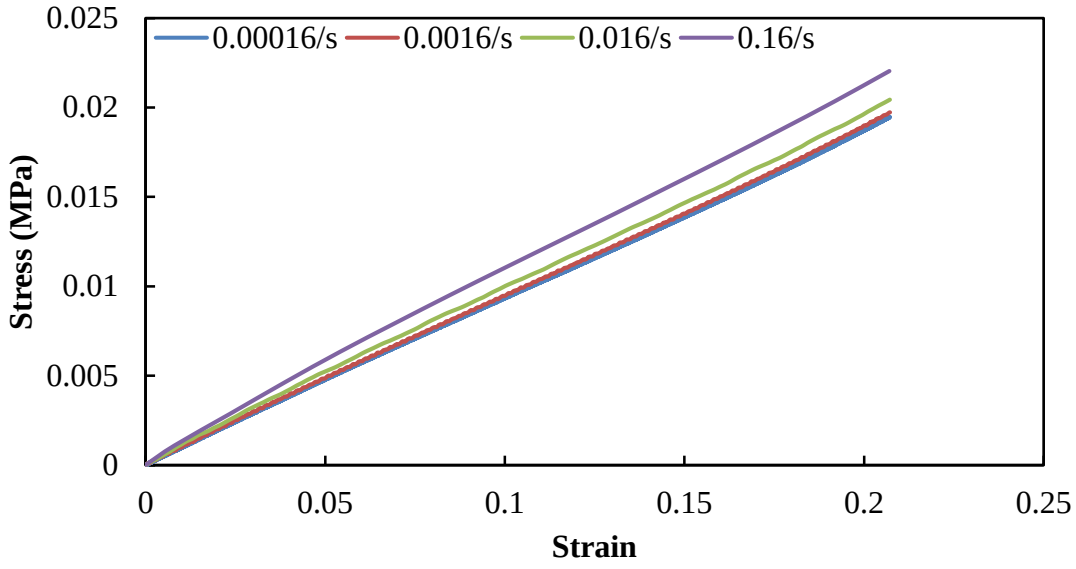


Figure 39. Stress-strain curve of porous nanocomposites created by the indirect method (0.92 wt.% CNF) with various strain rates within linear elasticity region

Table 19. Young's modulus under different strain rates of porous nanocomposites created by the indirect method (0.92 wt.% CNF)

Strain Rate (s^{-1})	Young's Modulus (MPa)
0.00016	0.0931
0.0016	0.0945
0.016	0.0984
0.16	0.1074

It is noted that the critical strain (21% compressive strain) of the linear elasticity region was independent of either CNF loading or strain rate, only dependent on the porosity of the porous PDMS foam. Porous CNF/PDMS nanomaterials created by both methods exhibited strong robustness with strain rates varied over orders of magnitude. Mechanical performances subjected at very high strain rate (0.16 s^{-1}) can be used as a reference for impact sensor, but present work only focuses on conventional scenarios.

4.5 Electrical Properties of Porous CNF/PDMS Nanocomposites Created by the Direct and Indirect Methods

Electrical resistivity is a fundamental property of materials. It describes how strongly oppose the flow of electric current. Electrical conductivity, the reciprocal of electrical resistivity, indicates the capacity of conducting the flow of electric current [48]. These intrinsic properties are indispensable for designing piezoresistive sensors. To understand the effect of the CNF loading in porous CNF/PDMS nanocomposites on electrical properties, the electrical resistance of nanocomposites created by both methods were measured and compared. Additionally, it is necessary to explore the percolation threshold of CNF for outlook and guidance in electrical sensor design.

Due to a low conductive, thin PDMS film on the surface of samples created by the direct method, the two probes method had to be used to measure its electrical resistance. Two needles were inserted on opposite ends of the cube about 8mm apart, as shown in Figure 40. Samples created by the indirect method were sandwiched between two aluminum blocks and a small load was applied until the aluminum blocks fully contacted the surfaces, as show in Figure 41. An Agilent 34401A multimeter connected to an RS-232 data logger at 3 Hz frequency was used to record electrical resistance over a 20 seconds data collection period, as shown in Figure 42 and Figure 43.

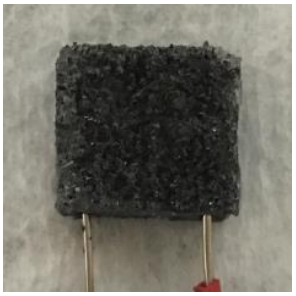


Figure 40. Electrical resistance measurement set up of porous nanocomposites created by the direct method

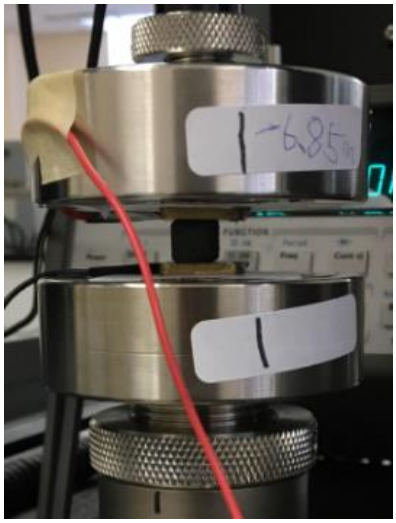


Figure 41. Electrical resistance measurement set up of porous nanocomposites created by the indirect method

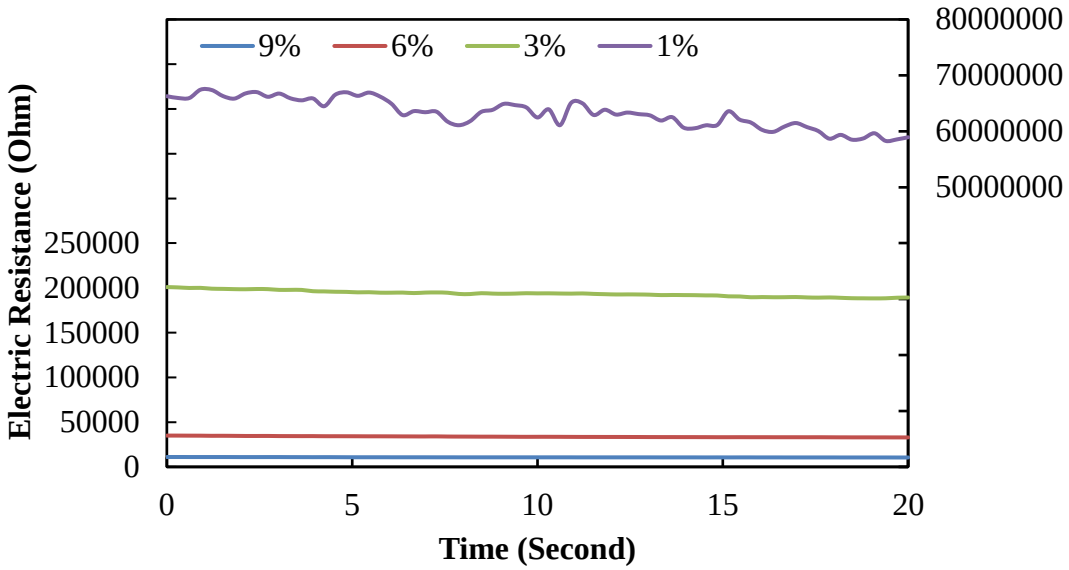


Figure 42. Electrical resistance of porous nanocomposites created by the direct method with various amount of CNF loading

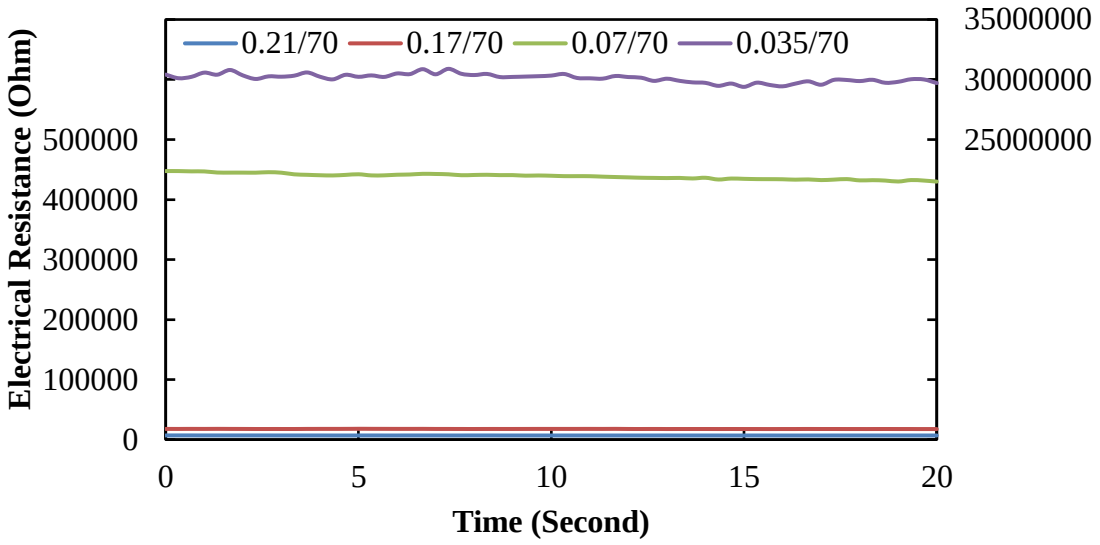


Figure 43. Electrical resistance of porous nanocomposites created by the indirect method with various amount of CNF loading

The electrical resistivity of porous nanocomposites is calculated by:

$$\rho = R\frac{A}{L} \tag{6}$$

where ρ is the electrical resistivity, R is the average electrical resistance, A is the cross-sectional area of the sample, and L is the height of nanocomposites created by the indirect method; or 8mm for nanocomposites created by the direct method.

The electrical conductivity of porous nanocomposites is calculated by

$$\sigma = \frac{1}{\rho} \tag{7}$$

where σ is electrical conductivity.

Table 20. Electrical resistivity and conductivity of porous nanocomposites created by the direct method with various CNF loading

CNF wt.%	Resistivity (Ohm-m)	Conductivity (S/m)
1	7.33E+05	1.36E-06
3	2.23E+03	4.49E-04
6	3.91E+02	2.56E-03
9	1.23E+02	8.12E-03

Table 21. Electrical resistivity and conductivity of porous nanocomposites created by the indirect method with various CNF loading

Concentration (g/L)	CNF wt.%	Resistivity (Ohm-m)	Conductivity (S/m)
0.5	0.24	2.36E+05	4.24E-06
1	0.47	3.56E+03	2.81E-04
2.42	0.78	1.44E+02	6.94E-03
3	0.92	5.53E+01	1.81E-02

The average of electrical resistance was used to calculate conductivity and resistivity. As shown in Table 20 and Table 21, the electrical conductivity enhanced with increasing CNF loading of the nanocomposites created by both methods. The higher amount of CNF deposited into nanocomposites resulted in a larger number of electrical pathways, as depicted from SEM figures, thus enhanced conductivity. It is noted that the conductivity of the nanocomposites created by the direct method increased rapidly when the CNF loading increase from 1 wt.% and 3 wt.%. This increase was over 100 times greater than the CNF loading increased from 3 wt.% to 6 wt.%. For nanocomposites created by the indirect method, conductivity increased sharply from 0.24 wt.% to 0.47 wt.% CNF loading. These results illustrate percolation threshold of porous CNF/PDMS nanocomposites happened at 3 wt. % CNF loading for the direct fabrication method and 0.47 wt. % CNF loading for the indirect fabrication method. As shown in Figure 44 and Figure 45, in order to reach the same resistivity/conductivity of the indirect method fabricated sample at 0.78 wt.% CNF loading, the direct method fabricated sample required 9 wt.% CNF loading. Therefore,

the indirect method requires a relative lower CNF loading to reach the percolation threshold. In another word, porous nanocomposites created by the indirect method could obtain sufficient electrical conductivity with a small quantity of CNF. This is because the indirect method created more electric networks than the direct method when loaded with same amount of CNF, as shown in Table 4 and Table 5. In addition, the formation of CNF chunks in nanocomposites created by the indirect method plays an important role in enhancing conductivity.

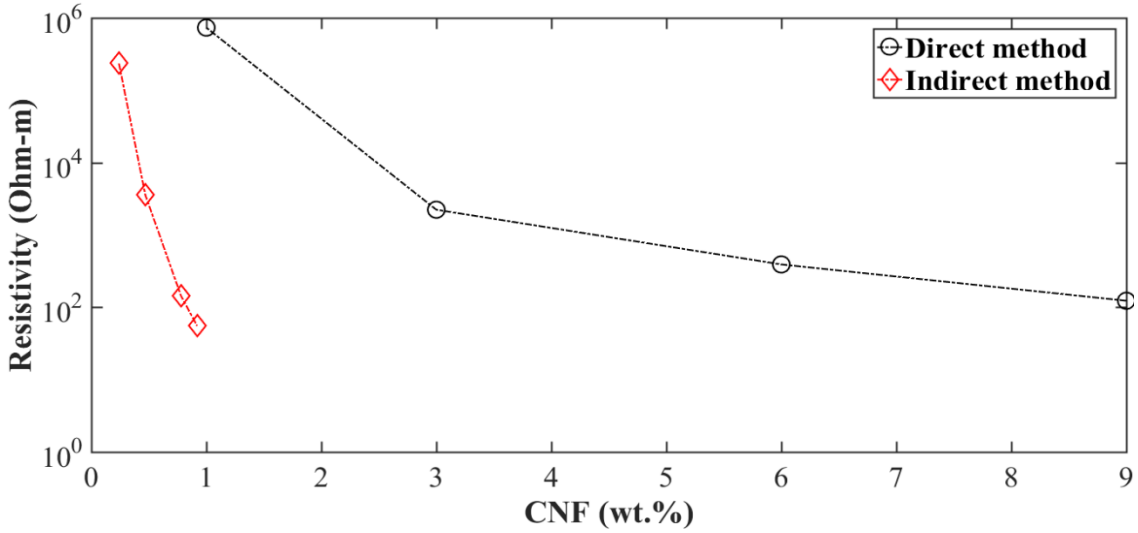


Figure 44. Electrical resistivity of porous nanocomposites created by the direct and indirect methods

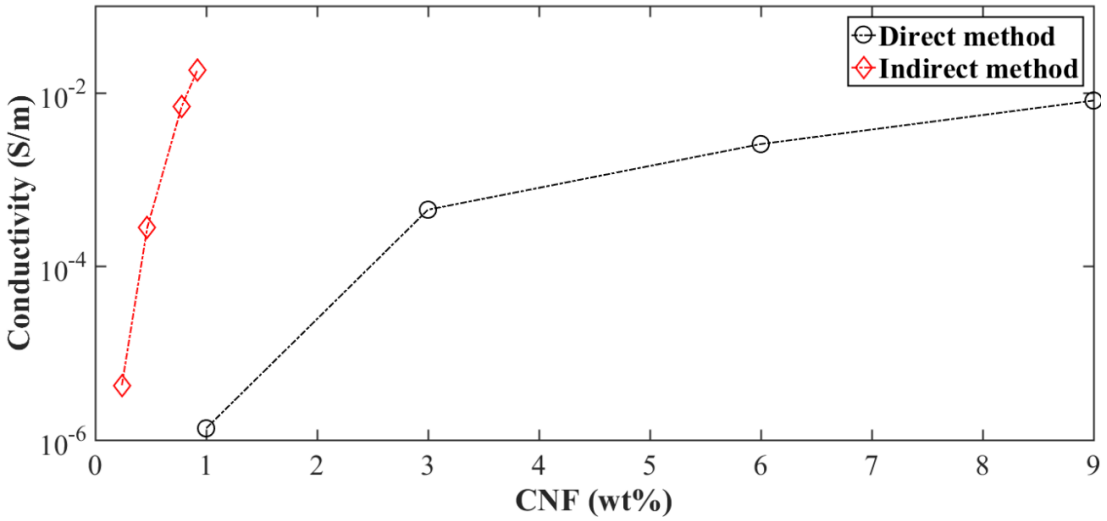


Figure 45. Electrical conductivity of porous nanocomposites created by the direct and indirect methods

Chapter 5. Sensing Concept Validation

Among the piezoresistive, piezoelectric, capacitive, triboelectric, and electromagnetic in the range of conductive based applications, piezoresistive sensors have drawn significant interest over recent decades. The piezoresistive effect is defined as a change in electrical resistivity when strain or stress is applied. The basic principle of piezoresistive pressure or strain sensors is to convert pressure or deformation to an electrical signal [49]. The pressure or deformation on sensors is typically triggered by external stimuli such as pressure, strain, and magnetic field. The piezoresistive sensing functions are characterized by correlating the relative electrical resistance change and the pressure or strain change. Thus, the load exerted on a sensor could be predicted based on the sensing function. The performance of a piezoresistive sensor was considered the most important evaluation criteria. Barlian et al. [50] derived the relative electrical resistance chance relative to strain change equations. The electrical resistance of any homogenous materials is related to its dimension and electrical resistivity as the function of:

$$R = \rho \frac{L}{A} \tag{8}$$

where ρ is electrical resistivity, R is electrical resistance, A is cross-sectional area, and L is height of sample.

The cross-sectional area changes as the function of the longitudinal strain by Poisson's ratio *v*. Thus, the relative electrical resistance change is due to both geometric effect (1+2 *v*) with strain and change in electrical resistivity ($\frac{\Delta\rho}{\rho}$), as the following function [51]:

$$\frac{\Delta R}{R} = (1 + 2v)\varepsilon + \frac{\Delta \rho}{\rho} \quad (9)$$

where, ΔR is the electrical resistance change from initial resistance, R is original electrical resistance, and ε is the applied strain on the sample.

The Gauge factor is defined as the ratio of the relative electrical resistance change to strain. It is a familiar way to describe the piezoresistive property of a sensor. Higher gauge factor indicates a high sensitivity at specific strain region and vice versa. The Gauge factor is calculated by equation:

$$\text{Gauge factor} = \frac{\frac{\Delta R}{R}}{\varepsilon} \quad (10)$$

The relative electrical resistance change of metal sensor most from the geometric effect while a negligible change in electrical resistivity. The gauge factors are approximately from 1.4 to 2.0. Nevertheless, for silicon-based semiconductor, change in electrical resistivity is much larger than metal resulting in a larger gauge factor. To pursue the promising performances of sensing applications, the preliminary sensing responses are essential to validate. Recently, researchers have reported numerous testing methods such as, tensile, compressive, and stretching tests under single or cyclic loading/unloading tests [8] to validate the feasibility of sensors.

This chapter discusses the sensing responses of porous nanocomposites created by both methods under cyclic compressive test and their piezoresistive mechanism. Moreover, the durability and robustness of selected samples are demonstrated by applying strain rates varied over orders of magnitude and performing a long-term performance, respectively.

5.1 Sensing Functions of Porous CNF/PDMS Nanocomposites Created by the Direct Method

The porous CNF/PDMS nanocomposites created by the direct method were placed between two copper plates attached to two flat plates. These plates are a fixture attachment on an Instron 5900 column testing machine, as shown in Figure 46. A 0.1 N initial force was applied to avoid slippage and to ensure full contact of sample on top and bottom surfaces at the beginning of the test. The crosshead speed was 1mm/min. The force, deformation, and electrical resistance were recorded continuously by the Instron machine and data logger.

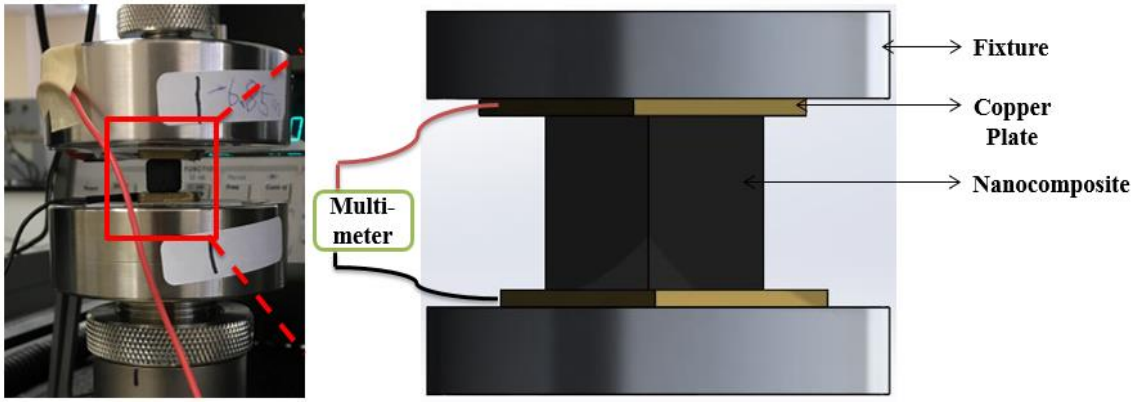


Figure 46. Schematic setup for sensing functions validation in compressive loading and unloading test

There are two piezoresistive mechanisms probably operating within the porous CNF/PDMS nanocomposites: the matrix effect and pore effect. As shown in Figure 47, the matrix effect is the change in resistance due to the rearranging of CNF (black ellipse) embedded within the cured PDMS matrix (blue frame). When the sample is being compressed under a lower strain range, the CNFs are brought closer together within matrix or contact CNF that attaches to the pore walls, creating electrical pathways. At a higher strain range, most networks have been created, the resistance begins to reach a threshold. This threshold can manifest itself in overlapping CNF.

Degradation of pathways begins because CNF cannot comply with the deformation of the PDMS frame.

The pore effect is the change in resistance due to the creation of conductive networks as a result of the rearrangement of CNF that attaches to the pore walls. As a compressive strain is induced on a sample, the CNF on the pore walls is being brought closer together with matrix deformation. The pores continuously collapse creating more electric networks until all pores have collapsed. It causes the formations of multi-branched networks due to the CNF sliding.

In conductive porous nanocomposites, both effects can be seen, but one may dominate over the other depending on the amount of CNF embedded within the matrix and attached to the pores.

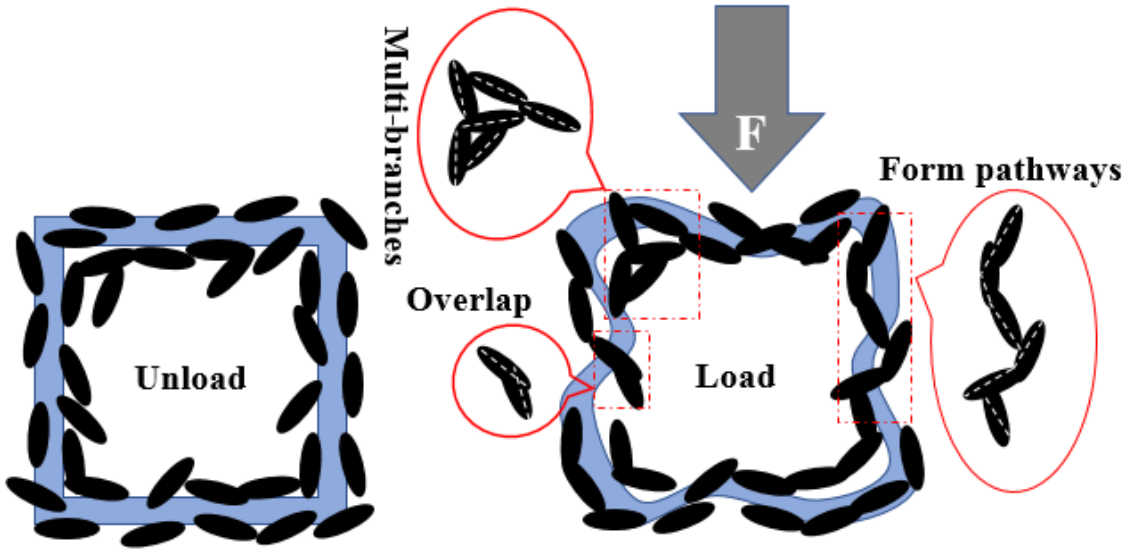


Figure 47. Effect of compressive deformation on the electrical networks of the porous CNF/PDMS nanocomposites

The sensing functions of porous CNF/PDMS nanocomposites created by the direct method (3 wt.%, 6 wt.%, and 9 wt.% CNF) were characterized under cyclic compressive loading and unloading tests. The tests were performed at 1.25%, 2.5%, 5%,

10%, 20%, and 40% maximum compressive strains. Figure 48, Figure 49, and Figure 50 illustrate the relationship between the relative electrical resistance change and maximum compressive strain during five cycles of the test for three CNF loadings. As expected, the relative resistance change increased with larger compressive strain. When the sample was deformed, the CNF (embedded or attached to the pore walls) became closer and may have contacted. The numbers of conductional networks increased, causing a decreased electrical resistance. When sample was released, the CNF returned to their original location, reversing the CNF networks created, and creating an increased electrical resistance.

The gauge factors for CNF/PDMS nanocomposites created by the direct method under different maximum compressive strains were calculated by Equation 10, as shown in Table 22, Table 23, and Table 24. The gauge factors decreased when compressive strain increased up to 20%. The gauge factors, then rose slightly at 40% maximum strain. Except at 9 wt.% CNF loading sample, the gauge factor decreased up to 10% maximum strain, and slightly increased at 20%. The sample with a higher CNF loading exhibited a larger gauge factor at 40% maximum compressive strain. Nevertheless, 3 wt. % CNF loading sample exhibited a largest gauge factor up to 20% maximum compressive strain range

This phenomenon happened because the CNF was very spread out and embedded within the PDMS matrix for nanocomposites created by the direct method, as depicted in SEM figure, meaning that the dominating piezoresistive effect is the matrix effect. The sample with a lower CNF loading exhibited a higher potential for electric network creation. Because a larger spacing between the CNF, but as the CNF loading

increases, the larger amount of CNF results in less spacing. This results in a lower potential for new electric network formation as the sample being compressed or with a higher CNF loading, because network formation will reach saturation earlier. This effect is true for CNF that embedded within the PDMS matrix because they cannot escape. Thus, the gauge factor is larger in a lower compressive strain or with a lower CNF loading. Wu. et al. [8] similarly reported that porous CNF/PDMS nanocomposites with lower CNF loading exhibited a higher sensitivity than those with a higher CNF loading.

Once saturation of electrical networks is achieved within the PDMS matrix, the electrical resistance change is dominated by the creation of networks of CNF attached to the pore walls, or the pore effect. The formation of multi-conduction pathways perturbs the rule that less CNF loading provides a high potential sensing capacity, because multi-branched pathways enhance electrical conductivity strongly [23]. As the deformation increases, and the pores begin to collapse, the CNF on the pore walls are continuously being brought closer together, and thus, the higher loading of CNF results in more CNF on the pore walls which allows for a larger number of multi-branched pathways to be created. Therefore, the nanocomposites created by the direct method with a higher CNF loading exhibited a larger gauge factor of when the compressive strain was over 20%.

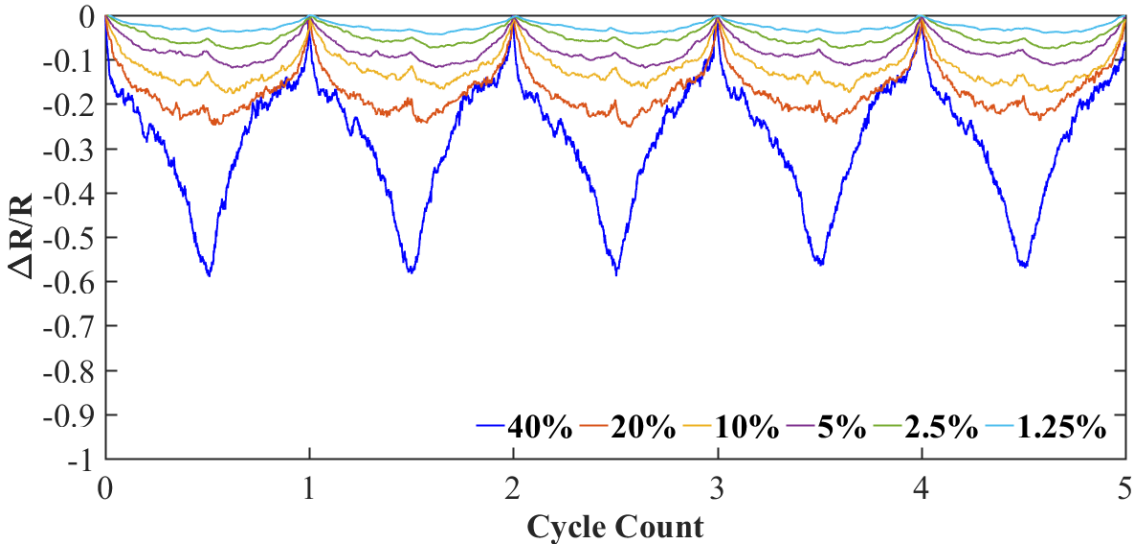


Figure 48. Sensing functions of porous nanocomposites created by the direct method (3 wt.% CNF) under different maximum compressive strain

Table 22. Gauge factors of porous nanocomposites created by the direct method (3 wt.% CNF) under different maximum compressive strain

Strain	Resistance change	Gauge factor
1.25%	4.1%	3.28
2.5%	7.4%	2.96
5%	11.8%	2.36
10%	16.5%	1.65
20%	25.3%	1.27
40%	58.9%	1.47

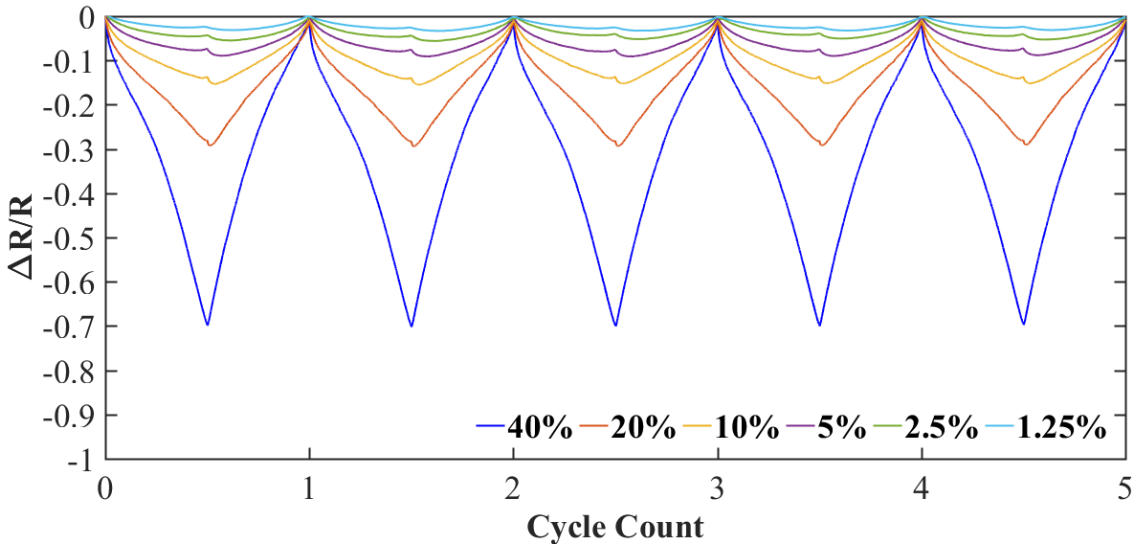


Figure 49. Sensing functions of porous nanocomposites created by the direct method (6 wt.% CNF) under different maximum compressive strain

Table 23. Gauge factors of porous nanocomposites created by the direct method (6 wt.% CNF) under different maximum compressive strain

Strain	Resistance change	Gauge factor
1.25%	3.3%	2.64
2.5%	5.2%	2.08
5%	9.1%	1.82
10%	15.2%	1.52
20%	29.2%	1.46
40%	70.1%	1.75

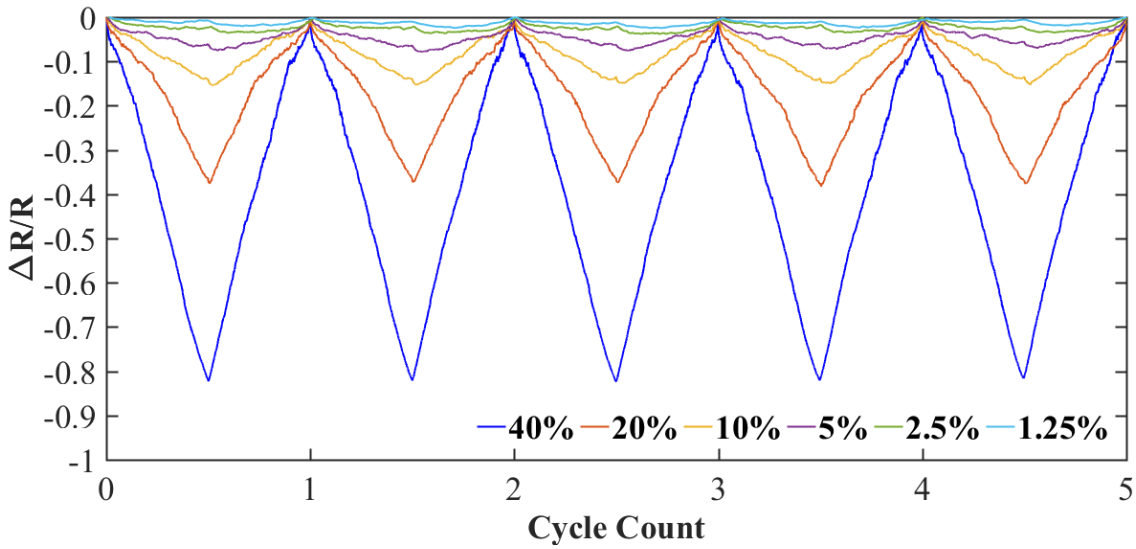


Figure 50. Sensing functions of porous nanocomposites created by the direct method (9 wt.% CNF) under different maximum compressive strain

Table 24. Gauge factors of porous nanocomposites created by the direct method (9 wt.% CNF) under different maximum compressive strain

Strain	Resistance change	Gauge factor
1.25%	2.3%	1.84
2.5%	3.8%	1.52
5%	7.6%	1.52
10%	14.9%	1.49
20%	37.4%	1.87
40%	82.3%	2.06

Figure 51, Figure 52, and Figure 53 show the relative resistance change and stress as a function of strain, in this way, the induced stress and strain could be identified by the relative resistance change (applications for stress/strain sensor). The 6 wt.% and 9 wt.% CNF loading samples exhibited excellent sensing response because

the relative resistance change changed consistently with nearly linear sensing responses regardless of the CNF loading and strain range. But, the 3 wt. % CNF loading sample presented an unstable sensing response with several sudden fluctuates. Thus, the 6 wt.% and 9 wt.% CNF loading samples could be potentially developed as stress/strain sensors. The gauge factors at the 40% maximum compressive strain were 1.47, 1.75, and 2.06, respectively, for 3 wt.%, 6 wt.%, and 9 wt.% CNF loading samples .

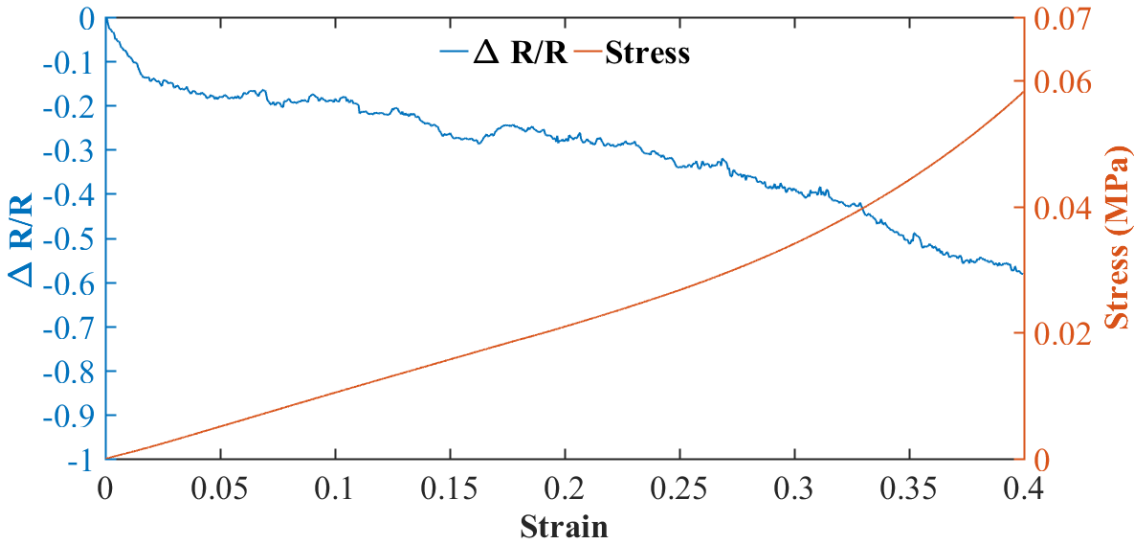


Figure 51. Validation of relative resistance change and stress as a function of strain porous nanocomposites (3 wt.% CNF) created by the direct method

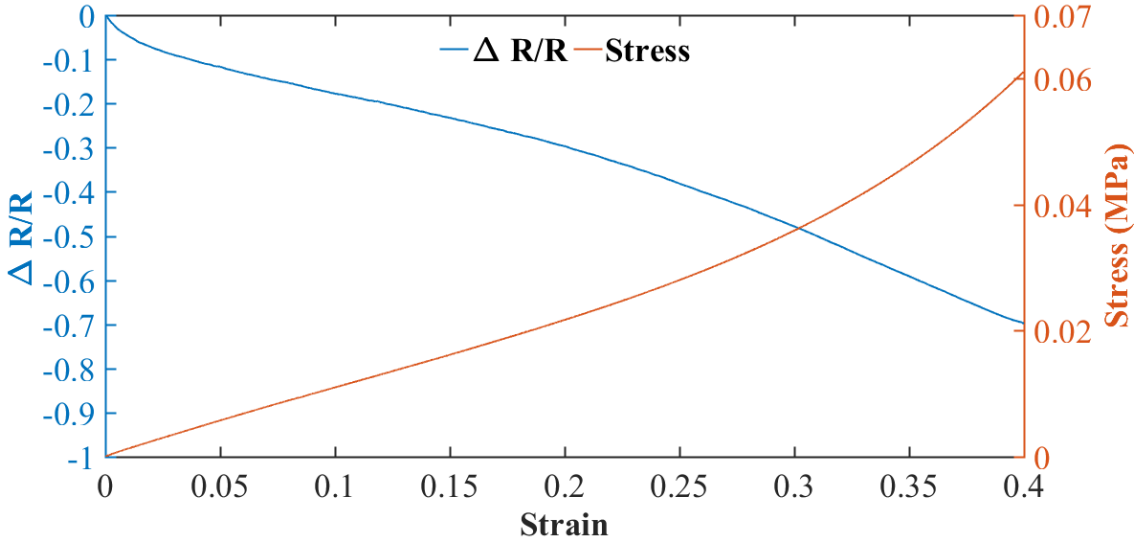


Figure 52. Validation of relative resistance change and stress as a function of strain porous nanocomposites (6 wt.% CNF) created by the direct method

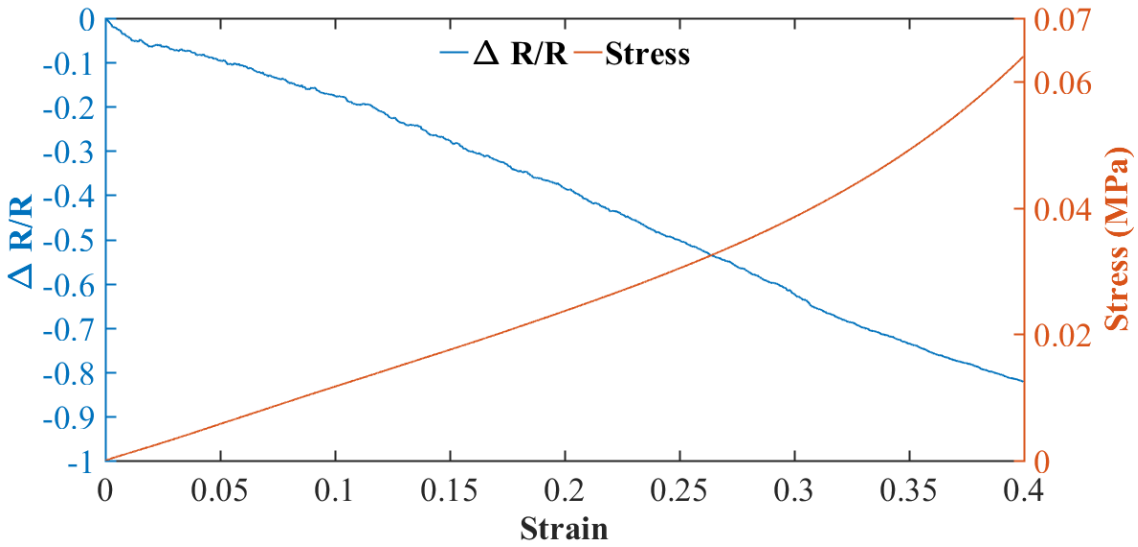


Figure 53. Validation of relative resistance change and stress as a function of strain porous nanocomposites (9 wt.% CNF) created by the direct method

5.2 Sensing Functions of Porous CNF/PDMS Nanocomposites Created by the Indirect Method

The sensing functions of porous CNF/PDMS nanocomposites created by the indirect method were characterized in the same testing method. Figure 54, Figure 55, and Figure 56 illustrate the sensing functions within five cycles of the test for three CNF loadings. Similarly, the resistance of samples decreased when induced a larger compressive deformation.

The gauge factors were always larger at lower compressive strain for each type of nanocomposites, as shown in Table 25, Table 26, and Table 27. In addition, the gauge factors increased with a higher CNF loading regardless of compressive strain range, comparing to the samples at different CNF loading under the same compressive strain. This contrasts the nanocomposites created by the direct method. This is due to the piezoresistive mechanism of nanocomposites created by the indirect method only being dominated by the pore effect. Because less CNF was embedded within the cured PDMS matrix, while, the majority of CNF was loosely attached to the pore walls, as

depicted in SEM figures. This displayed as a constant increase of gauge factor at a higher CNF loading for the same strain because sample with a higher CNF loading were likely to create multi-branched networks. The sample with 0.92 wt.% CNF loading presented the largest sensitivity for all cyclic tests when compared to samples with 0.47 wt.% and 0.78 wt.% CNF loading.

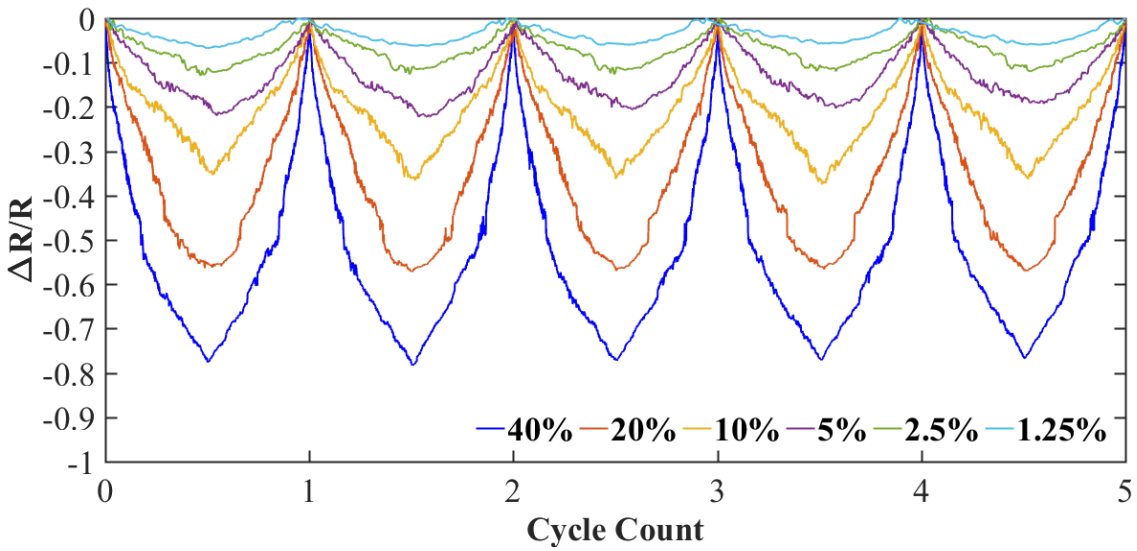


Figure 54. Sensing functions of porous nanocomposites created by the indirect method (0.47 wt.% CNF) under different maximum compressive strain

Table 25. Gauge factors of porous nanocomposites created by the indirect method (0.47 wt.% CNF) under different maximum compressive strain

Strain	Resistance change	Gauge factor
1.25%	6.0%	4.80
2.5%	12.3%	4.92
5.0%	20.5%	4.10
10.0%	36.3%	3.63
20.0%	56.5%	2.83
40.0%	77.2%	1.93

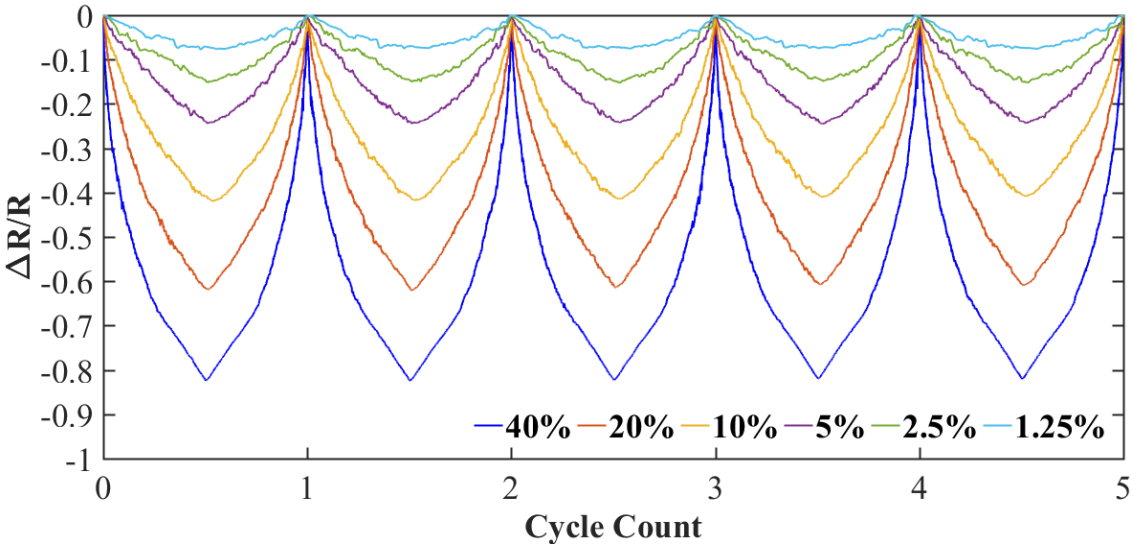


Figure 55. Sensing functions of porous nanocomposites created by the indirect method (0.78 wt.% CNF) under different maximum compressive strain

Table 26. Gauge factors of porous nanocomposites created by the indirect method (0.78 wt.% CNF) under different maximum compressive strain

Strain	Resistance change	Gauge factor
1.25%	7.6%	6.08
2.5%	15.3%	6.12
5.0%	24.3%	4.86
10.0%	41.5%	4.15
20.0%	61.4%	3.07
40.0%	82.0%	2.05

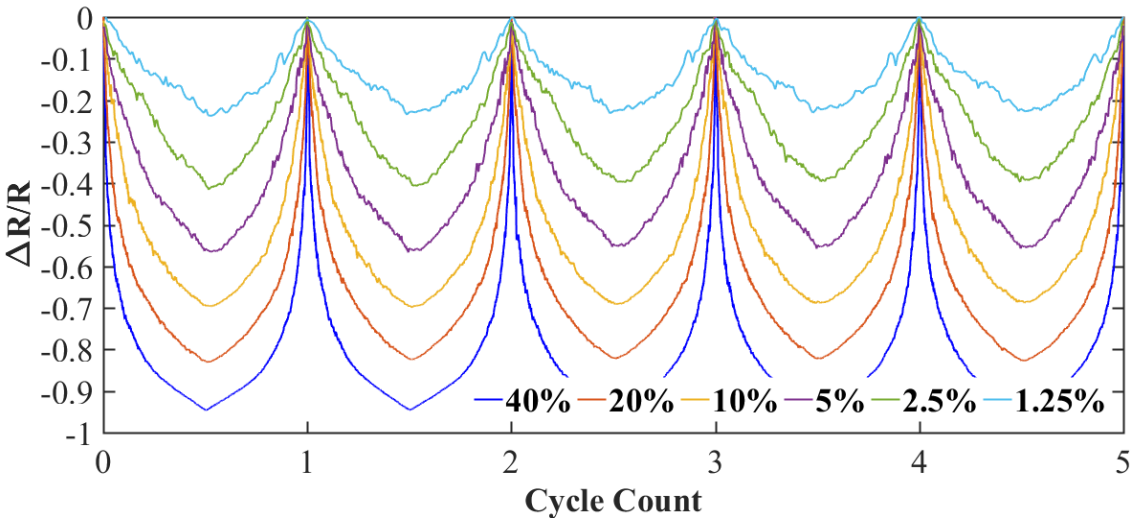


Figure 56. Sensing functions of porous nanocomposites created by the indirect method (0.92 wt.% CNF) under different maximum compressive strain

Table 27. Gauge factors of porous nanocomposites created by the indirect method (0.92 wt.% CNF) under different maximum compressive strain

Strain	Resistance change	Gauge factor
1.25%	23.2%	18.56
2.5%	39.7%	15.88
5.0%	55.3%	11.06
10.0%	68.8%	6.88
20.0%	82.1%	4.11
40.0%	94.2%	2.36

Figure 57, Figure 58, and Figure 59 show the relative resistance change changed consistently for the 0.78 wt.% and 0.92 wt.% CNF loading samples. The 0.47 wt.% CNF loading sample displayed a near linear sensing response, while, the 0.92 wt.% CNF loading sample displayed the most non-linear sensing response due to denser CNF distributed on PDMS plane and CNF chunks appeared inside of pores, as shown in Table 5, which diminished the degree of linearity in the sensing function. The CNF distribution also explained the reason of nanocomposites created by the direct method displayed linear sensing functions, because a relative less CNF distributed on the PDMS plane, compared with nanocomposites created by the indirect method with 0.78 wt.% and 0.92 wt.% CNF loading. The gauge factor at the 40% maximum compressive strain was 1.93, 2.05, and 2.36 for the nanocomposites with 0.47 wt.%, 0.78 wt.%, and 0.92 wt.% CNF loading, respectively. The nanocomposites created by the indirect method displayed a tremendous sensitivity especially at the lower compressive strain range. However, it yielded non-linear sensing responses and the degree of linearity depended on the CNF loading.

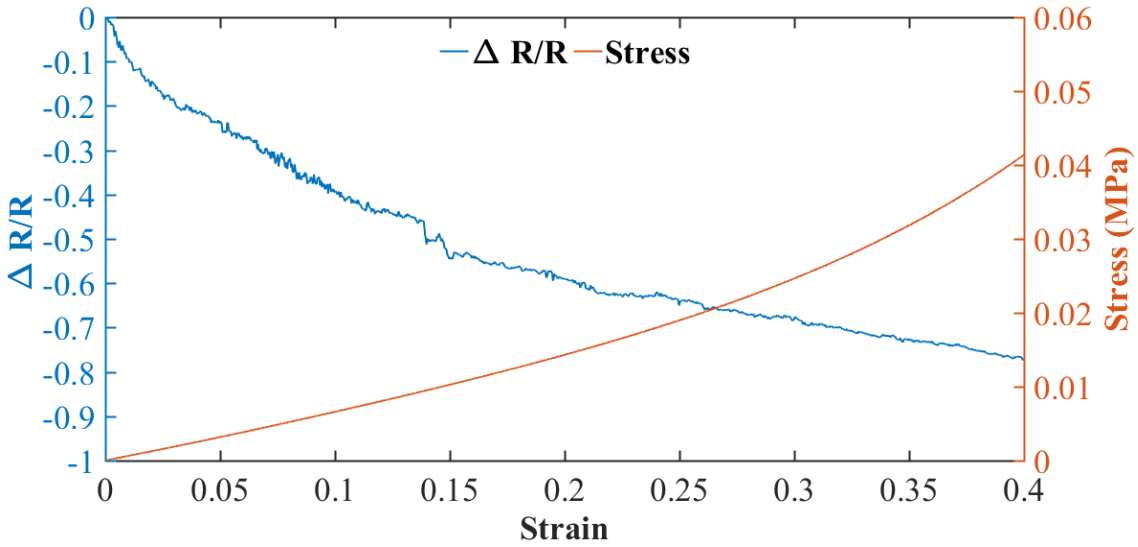


Figure 57. Validation of relative resistance change and stress as a function of strain porous nanocomposites (0.47 wt.% CNF) created by the indirect method

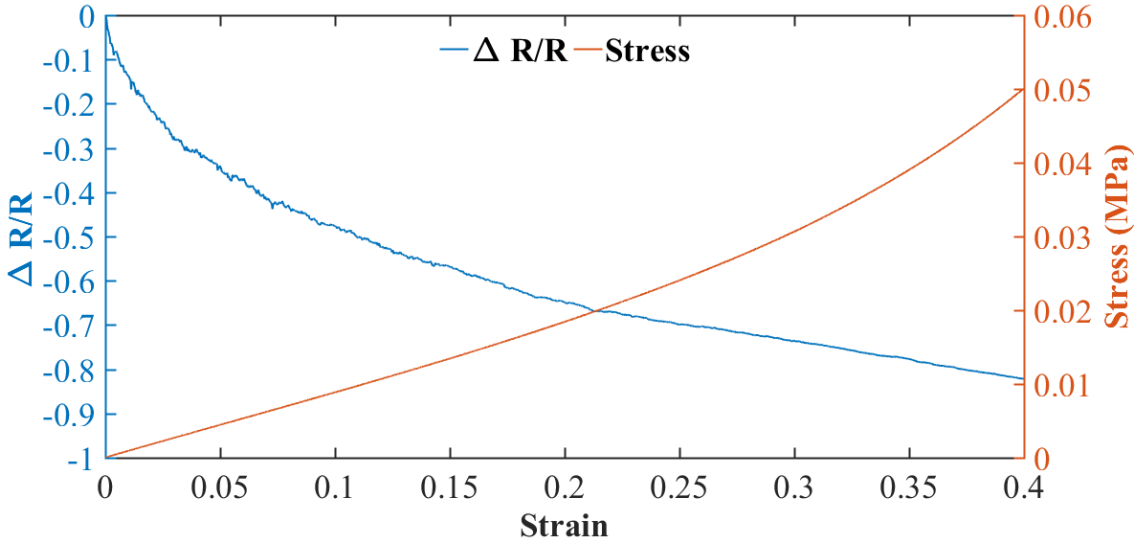


Figure 58. Validation of relative resistance change and stress as a function of strain of porous nanocomposites (0.78 wt.% CNF) created by the indirect method

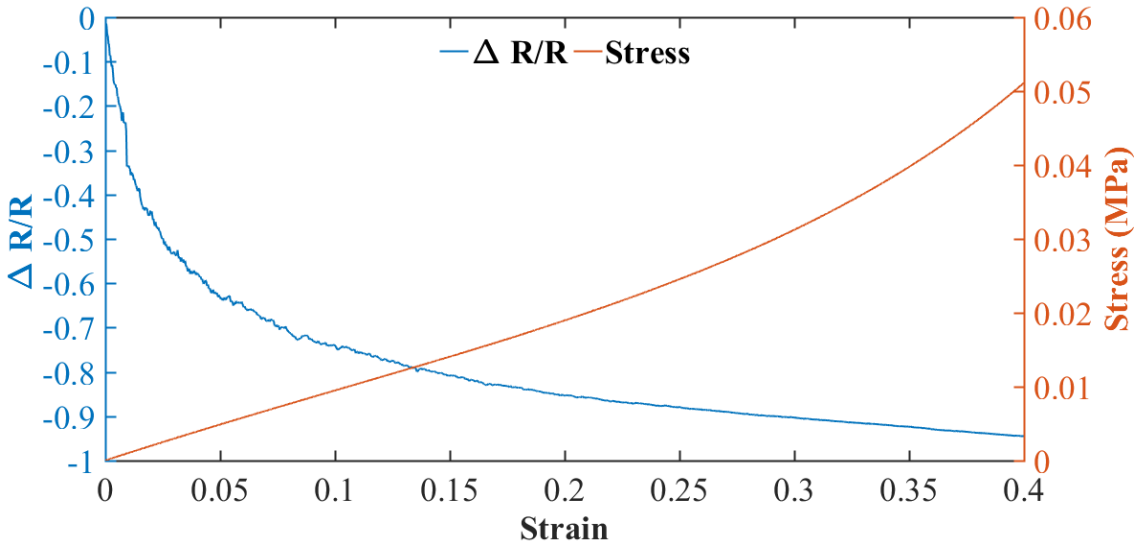


Figure 59. Validation of relative resistance change and stress as a function of strain of porous nanocomposites (0.92 wt.% CNF) created by the indirect method

5.3 Robustness and Durability of Sensing Responses

Considering the sensing performances of all samples studied above, the nanocomposites created by the direct method with 9 wt.% CNF loading, and the nanocomposites created by the indirect method with 0.78 wt.% CNF loading were selected for optimum formulas. The selection criteria for these two samples hinged on three aspects: the degree of linearity in the sensing function, sensitivity (gauge factor), and quality (none noisy points) of the sensing response. Table 28 illustrates the selection criteria and the ranking of each sample based on each criterion. The sample with the lowest score out of each fabrication method was selected. The nanocomposites created by the direct method with 9 wt.% CNF loading displayed the best degree of linearity and quality, and the nanocomposites created by the indirect method with 0.78 wt.% CNF loading exhibited the best quality and intermediate degree of linearity and sensitivity between samples fabricated using the same method.

Table 28. Selections of optimized porous nanocomposites created by the direct and indirect methods

	Linearity	Sensitivity	Quality	Total
Direct 3 wt.%	3	1	3	7
Direct 6 wt.%	3	2	1	6
Direct 9 wt.%	1	3	1	5
In-direct 0.47 wt.%	1	3	3	7
In-direct 0.78 wt.%	2	2	1	5
In-direct 0.92 wt.%	3	1	2	6

Designing commercial grade sensor requires outstanding robustness and durability of the sensing response. Several criteria must be taken into consideration: (I) to verify robustness of the sensing response, it is expected to experience consistent performances over a wide range of strain rates. (II) to verify durability of the sensing response, sensors must exhibit repeatable performances with full recovery in each cycle, throughout a longevity test.

5.3.1 Robustness Validation

To satisfy criterion (I), cyclic compressive loading and unloading tests were performed at 20% maximum compressive strain with strain rates varied from $0.001s^{-1}$ to $0.06\ s^{-1}$ for the sensor created by the direct method. Figure 60 shows a superposition of five cycles from each of the tests varying strain rates. The relative resistance changed only about 3% between at the lowest and highest strain rate. The sensor created by the indirect method underwent a similar test with varying strain rate from $0.0008\ s^{-1}$ to $0.048\ s^{-1}$. Figure 61 shows the relative resistance changed 5% between at the lowest and highest strain rate. This slightly higher change is likely due to the weak interfacial adhesion of the CNF to the PDMS. This weak adhesion caused problems at high strain rates because the CNF would not comply with the deformation of the porous PDMS frame. This cause the CNF to detach from the porous PDMS matrix, delaying the

recovery of the sensing responses. Nonetheless, they both displayed excellent repeatability at strain rates varied orders of magnitude.

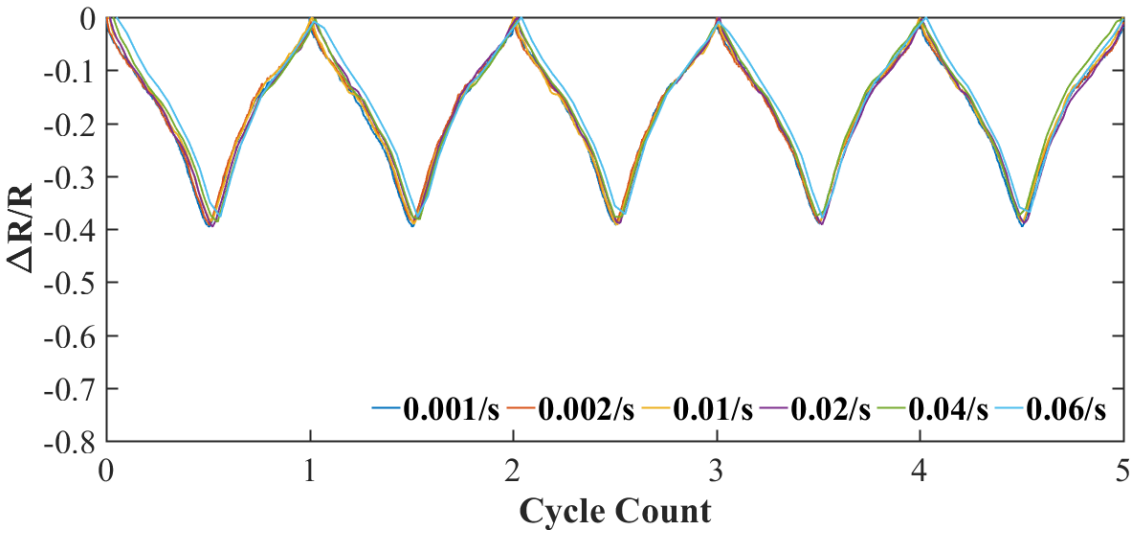


Figure 60. Robustness validation of porous nanocomposites (9 wt.% CNF) created by the direct method

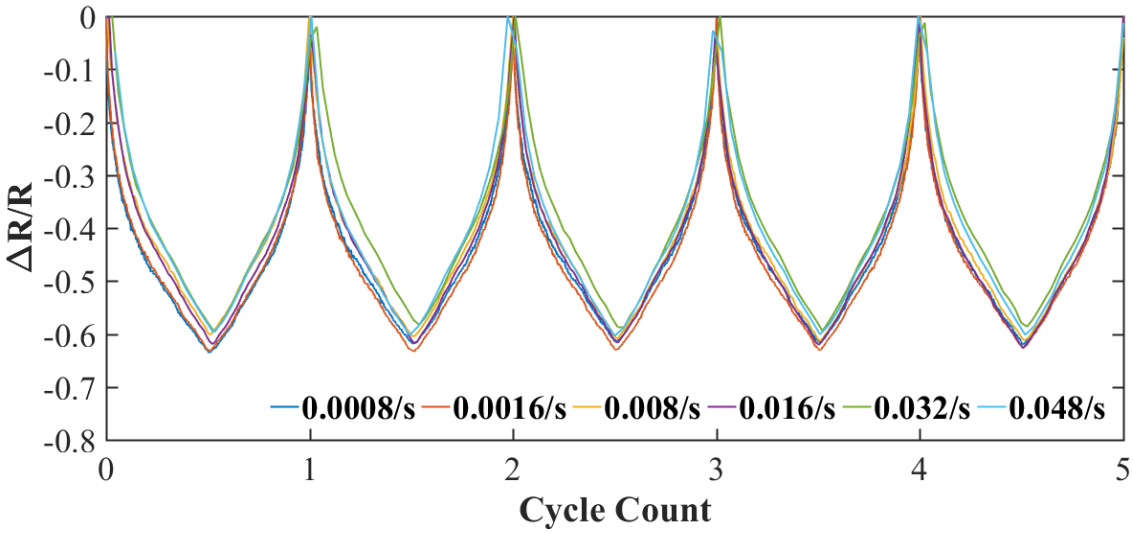


Figure 61. Robustness validation of porous nanocomposites (0.78 wt.% CNF) created by the indirect method

5.3.2 Durability Validation

To satisfy with criterion (II), a long-term cyclic compressive loading and unloading test was performed on the selected samples, holding the 20% maximum compressive strain and crosshead speed constant at 1mm/min for over 12 hours. The results for the durability test of the sample created by the direct method are shown in

Figure 62 and Figure 63. They show the relative resistance change stayed relatively constant, at around 32%, and produced a repeatable sensing response for 240 cycles, with only less than 1% difference.

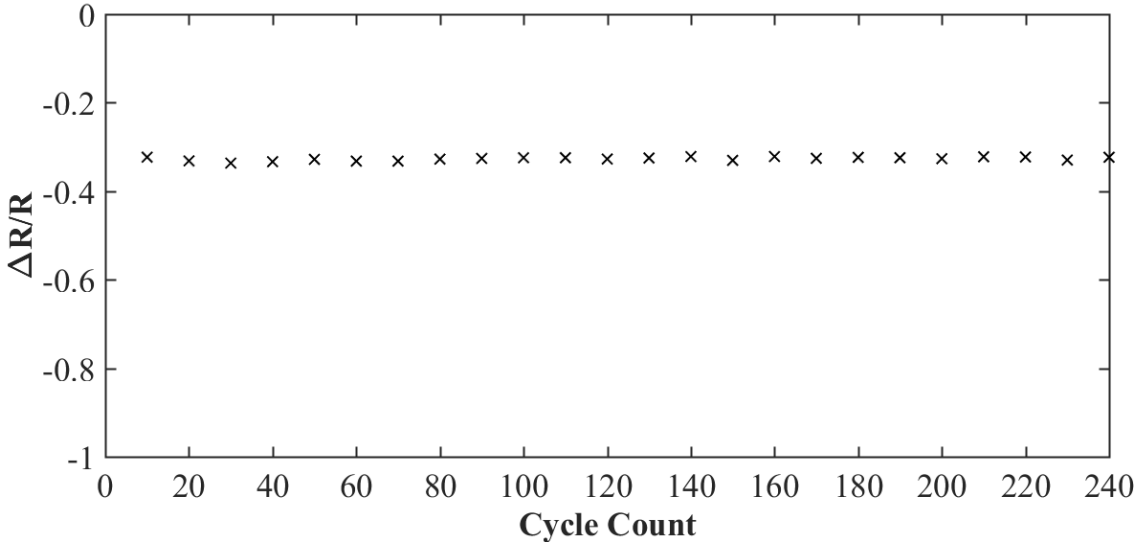


Figure 62. Relative resistance change throughout durability test of porous nanocomposites (9 wt.% CNF) created by the direct method

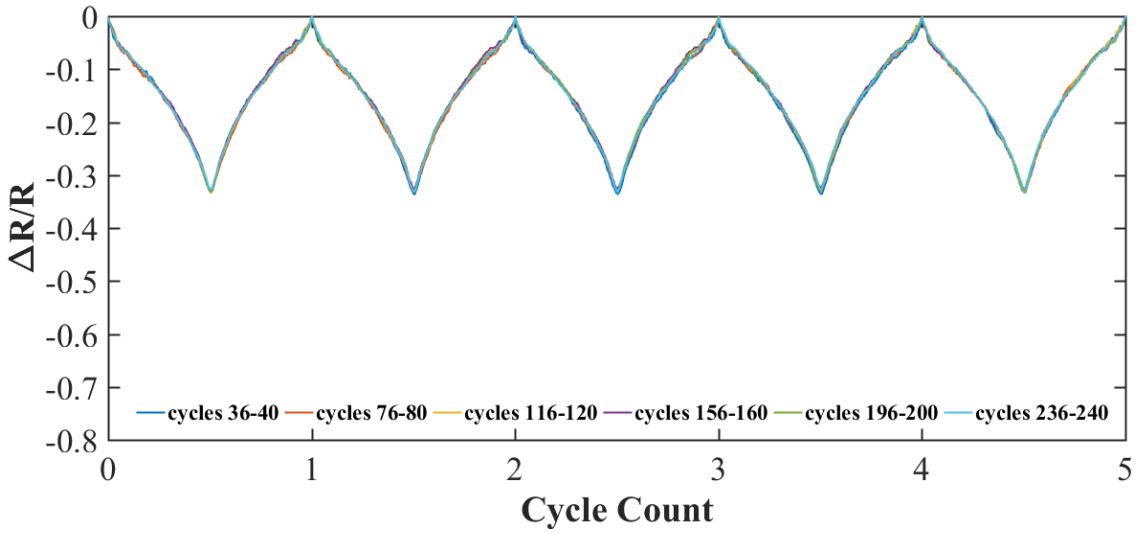


Figure 63. Durability validation of porous nanocomposites (9 wt.% CNF) created by the direct method

Figure 64 and Figure 65 show the results for the same test on the selected sample created by the indirect method. They show the sensor exhibited a constant 60% relative resistance change and less than 1% difference throughout the 180 cycles.

Both of selected porous CNF/PDMS nanocomposites created by the direct and indirect methods displayed consistent, steady, and fully recoverable sensing responses under longevity test.

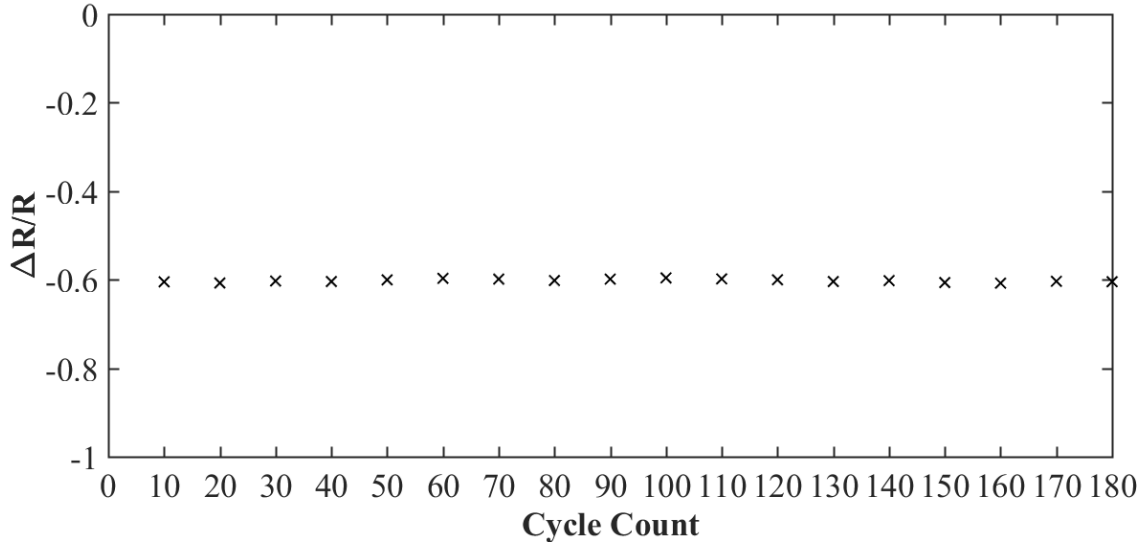


Figure 64. Relative resistance change throughout durability test of porous nanocomposites (0.78 wt.% CNF) created by the indirect method

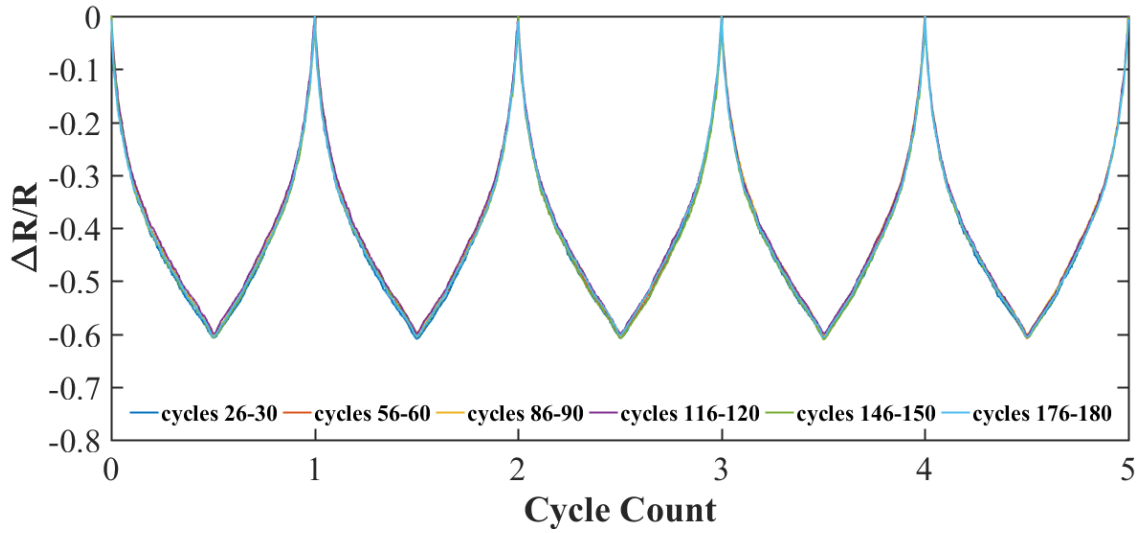


Figure 65. Durability validation of porous nanocomposites (0.78 wt.% CNF) created by the indirect method

The presence of hysteresis may explain the slight change (1%) in sensing responses. It is defined as the area between the loading and unloading curves (hysteresis

loop) [52]. Figure 66 shows the stress of the nanocomposites created by the indirect method with 0.78 wt.% CNF loading lags before return to its original position when compressive load release. This is due to the viscoelastic properties of the porous materials, which absorb energy during loading faster than it releases [53].

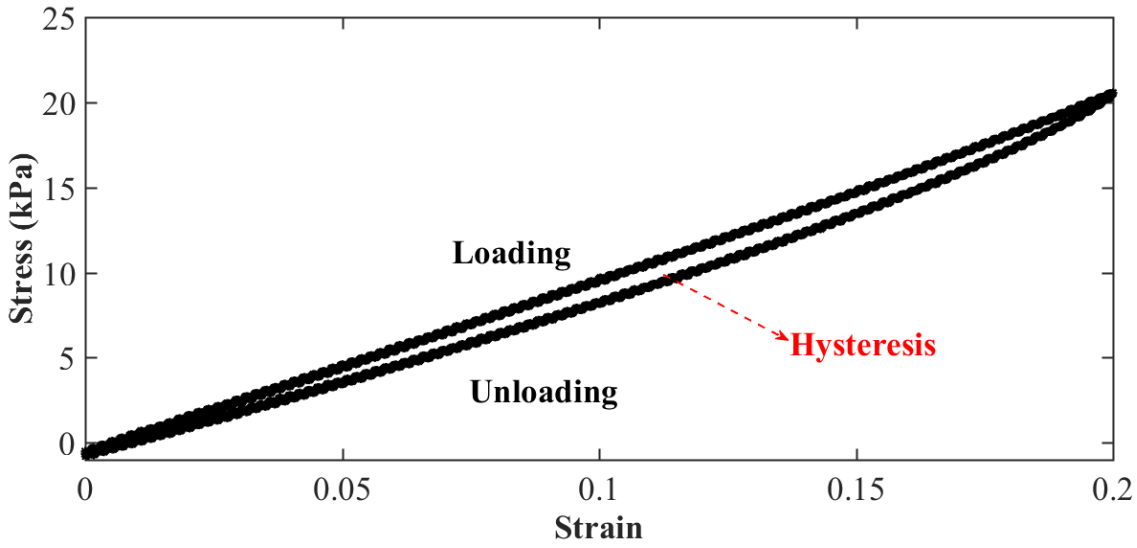


Figure 66. Hysteresis of porous nanocomposites (0.78 wt.% CNF) created by the indirect method

Chapter 6. Summary and Scope for Future Works

This experimental work developed the highly flexible and electrically conductive porous CNF/PDMS nanocomposites for sensing application using the sugar templating strategy. The pristine PDMS foams with four different porosities (77.38%, 75.14%, 71.59%, and 68.48%) were fabricated by changing the volume ratios of fine and coarse sugar particles (4:0, 3:1, 1:3, and 0:4) as sugar templates. The Young's modulus and mechanical behaviors of pristine porous PDMS foams were investigated under quasi-static compressive tests. The Young's modulus could be properly predicted by a polynomial equation by known density. The pristine porous PDMS foam created by only fine sugar crystals was selected as the feasible substrate based on the mechanical performance and productivity.

The CNF was deposited into porous PDMS foam by the direct and indirect methods. In the direct method, the sugar particles were first coated with CNF, which ensured a good adhesion between the CNF and the polymer. In the indirect method, the fine sugar crystals were used to fabricate the porous PDMS foam followed with forcing impregnation of CNF via ultrasonic agitation. The electrical properties of samples were measured and revealed that CNF percolation threshold for porous nanocomposites created by the indirect method (0.47 wt.%) is much lower than nanocomposites created by the direct method (3 wt.%). Moreover, the Young's modulus of nanocomposites created by both methods, with various CNF loading, were characterized under quasi-static compressive tests, which indicated that the Young's modulus increased with a higher CNF loading. Prior to design as a sensor, the mechanical robustness of porous CNF/PDMS nanocomposites created by both methods were validated with strain rates

varied over orders of magnitude. The morphologies of samples, and the distributions and dispersion quality of CNF in nanocomposites created by both methods with low and high CNF loading were examined by SEM. The CNF was embedded into the PDMS matrix for the direct method, while, CNF loosely attached to the pore walls and may precipitated as chunks for nanocomposites created by the indirect method. Additionally, nanocomposites created by both methods provided an uniform CNF dispersion within the PDMS matrix.

The sensing functions of nanocomposites created by both methods, with a series of CNF loadings, were characterized by correlating the relative electrical resistance change and the compressive strain under cyclic compressive loading and unloading tests at the compressive strain range from 1.25% to 40%. Nanocomposites created by the direct method endowed excellent linearity of sensing performances regardless of CNF loading and strain range. The indirect method exhibited non-linearity sensing performances and the degree of linearity depended on the CNF loading. However, it presented a tremendous sensitivity especially at lower strain range. Moreover, nanocomposites created by the direct method with 9 wt.% CNF, and by the indirect method with 0.78 wt.% were selected as optimum formulas based on the degree of linearity in the sensing function, gauge factor, and quality of the sensing response. Finally, the durability and robustness of identified nanocomposites were demonstrated by applying strain rates varied over orders of magnitude and long-term test, respectively.

This work only focused on the sensing performances under compressive tests. Future works are suggested to characterize porous CNF/PDMS nanocomposites under

the tensile test to design sensors for monitoring the movement of human fingers. Besides, the dynamic morphologies of CNF when sample induced by compressive load under SEM should be investigated. It could validate the piezoresistive mechanisms of porous electrically conductive sensors. In addition, future research can explore other innovative shapes of sensor or deposit functionalized nanofiller to improve sensitivity of sensor.

References

1. Luo, W., Y. Liu, and M. Saha. *CNT Bucky Paper Enhanced Sandwich Composites for In-Situ Load Sensing*. in *ASME 2017 International Mechanical Engineering Congress and Exposition*. 2017. American Society of Mechanical Engineers.
2. Zamarayeva, A.M., et al., *Flexible and stretchable power sources for wearable electronics.* Science advances, 2017. **3**(6): p. e1602051.
3. Wang, L., T. Ding, and P. Wang, *Thin flexible pressure sensor array based on carbon black/silicone rubber nanocomposite.* IEEE Sensors Journal, 2009. **9**(9): p. 1130-1135.
4. Tanaka, M., et al., *The "Haptic Finger"–a new device for monitoring skin condition.* Skin Research and Technology, 2003. **9**(2): p. 131-136.
5. Yilgör, E. and I. Yilgör, *Silicone containing copolymers: synthesis, properties and applications.* Progress in Polymer Science, 2014. **39**(6): p. 1165-1195.
6. Johnston, I., et al., *Mechanical characterization of bulk Sylgard 184 for microfluidics and microengineering.* Journal of Micromechanics and Microengineering, 2014. **24**(3): p. 035017.
7. Hocheng, H., et al., *Study of novel electrical routing and integrated packaging on bio-compatible flexible substrates.* Microsystem technologies, 2010. **16**(3): p. 423.
8. Wu, S., et al., *Novel electrically conductive porous PDMS/carbon nanofiber composites for deformable strain sensors and conductors.* ACS applied materials & interfaces, 2017. **9**(16): p. 14207-14215.
9. Sepulveda, A., et al., *Nanocomposite flexible pressure sensor for biomedical applications.* Procedia Engineering, 2011. **25**: p. 140-143.
10. Han, J.-W., et al., *Flexible, compressible, hydrophobic, floatable, and conductive carbon nanotube-polymer sponge.* Applied physics letters, 2013. **102**(5): p. 051903.
11. McCall, W.R., et al., *Piezoelectric nanoparticle–polymer composite foams.* ACS applied materials & interfaces, 2014. **6**(22): p. 19504-19509.
12. Liu, G., et al., *Triboelectric nanogenerator based on magnetically induced retractable spring steel tapes for efficient energy harvesting of large amplitude motion.* Nano Research, 2018. **11**(2): p. 633-641.
13. Zheng, Q., et al., *High-performance flexible piezoelectric nanogenerators consisting of porous cellulose nanofibril (CNF)/poly (dimethylsiloxane)(PDMS) aerogel films.* Nano Energy, 2016. **26**: p. 504-512.
14. Chun, J., et al., *Mesoporous pores impregnated with Au nanoparticles as effective dielectrics for enhancing triboelectric nanogenerator performance in harsh environments.* Energy & Environmental Science, 2015. **8**(10): p. 3006-3012.
15. Athanassiou, E.K., R.N. Grass, and W.J. Stark, *Large-scale production of carbon-coated copper nanoparticles for sensor applications.* Nanotechnology, 2006. **17**(6): p. 1668.

16. Amjadi, M., M.S. Kim, and I. Park. *Flexible and sensitive foot pad for sole distributed force detection*. in *Nanotechnology (IEEE-NANO), 2014 IEEE 14th International Conference on*. 2014. IEEE.
17. Boland, C.S., et al., *Sensitive electromechanical sensors using viscoelastic graphene-polymer nanocomposites.* Science, 2016. **354**(6317): p. 1257-1260.
18. *Comparative Study of Carbon Nanotubes and Carbon Nanofibers*. 2011; Available from: https://www.azonano.com/article.aspx?ArticleID=2885.
19. Zhou, K., et al., *Effect of dispersion on rheological and mechanical properties of polypropylene/carbon nanotubes nanocomposites.* Polymer Engineering & Science, 2012. **52**(7): p. 1485-1494.
20. Sandler, J., et al., *Carbon-nanofibre-reinforced poly (ether ether ketone) composites.* Composites Part A: Applied Science and Manufacturing, 2002. **33**(8): p. 1033-1039.
21. Chowdhury, S., et al. *Carbon Nanofiber and PDMS Based Nanocomposite With Sensing Functions*. in *ASME 2016 International Mechanical Engineering Congress and Exposition*. 2016. American Society of Mechanical Engineers.
22. King, M., et al., *Porous PDMS force sensitive resistors.* Procedia Chemistry, 2009. **1**(1): p. 568-571.
23. Rinaldi, A., et al., *A flexible and highly sensitive pressure sensor based on a PDMS foam coated with graphene nanoplatelets.* Sensors, 2016. **16**(12): p. 2148.
24. Zhang, A., et al., *Poly (dimethylsiloxane) oil absorbent with a three-dimensionally interconnected porous structure and swellable skeleton.* ACS applied materials & interfaces, 2013. **5**(20): p. 10201-10206.
25. Zhao, X., et al., *Durable superhydrophobic/superoleophilic PDMS sponges and their applications in selective oil absorption and in plugging oil leakages.* Journal of Materials Chemistry A, 2014. **2**(43): p. 18281-18287.
26. Kang, S., et al., *Highly Sensitive Pressure Sensor Based on Bioinspired Porous Structure for Real-Time Tactile Sensing.* Advanced Electronic Materials, 2016. **2**(12).
27. Chen, M., et al., *Highly stretchable conductors integrated with a conductive carbon nanotube/graphene network and 3D porous poly (dimethylsiloxane).* Advanced Functional Materials, 2014. **24**(47): p. 7548-7556.
28. Kobayashi, T., et al., *Porous membrane of polydimethylsiloxane by hydrosilylation cure: characteristics of membranes having pores formed by hydrogen foams.* Journal of applied polymer science, 1993. **50**(6): p. 971-979.
29. Grosse, M.T., et al., *Preparation of microcellular polysiloxane monoliths.* Journal of Polymer Science Part A: Polymer Chemistry, 2008. **46**(1): p. 21-32.
30. Huang, C., et al., *Experimental and theoretical study on mechanical properties of porous PDMS.* Journal of Applied Mechanics, 2018.
31. Lee, H., et al., *A Stretchable Polymer–Carbon Nanotube Composite Electrode for Flexible Lithium-Ion Batteries: Porosity Engineering by Controlled Phase Separation.* Advanced Energy Materials, 2012. **2**(8): p. 976-982.
32. Zhai, T., et al., *Poly (vinyl alcohol)/cellulose nanofibril hybrid aerogels with an aligned microtubular porous structure and their composites with*

polydimethylsiloxane. ACS applied materials & interfaces, 2015. **7**(13): p. 7436-7444.
33. Hinton, T.J., et al., *3D printing PDMS elastomer in a hydrophilic support bath via freeform reversible embedding.* ACS biomaterials science & engineering, 2016. **2**(10): p. 1781-1786.
34. Duan, S., et al., *Fabrication of highly stretchable conductors based on 3D printed porous poly (dimethylsiloxane) and conductive carbon nanotubes/graphene network.* ACS applied materials & interfaces, 2016. **8**(3): p. 2187-2192.
35. *Pyrograf Carbon Nanofiber*. Available from: http://pyrografproducts.com/nanofiber.html.
36. Lee, J.N., C. Park, and G.M. Whitesides, *Solvent compatibility of poly (dimethylsiloxane)-based microfluidic devices.* Analytical chemistry, 2003. **75**(23): p. 6544-6554.
37. Gokmen, M.T. and F.E. Du Prez, *Porous polymer particles—A comprehensive guide to synthesis, characterization, functionalization and applications.* Progress in Polymer Science, 2012. **37**(3): p. 365-405.
38. Vaid, A., R. Singh, and P. Lehana, *Developement of microchannel fabrication technique and method to increase trench depth on PDMS.* International Journal of Advanced Research in Computer and Communication Engineering, 2013. **2**(12): p. 2278-1021.
39. Lawrenson, A., K. Barnes, and N. Greeves, *ChemTube3D interactive 3D organic reaction mechanisms.* ChemTube3D, 2008.
40. *PDMS: A REVIEW*. Available from: https://www.elveflow.com/microfluidic-tutorials/microfluidic-reviews-and-tutorials/the-poly-di-methyl-siloxane-pdms-and-microfluidics/.
41. *Sylgard 184 clear 0.5kg kit*. Available from: https://krayden.com/buy/sylgard-184-0-5kg-1-1lb-kit-dc4019862.html.
42. Lam, C.-w., et al., *A review of carbon nanotube toxicity and assessment of potential occupational and environmental health risks.* Critical reviews in toxicology, 2006. **36**(3): p. 189-217.
43. Lantada, A.D., H.A. Iniesta, and J.P. García-Ruíz, *Composite scaffolds for osteochondral repair obtained by combination of additive manufacturing, leaching processes and hMSC-CM functionalization.* Materials Science and Engineering: C, 2016. **59**: p. 218-227.
44. Saha, M., et al., *Effect of density, microstructure, and strain rate on compression behavior of polymeric foams.* Materials Science and Engineering: A, 2005. **406**(1-2): p. 328-336.
45. Zhang, J., et al., *A comparative study of porous scaffolds with cubic and spherical macropores.* Polymer, 2005. **46**(13): p. 4979-4985.
46. CORNING, D., *SAFETY DATA SHEET*
47. Standard, A., *D638: Standard test method for tensile properties of plastics.* West Conshohocken (PA): ASTM International, 2010.
48. Lowrie, W., *Fundamentals of geophysics*. 2007: Cambridge university press.

49. Obitayo, W. and T. Liu, *A review: Carbon nanotube-based piezoresistive strain sensors.* Journal of Sensors, 2012. **2012**.
50. Barlian, A.A., et al., *Semiconductor piezoresistance for microsystems.* Proceedings of the IEEE, 2009. **97**(3): p. 513-552.
51. Rolnick, H., *Tension coefficient of resistance of metals.* Physical review, 1930. **36**(3): p. 506.
52. *Viscoelastic Material: Damping Property*. 2011; Available from: http://www.xyobalancer.com/xyo-balancer-blog/viscoelastic_material_damping_property.
53. Park, Y.-J. and A.H.-S. Ang, *Mechanistic seismic damage model for reinforced concrete.* Journal of structural engineering, 1985. **111**(4): p. 722-739.